

AN ABSTRACT OF THE THESIS OF

Erwin G. Schüttfort for the degree of Master of Science in Geology presented on January 3, 2001. Title: The Genesis of the San Vicente Lead Zinc Rhythmite Deposit, Peru - a Petrologic, Geochemical, and Sulfur Isotope Study

Redacted for Privacy

Abstract approved: _____


Cyrus W. Field

The San Vicente zinc lead deposit is located in the Eastern Andes of Central Peru. The deposit is an epigenetic Mississippi Valley-type deposit based on stratigraphic, geologic, petrographic, and geochemical evidence.

The dolomite host rocks of the Pucara Group are of Triassic-Jurassic age. The source of metals are red sandstones of the Late Permian Mitu Group. Sulfate was reduced to hydrogen sulfide at temperatures above 200 °C under acidic conditions in the lower parts of the sedimentary basin.

The paragenetic sequence of the mineral assemblage indicates replacement of original sedimentary dolomite-I by sphalerite. Organic matter is well preserved in the primary dolomite-I and partially overgrown by sulfides. Precipitation of sphalerite began prior to the deposition of galena, but both minerals occur contemporaneously in the rhythmite bands. Pyrite occurs as a minor component and precipitated during the last stages of sulfide mineralization. Open spaces between the rhythmite bands were filled with white, sparry dolomite-II.

Electron microprobe analyses indicate chemical zonations in dolomite and sulfide minerals. Dolomite-II is less homogeneous than the primary dolomite-I. The darker color of sphalerite correlates with elevated iron and cadmium concentrations.

The source of sulfur, temperature and physico-chemical conditions of the hydrothermal fluid are constrained by sulfur isotope measurements. The overall isotopic abundance of $\delta^{34}\text{S}$ indicates a Triassic-Jurassic marine sulfate source. The temperature of sulfide precipitation was approximately 140 °C as deduced from sphalerite-galena geothermometry. A distinct trend in the $\delta^{34}\text{S}$ values of sphalerite was observed. Isotope fractionation models indicate that the reduction of sulfate to hydrogen sulfide occurred most likely at temperatures above 200°C in the red sandstone of the Mitu Group. The reductant of sulfate was most likely ferrous iron.

Further evidence for the reduction of sulfate at higher temperature in slightly acidic environments comes from the thermodynamic modeling of the fluid. Speciation studies indicate that zinc is transported as a chloride complex that destabilizes at approximately 160 °C. The reaction mechanism of sulfate to hydrogen sulfide is favored in slightly acidic environments above 200°C.

The transport of metals by an acidic hydrothermal fluid from the deeper part of the basin and the reduction of sulfate away from the site of deposition are only compatible with an epigenetic origin of this deposit. Earlier syngenetic models by previous workers are not supported by the data obtained in this study.

©Copyright by Erwin G. Schüttfort
January 3, 2001
All Rights Reserved

**The Genesis of the San Vicente Lead Zinc Rhytmite Deposit,
Peru - a Petrologic, Geochemical, and Sulfur Isotope Study**

by

Erwin G. Schütfort

A THESIS

Submitted to

Oregon State University

In partial fulfillment of
the requirements for the
degree of

Master of Science

Presented January 3, 2001
Commencement June 2001

Master of Science thesis of Erwin Schüttfort presented on January 3, 2001

APPROVED:

Redacted for Privacy

Major Professor, representing Géology

Redacted for Privacy

Chair of Department of Geosciences

Redacted for Privacy

Dean of Graduate School

I understand that my thesis will become part of the permanent collection of Oregon State University libraries. My signature below authorizes release of my thesis to any reader upon request.

Redacted for Privacy

Erwin Schüttfort, Author

ACKNOWLEDGEMENTS

This research would not have been possible without the great encouragement and support from coworkers, friends, and my family. I am thankful to my mentor and advisor Dr. Cyrus W. Field who introduced me to the essential concepts of economic geology, scientific inquiry, and geologic writing. My committee members John Dilles, Roger Nielsen, and Jack Higginbotham have contributed valuable advice and laboratory facilities. Dr. Roman A. Schmitt also has stimulated many thoughts and introduced me to important concepts of modern geochemistry. I would like to thank him for his continuous encouragement and expertise in nuclear chemistry.

In addition, I received an excellent academic training from faculty in the Department of Chemistry. In particular, Dr. Michael W. Schuyler introduced me to practical analytical chemistry. Dr. Walter D. Loveland taught me nuclear chemistry and computer programming. I would like to thank all of them for their great teaching skills.

Throughout this research my wife Julianne has listened patiently to many of the ideas and provided the necessary atmosphere to complete this thesis. I would like to thank her for the patience, compassion, and encouragement. Guidance, support, and encouragement was also provided by my parents, Jurgen and Gudrun Schuffort. My son Theodor had kept up with my absence while writing the manuscript. I promise to find more time to be on the playground with him.

TABLE OF CONTENTS

Introduction	1
Previous Research	5
Geographic Location	6
Mining	9
Tectonic Framework	10
Regional Geology of the San Vicente Deposit	17
Mitu Group	17
Pucara Group	21
Chambara Formation	21
Aramachay Formation	22
Condorsigna Formation	23
The Utcuyacu Intrusion	23
Gabbroic Intrusions and Diorite Stocks	24
Petrography	25
Rhythmically-Banded Ore	26
Ore Breccia	30
Mineralogy and Textures	31
Dolomite-I	31
Bitumen	34
Sphalerite	36
Galena	40
Dolomite II	41
Pyrite	42
Paragenetic Sequence	44
Electron Microprobe Analyses	49
Dolomite	49
Sphalerite	53
Sulfur Isotope Study	61
Source of Sulfur	71

TABLE OF CONTENTS (CONTINUED)

Sulfur Isotope Geothermometry	78
Isotope Fractionation Models	82
Model I Isotopic Variation Caused by Sulfate Reduction to Hydrogen Sulfide.....	83
Model II Isotopic Variations in Sulfides due to Raleigh Fractionation of Hydrogen Sulfide	91
Model III: variations caused by changing pH and pe conditions	94
Chemistry of the Ore-Forming Fluids	97
Geochemical Modeling of the hydrothermal fluid	97
Construction of the pH-pe diagram.....	100
Molecular Reaction Mechanism of Sulfate Reduction	103
Speciation of Solutes in the Hydrothermal Fluid.....	107
Genetic Model of Ore Deposition.....	111
Summary and Conclusions	115
References	119
Appendices	125

LIST OF FIGURES

<u>Figure</u>		<u>Page</u>
1.	Geographic Location of the San Vicente Deposit (after Bartlett, 1984).	8
2.	Geology of Peru (modified after Petersen, 1965).	11
3.	Geographic Distribution of the Pucara Group in Peru (after Fontbote and Gorzawski, 1990).	13
4.	Schematic cross section and lithostratigraphic relationships of the Pucara Group and adjacent formations (after Loughman and Hallam, 1982).	14
5.	Regional Geology of the San Vicente Mine (after Fontbote and Gorzawski, 1990).	18
6.	Cross section profile AA' of San Vicente Deposit (after Fontbote and Gorzawski, 1990).	19
7.	Stratigraphic column of lithologic units in the San Vicente Deposit (after Fontbote and Gorzawski, 1990).	20
8.	Photograph of Rhythmite Ore (sample SV-6).	28
9.	Photograph of Breccia Ore sample (sample SV-5).	28
10.	Photomicrograph of rhythmite in (A) plane light and (B) cathodoluminescence view.	33
11.	Photomicrograph of dolomite-I in thin section SV-3.	35
12.	Photomicrograph of bitumen in thin section SV-5.	35

LIST OF FIGURES (Continued.)

<u>Figure</u>	<u>Page</u>
13. Photomicrograph of sphalerite-II from thin section SV-4a.	38
14. Photomicrograph of sphalerite-II from thin section SV-6.	38
15. Possible Hydrocarbon fluid inclusions in sphalerite.	39
16. Fractures and small veinlets in sphalerite filled with galena.	39
17. Photomicrograph of dolomite-II in thin section SV1.	43
18. Pyrite at the center of two sphalerite bands.	43
19. Schematic diagram illustrating the paragenetic sequence of mineral phases in the San Vicente ore.	45
20. Concentration profile of transition metals (Fe, Mn, and Zn) in dolomite-I (A, upper graph) and dolomite-II (B, lower graph).	51
21. Location of electron microprobe profiles on thin section SV5-B.	55
22. Chemical profiles of iron sulfide (FeS) and cadmium sulfide (CdS) in sphalerite SV5-B.	57
23. Profile of cadmium and iron concentration in sphalerite on thin section SV1A.	60
24. Location of sulfide concentrate samples (galena and sphalerite) on hand sample SV-4 (values are δ^{34S} in per mil).	65

LIST OF FIGURES (Continued.)

<u>Figure</u>		<u>Page</u>
25.	Plot of sulfur isotope $\delta^{34}\text{S}$ values from rhythmite bands of sample SV4 according to their paragenetic sequence.	66
26.	Sulfur isotope values of Central Peruvian Ore Deposits.	69
27.	Histogram of sulfur isotope values from sphalerite, galena and pyrite from this study.	72
28.	Plot of $\delta^{34}\text{S}$ values of sulfate and hydrogen sulfide calculated from Raleigh fractionation model at 140°C , given for case 3 (●-●) and case 4 (●-▼) of Model I.	87
29.	Evolution of $\delta^{34}\text{S}$ in sphalerite from a hydrothermal fluid at various sulfide to sulfate ratios over the temperature range from 275° to 100°C .	90
30.	$\delta^{34}\text{S}$ values of sphalerite, galena, and pyrite calculated for Model II based on the mole fraction of sphalerite ($X_{\text{sl}} = 0.85$), galena ($X_{\text{gn}} = 0.09$), and pyrite ($X_{\text{py}} = 0.06$).	93
31.	Possible models for the evolution of $\delta^{34}\text{S}$ values for sphalerite that involve changes in pH/pe conditions (Model III), reduction of sulfate to hydrogen sulfide (Model I), and Raleigh fractionation of hydrogen sulfide (Model II).	95
32.	Plot of the aqueous zinc-sulfur-carbon system at 25°C with respect to pe and pH.	102
33.	Speciation of zinc in sulfate solutions as a function of temperature.	108
34.	Speciation of zinc in sulfide solutions as a function of temperature.	110

LIST OF FIGURES (Continued.)

<u>Figure</u>		<u>Page</u>
35.	Genetic model of the San Vicente zinc-lead Mississippi Valley type deposit.	114

LIST OF TABLES

<u>Table</u>		<u>Page</u>
1.	Description and overview of hand samples of San Vicente ores and host rock.	27
2.	Chemical composition of dolomite from the San Vicente Dolomite (in wt. %).	50
3.	Sulfur Isotope Composition of Sulfides from the San Vicente Deposit (SL = sphalerite, Gn = galena, Py = pyrite).	63
4.	Summary of Sulfur Isotope Data of Ore Deposits in Central Peru.	68
5.	Delta values of sphalerite-galena mineral pairs including isotopic temperature estimates.	81

LIST OF APPENDICES

<u>Appendix</u>		<u>Page</u>
1.	Elemental Abundances of Zinc, Iron, Manganese , Cadmium, and Sulfur in Sample SV-1A (electron microprobe data).	126
2.	Elemental Abundances of Zinc, Iron, Manganese , Cadmium, and Sulfur in Sample SV-5B (electron microprobe data).	131
3.	Input parameter and calculations of isotope fractionation Model I.	134
4.	Input parameter and calculations of Isotope Fractionation Model II.	135
5.	Input parameter and calculations of Isotope Fractionation Model III.	136

THE GENESIS OF THE SAN VICENTE LEAD ZINC RHYTHMITE DEPOSIT, PERU - A PETROLOGIC, GEOCHEMICAL, AND SULFUR ISOTOPE STUDY

INTRODUCTION

The purpose of this research has been to determine the origin of the San Vicente zinc-lead deposit based on textural, mineralogical and geochemical studies of the sulfide ores and carbonate host rock. The relatively simple and uncomplicated mineralogy of the ores and host rock permits the application of standard petrographic techniques as well as specialized methods such as cathodoluminescence, electron microprobe analysis, and detailed sulfur isotope geochemistry.

Previous studies have demonstrated that the sulfur isotopic composition of sphalerite varies across the ore bands (Gorzawski, et al. 1990). These variations have neither been quantified nor have they been correlated with geochemical and mineralogical zones in sulfides such as the iron content and paragenetically distinguishable growth bands in sphalerite. Large isotopic variations with varying FeS content of sphalerite are unlikely because the fractionation equations for pyrrhotite-hydrogen sulfide (FeS-H₂S) and sphalerite-hydrogen sulfide (ZnS-H₂S) are identical at

$$1000 \ln \alpha = 0.10 \left(\frac{10^6}{T^2} \right) \quad (1)$$

according to Ohmoto and Rye (1979), where α is the fractionation factor and T denotes temperature in Kelvin. However, if the iron disulfide phase, pyrite

(FeS₂) becomes stable, cogenetic sphalerite might become isotopically depleted in ³⁴S, assuming a finite source of sulfur, because the fractionation equation for pyrite-hydrogen sulfide equilibria

$$1000 \ln \alpha = 0.4 \left(\frac{10^6}{T^2} \right) \quad (2)$$

dictates that pyrite is enriched in ³⁴S relative to either pyrrhotite or sphalerite. Consequently, changes in the physical and chemical conditions would likely be reflected in geochemical and petrographic variability.

Accordingly, the integration of chemical, mineralogical, and petrographic data collectively suggest that the San Vicente Zn-Pb ore body may be classified as a Mississippi Valley-type (MVT) deposit, as first tentatively suggested by Gorzawski et al. (1990) on the basis of more limited data.

World-class polymetallic sulfide deposits are abundantly present in the Central Andes of Peru. Porphyry copper-molybdenum deposits and stratabound Pb-Zn replacement deposits are economically the most important mineral resources of Peru. Most deposits in the Central Andes are easily classified into different hydrothermal types, because of their close association with igneous rocks and various ore and alteration mineral assemblages. However, the San Vicente ore is significantly different from those of other deposits of the Andes. For example, the ores are hosted entirely by carbonates of the Triassic-Jurassic Pucara Group, metal-rich (~10% wt. Zn & 1% wt. Pb) and dominated by sphalerite with minor galena. They occur as epigenetic rhythmites rather than as through-going vein or massive replacement deposits, and are not associated with either plutonic or volcanic igneous rocks.

The origin of the San Vicente deposit has been debated over the past three decades. Various genetic models such as syngenetic (Levin and Amstutz, 1976; Fontbote, 1987), diagenetic recrystallization (Fontbote and Gorzawski, 1990) and an epigenetic model (Gorzawski, H., Fontbote, L., Field, C.W., and Tejada, R., 1990; Lange et al., 1990) have been proposed. The focus of this study has been to obtain geochemical, mineralogical and petrographic data that are relevant to these conflicting hypotheses. The study of this deposit presumably may also be a significant contribution to the ongoing genetic discussion of Mississippi Valley Type deposits.

Cu-Pb-Zn-Ag replacement deposits are the most important deposits in the Central Andes (Fontbote, 1987) and are probably the second-most abundant sources of lead, zinc, and silver on Earth. The San Vicente deposit has few characteristics of a typical hydrothermal deposit, whereas in contrast it has many of those typical of a Mississippi Valley-type (MVT) deposit (Ohle, 1959). It is probably the first MVT deposit to be recognized in South America. Therefore, it is problematic to attribute this deposit to either one of the two classes, unless there is convincing evidence for either case.

The genesis of lead-zinc MVT deposits has been a geologic enigma almost since the first descriptions of this class of ores. Ohle (1959) summarized five different modes of origin. The initial hypothesis was that these deposits were syngenetic and formed contemporaneous to the original sediments, but many of the characteristics of these deposits are not plausible under this model. Therefore another hypothesis was postulated, suggesting that the textural

features of these deposits were slightly altered by subsequent regional metamorphism. However, these models were soon challenged by the suggestion that metasomatism could play a role in their formation, and thus, a third hypothesis was formulated proposing that the syngenetic deposition was followed by metasomatic processes originating from upward movement of groundwater. A fourth model that recognizes this same metamorphism, but related to downward moving fluids, has also been considered. Finally, yet another metasomatic model of origin has been proposed that attributes deposition of the ore directly from hydrothermal fluids that were derived from magmatic sources.

Discussions about the mode of origin of Mississippi Valley Type deposits in the recent literature have divided economic geologists in two groups. One group proposes syngenetic deposition of the ores, whereas the other favors epigenetic processes as main temporal factor. The term syngeneses is used to describe processes that happen to a sediment and its mineral components during transport, deposition, and the early stages of compaction, cementation, and diagenesis (Snyder, 1967). These phenomena are usually restricted to burial depth of less than 100 m. In economic geology the term syngeneses is applied to ores that form contemporaneously with igneous or sedimentary host rock, whereas epigenetic ores have originated after lithification of the enclosing host rock. Epigenesis in sedimentary geology refers to the changes and transformations that take place in sediment after compaction and lithification at low temperature and pressures prior to conditions that define metamorphism.

Mississippi Valley Type ores are strata-bound deposits of zinc-lead sulfide, that are localized in carbonate host rocks (Bates and Jackson, 1987). Characteristic features of these deposits according to Mills (1976) are as follows:

1. wall rock alteration is limited and consists largely of dolomite and jasperoid;
2. ore and gangue minerals consist chiefly of sphalerite, galena, and Fe-sulfides;
3. ore fills open spaces and breccias; and
4. ore and gangue minerals exhibit depositional and colloform banding, form cockade encrustations, and fill vugs.

Rhythmically banded ores, also referred to as rhythmites or zebra structure, are a succession of centimeter-thick bands of (1) dark-colored dolomite; (2) dark-colored sphalerite and galena, (3) colorless sphalerite with galena; and (4) central bands of white and coarsely crystalline dolomite (Fontbote, 1987).

Previous Research

Genetic aspects of San Vicente deposit were investigated initially by Levin and Amstutz (1976). They studied the structure of the ore rhythmites in hand specimens and identified twelve different types of rhythmic structures. Based on their observations, they interpreted the ore formation as syngenetic.

Lavado (1980) studied the general geology of the mine and contributed

geochemical data. He analyzed the total organic carbon content of the dolomite, which ranges from 0.1 to 3.4 wt. %, and pointed out that decomposition of organic matter may have provided the reducing conditions that generated hydrogen sulfide from a sedimentary sulfate source. Lavado's microprobe data indicate up to 4 wt.% iron in sphalerite. He attributed the ore formation to both diagenetic and epigenetic processes, while speculating that the metal source may have been a "hydrothermal fluid".

Fontbote (1987), Fontbote and Gorzawski (1988), Gorzawski et al. (1990), Fontbote et al. (1990), and Lange et al. (1990) were the first who presented sulfur isotopic data and detailed textural analysis of the ores as discussed below. While Fontbote (1987) concluded that the ore represents a "...diagenetic recrystallization rhythmite...", Lange (1990) later proposed an epigenetic origin for the deposit. At that time, Gorzawski et al. (1990) suggested that San Vicente ores were similar to Mississippi Valley-type deposits, an interpretation that subsequently was favored by Fontbote and Gorzawski (1990) and recently by Spangenberg et al. (1999).

Geographic Location

Peru is South America's third largest country, covering 1,285,215 sq. km., and can be divided into three distinct geographic regions. The best known of these is the central high Sierra of the Andes. To the west of the high Sierra is a narrow, lowland coastal region. The high Sierra is the northern extension of the Atacama Desert. Peru's third geographical region is the dense forest that

surrounds the headwaters of the Amazon at the base of the eastern slopes of the Andes.

The San Vicente mine is approximately 10 miles south of San Ramon in the eastern Andes of central Peru as shown in Figure 1. The elevation of the mine is 2,030 meters above sea level. Its geographic location is at $77^{\circ} 18' W$ longitude and $11^{\circ} 14' S$ latitude. Politically it is situated in the district of Vitoc, the Province of Chanchamayo and the Department of Junin. Lima, the capital of Peru, is approximately 300 km to the west.

The Chanchamayo province is characterized by dense jungle vegetation. The exposure of bedrock is limited and restricts field observation and accurate mapping of the surface geology. Rivers are on the east side of the continental divide and drain into the Amazon river system.



Figure 1. Geographic Location of the San Vicente Deposit (after Bartlett, 1984).

Mining

Lead and zinc occurrences have been known in the carbonates of the Pucara Group since 1950. Carpena Monroy staked the San Vicente mine in 1955 and began a small lead-mining operation. Compania Minera Chanchamina and Mauricio Hochschild S.A. formed the Compania Minera San Vicente in 1960. This company intensified explorations and discovered reserves of 850,000 metric tons of ore with 18% zinc. Compania Minera San Ignacio de Morococha, S.A. acquired partial control of the San Vicente deposit in 1969. Large-scale production began in 1970 at the rate of 79,000 tons per year and continues today at approximately 100,000 tons per year. Accumulated production and reserves are estimated at about 20 million metric tons of ore. The current ore grades are 10 weight percent zinc and 0.8 weight percent lead, and San Vicente is presently the largest zinc deposit in South America.

TECTONIC FRAMEWORK

Although this research focuses on a detailed examination of individual hand specimens collected at San Vicente in 1981 by Professor Cyrus W. Field, it is important to link these petrographic observations to the larger scale geologic framework. The geology of the Pucara Basin is therefore briefly reviewed based on the current literature and recent publications by previous workers. A brief description of each unit is included in this chapter along with a more detailed description of the Pucara Group, because of its importance in understanding the stratigraphic control of the rhythmite MVT mineralization.

The geology of Central Peru can be divided into six regional areas based on the types and ages of the predominant rock units. These are (1) the Coastal Mesozoic Belt, (2) the Coastal Batholith, (3) the Cenozoic Volcanic Belt, (4) the Central Andean Mesozoic Belt (5) the Eastern Paleozoic Belt, and (6) the Eastern Mesozoic Belt as illustrated in Figure 2. The belts strike in a north-northwesterly direction. The San Vicente deposit lies within the Eastern Paleozoic Belt of Central Peru as indicated in Figure 2. While most of the rocks in this area are Paleozoic, there are smaller exposures of pre-Cretaceous intrusions and Mesozoic sediments in the core of synclinal structures. The Eastern Paleozoic Belt is uplifted relative to the Central Andean Mesozoic and Eastern Mesozoic Belts.

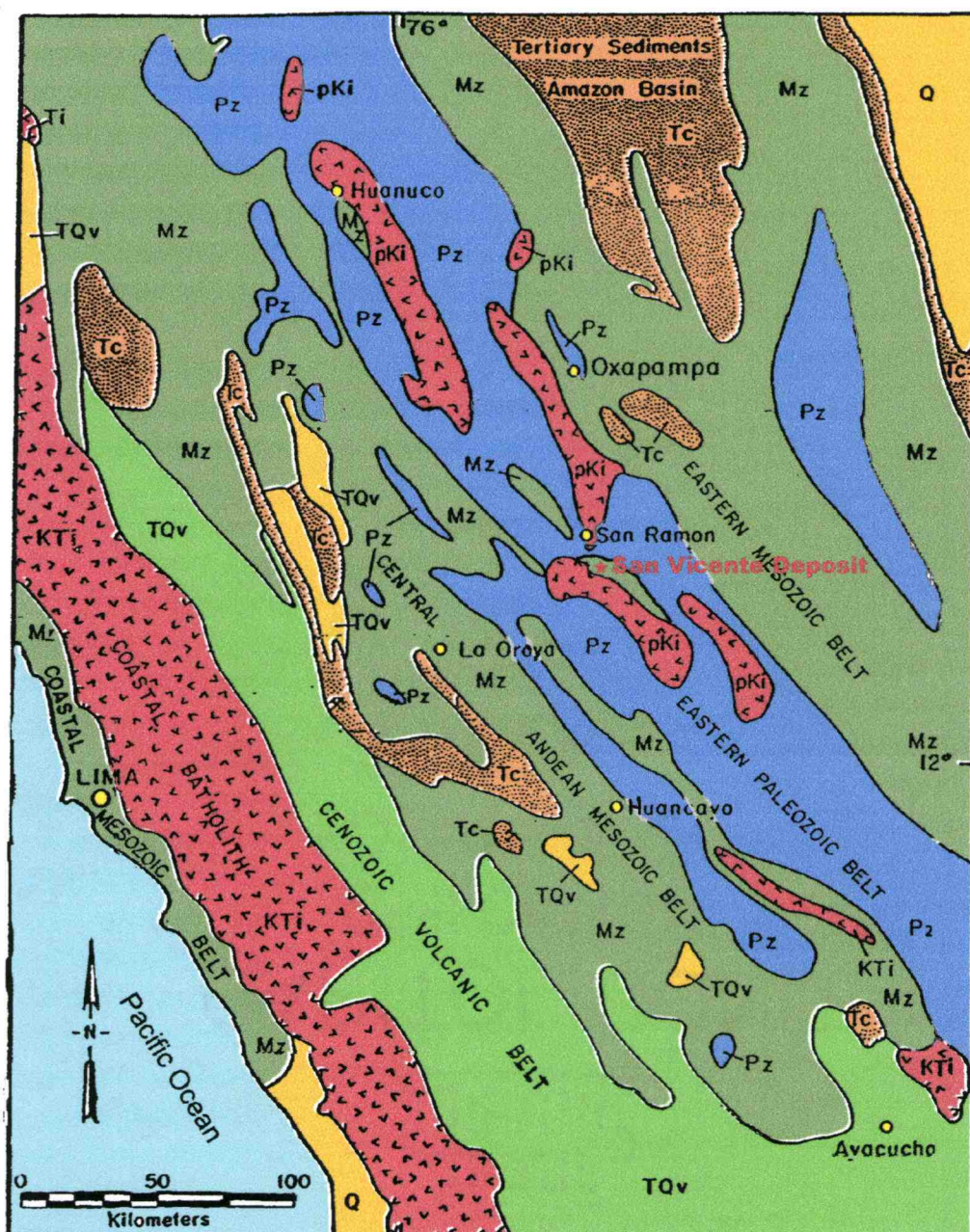


Figure 2. Geology of Peru (modified after Petersen, 1965). The stratigraphic legend is PZ= Paleozoic basement, Mz = Mesozoic sedimentary rocks, pKi = pre-Cretaceous intrusives, KTi = Cretaceous-Tertiary intrusives, Tc = Tertiary Casapalco Formation, TQv = Cenozoic volcanics, Q = Quaternary sediments).

The geographic distribution of the Pucara Group in Central Peru and the Eastern Cordillera is shown in Figure 3. Sedimentary rocks of the Pucara Group are present along two regional belts. West of the Comas-Tambo axis, the Pucara Group crops out along a northwestern trend from Huancayo to Cerro de Pasco. The type localities for the Aramachay and Chambara Formations are in this belt. This part of the basin corresponds to the Central Andean Mesozoic Belt in Figure 2. The Comas-Tambo axis is a horst structure that has uplifted Paleozoic rocks relative to the Central Cordillera and the Eastern Cordillera as shown in Figure 4. East of the axis, the Pucara Group is present in the Eastern Mesozoic Belt from Oxapampa to Huayanay.

Rocks of the Eastern Paleozoic belt consist predominantly of phyllites of the Silurian Excelsior Formation, red sandstones, clastic sediments, and volcanic rocks of the Permian Mitu Group, carbonates of the Pucara Group of Triassic-Jurassic age, and igneous rocks ranging from Paleozoic to Tertiary age. This belt trends northwesterly and is bordered to the west and east by the Central Andean Mesozoic Belt and the Eastern Mesozoic Belt, respectively.

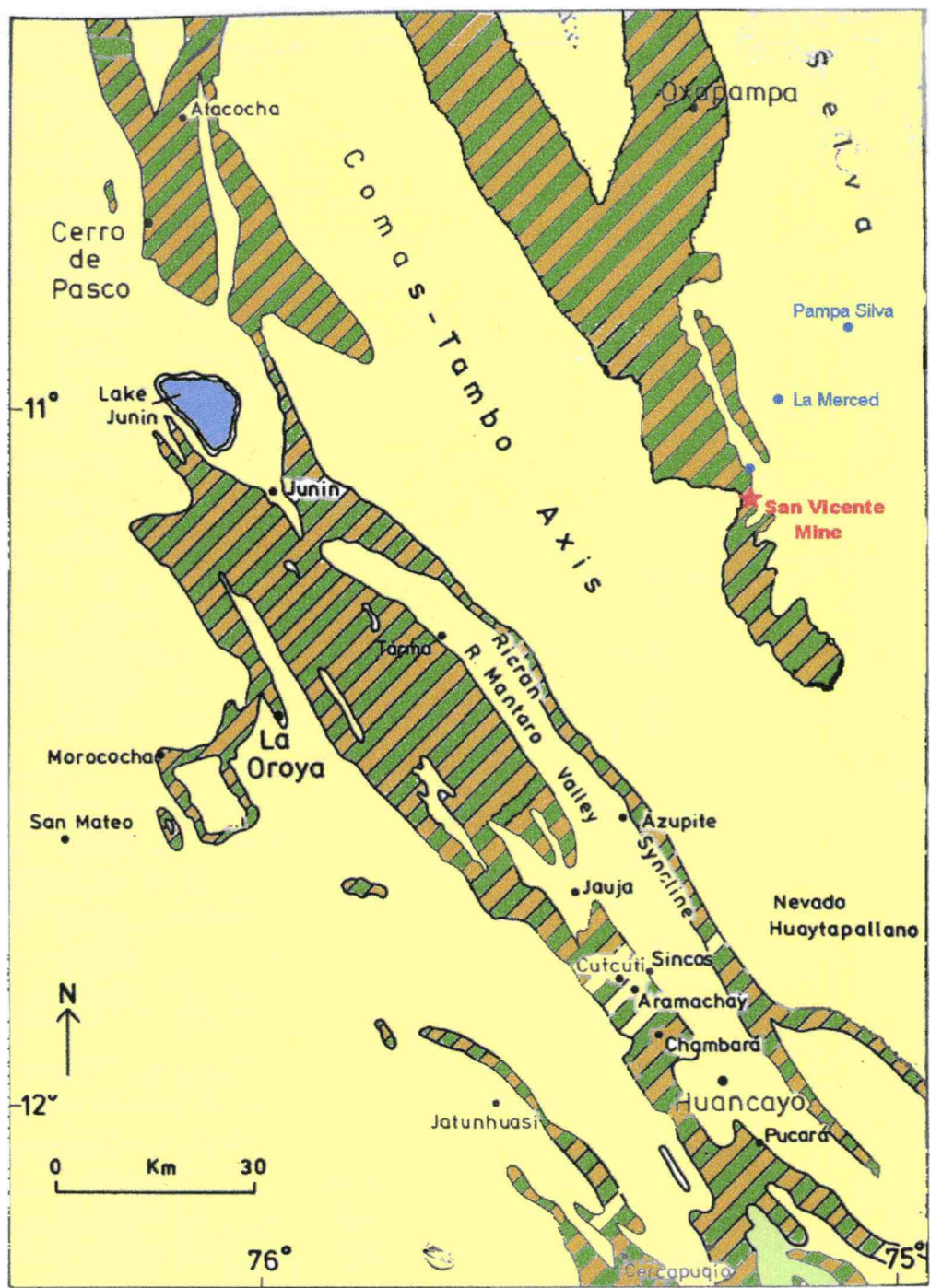


Figure 3. Geographic Distribution of the Pucara Group in Peru (after Fontbote and Gorzawski, 1990). The green-brown hatched area represents the outcrop pattern of the Pucara Group).

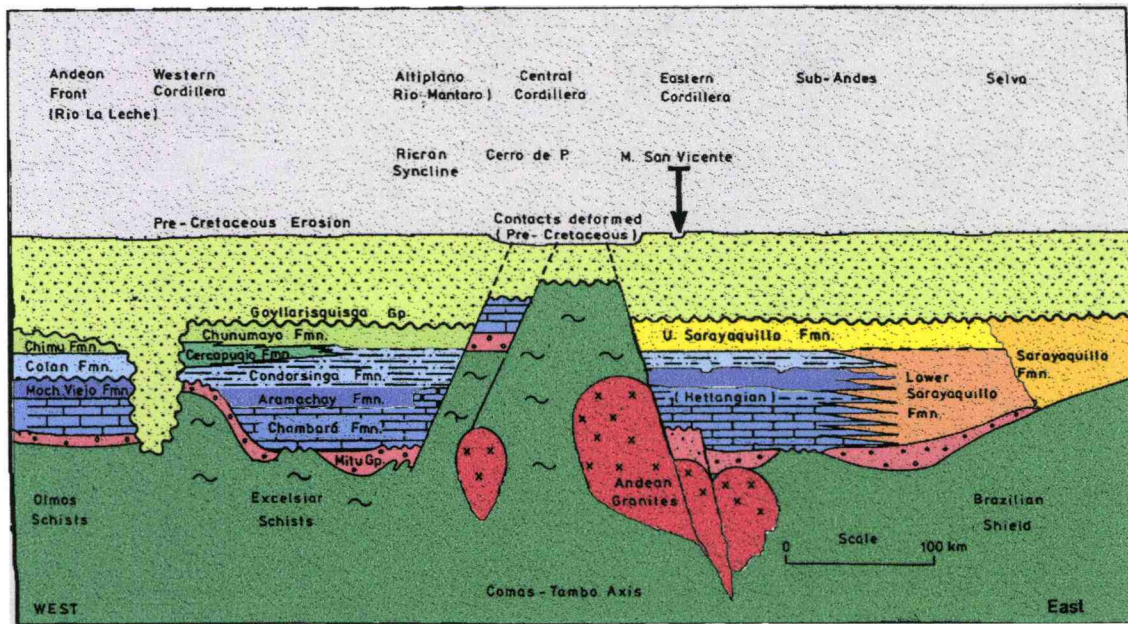


Figure 4. Schematic cross section and lithostratigraphic relationships of the Pucara Group and adjacent formations (after Loughman and Hallam, 1982).

Loughman and Hallam (1982) reconstructed the paleogeography and lithostratigraphy of the Pucara Basin. A schematic cross section of the basin is illustrated in Figure 4. Sedimentary rocks of the Pucara Group in the Altiplano and Western Cordillera of the Andes are separated from those in the Eastern Cordillera and Sub-Andes by the Paleozoic metamorphic rocks and Andean granites along the Comas-Tambo Axis in the Central Cordillera. The Brazilian shield borders the basin to the east. It also forms the crystalline basement beneath the eastern part of the basin.

Although the detailed stratigraphic correlation of sedimentary rocks in the Central and Eastern Cordillera has been a long-standing debate among geologists, the ages of these sedimentary rocks are similar and their depositional environment indicates the development of a sedimentary basin at the beginning of the Permian time. The presence of terrestrial and molasse sandstones indicate erosion of the Brazilian shield in an arid climate. The Pucara Group represents a marine transgression over Paleozoic terranes and red-bed molasse of the Mitu Group. This basin developed as a wide carbonate platform at the western margin of the Brazilian Shield in northern and central Peru. The deposition of carbonates was followed by clastic sediments of the Upper Sarayaquillo Formation during the Cretaceous. The evolution of the Pucara Basin is similar to that of carbonate platforms in other pericratonic areas. Unlike other Mesozoic basins in the Andes that are often influenced by arc related volcanism, the sedimentary rocks of the Pucara group show less

influence and association with volcanism. The contact of Tertiary volcanic rocks with the Mesozoic formations is characterized by an erosional unconformity.

The tectonic evolution of the Andes is highly complex and has involved at least four orogenic cycles (Caldas, 1983). These orogenic events include the Precambrian, Caledonian, Hercynian and Andean cycles. Of these, only the youngest Andean event has been recognized in the area encompassed by Figure 2. The Andean cycle began with deposition of Mesozoic sediments in two elongated belts, controlled by basement faults parallel to the western margin of Peru (Caldas, 1983). Major deformational events of the Andean cycle include (a) the Late Cretaceous-Early Eocene "Peruvian Phase", (b) the Upper Eocene – Lower Oligocene "Incaic Phase", (c) the Miocene-Pliocene "Quechua Phase" and, (d) Quarternary deformation.

The Peruvian Phase resulted in broad folding and general uplift of the Andes. Incaic deformation is responsible for most of the northwest-trending folds, thrust-faults, and compressionally induced features of Central Peru. The Quechua Phase folded Miocene continental sedimentary rocks. Post- Quechua Phase deformation generally is restricted to epirogenic uplift of the Andes and longitudinal faulting. The latter gave rise to the Pliocene-Quarternary volcanism in southern Peru (Caldas, 1983). Reactivation of faults produced during earlier deformational phases has continued to the present.

REGIONAL GEOLOGY OF THE SAN VICENTE DEPOSIT

The geology of the San Vicente mine is characterized by sedimentary rocks of the Mitu and Pucara Groups and the Utcuyacu granodiorite. A geologic map of the San Vicente area is shown Figure 5, and a cross section AA' given by Figure 6 depicts the subsurface geology of the local rock units (Fontbote and Gorzawski, 1990). The stratigraphic relationships of the units shown in Figure 5 and 6 are summarized in the stratigraphic column of Figure 7 based on the recent work by Fontbote and Spangenberg (1999). The base of the sedimentary basin is sandstone of the Permian Mitu Group. The lithology changes vertically upward to younger carbonates of the Triassic to Late Jurassic Pucara Group that host the ore body. The Utcuyacu intrusion has been thrust over the sedimentary rocks of this area.

Mitu Group

The Mitu Group contains volcanic andesites and rhyolites as well as terrestrial molasse sediments of Permian age. Sandstones and conglomerates are more abundant in the San Vicente area than are the volcanoclastic sedimentary rocks or lava flow rocks (Fontbote and Gorzawski, 1990). The sedimentary units represent the beginning of terrestrial sedimentation under arid climatic conditions. The provenance of the clastic sedimentary rocks is the crystalline basement of the Brazilian shield. In addition, pebble-sized fragments of the San Ramon Batholith are also observed in the conglomerates.

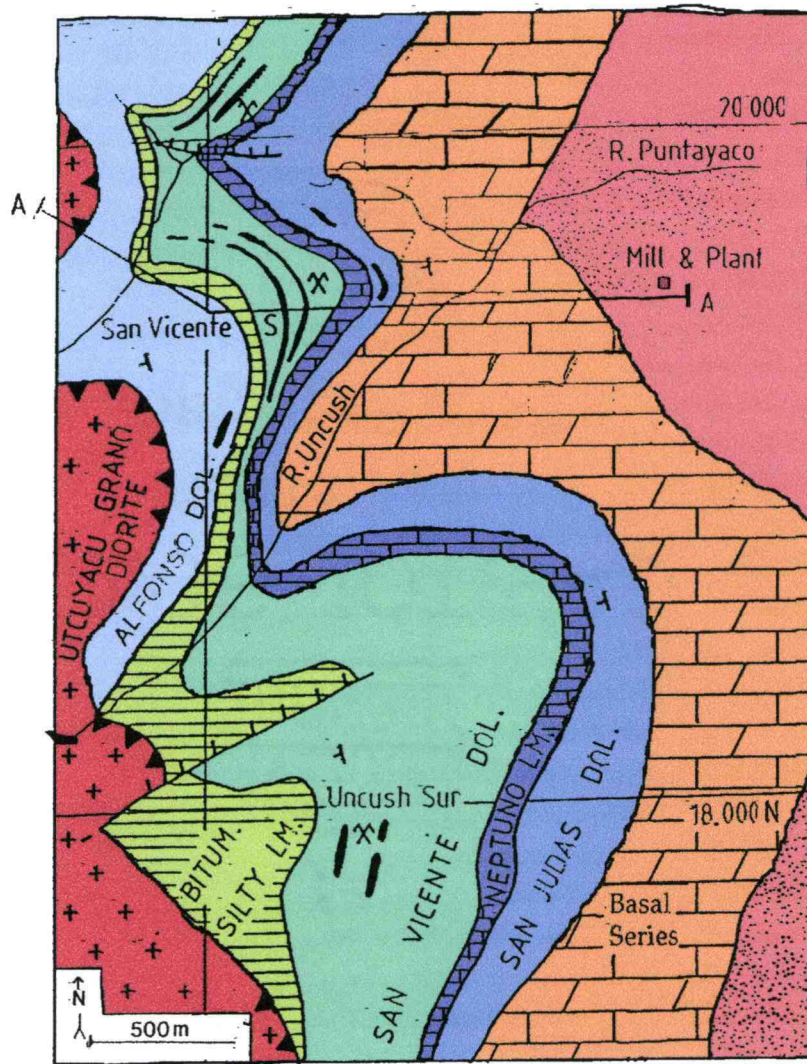


Figure 5. Regional Geology of the San Vicente Mine (after Fontbote and Gorzawski, 1990).

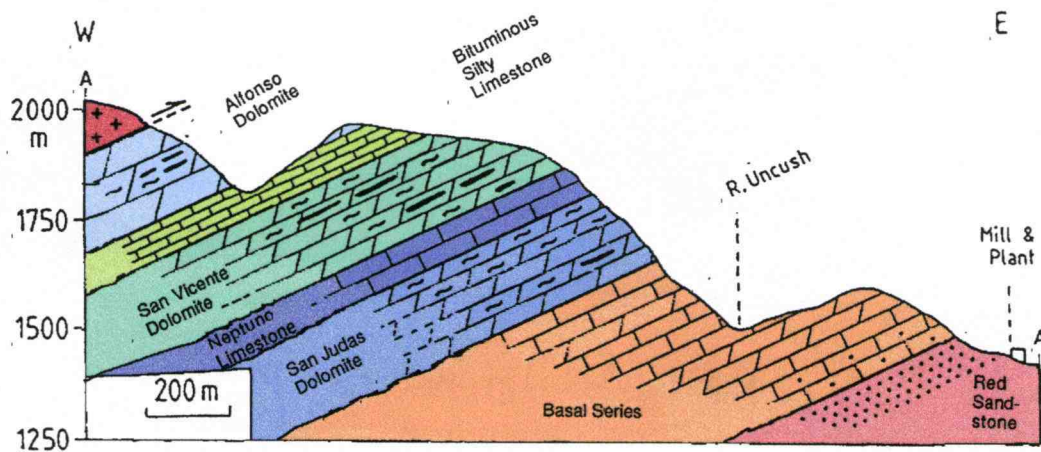


Figure 6. Cross section profile AA' of San Vicente Deposit (after Fontbote and Gorzawski, 1990).

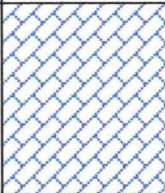

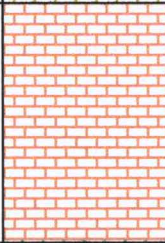
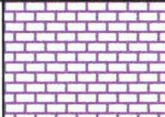
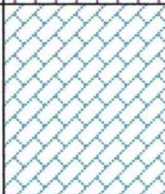
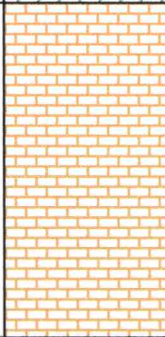

AGE		UNIT			Height	DESCRIPTION
JURASSIC	Hettangian	Condorsigna	Alfonso Dolomite		120 m	Medium to coarse crystalline dolomite
		Aramachay	Uncush Silty Limestone		105 m	Bitumen rich limestone with shale and silt intercalations
	Rhaetian	Chambara	San Vicente Dolomite		280 m	Main ore bearing unit Fine to very coarse crystalline dolomite. Subtidal oolithic barrier facies with lagoon and supratidal intercalations.
			Neptuno Limestone		150 m	Limestone with dolomite layers, shale intercalations
			San Judas Dolomite		380 m	Fine to coarse crystalline dolomite, formed in subtidal oolithic barrier facies with lagoon and supratidal intercalations.
			Basal Series		440 m	Limestone with dolomite, several horizons have up to 35% clastic minerals. The amount of detritus is high at the basis of the series.
		Mitu Group	Red Sandstone			Red silt and sandstone with lenses of gypsum CLASTIC FACIES
	TRIASSIC					

Figure 7. Schematic Stratigraphic column (after Fontbote and Gorzawski, 1990).

Pucara Group

The Pucara Group represents the first regionally extensive deposition of carbonates in the Mesozoic era. Formations of the Pucara Group have a Triassic-Jurassic age, and they were first described by McLaughlin (1924).

According to Megard (1968), the Pucara Group consists of: the Upper Triassic Chambara Formation, the Lower Liassic Aramachay Formation, and the Middle to Upper Liassic Condorsigna Formation.

Chambara Formation

The Chambara Formation is approximately 1150 meters thick in the San Vicente mining area. It consists of four members: (a) the Basal Series, (b) the San Judas Dolomite, (c) the Neptuno Limestone and (d) the San Vicente Dolomite. The age of the Chambara Formation is Norian to Rhaetian. The Basal Series lies conformably on top of red sandstones of the Mitu Group. It contains limestone and dolomite. The sediments are rich in detrital material, and up to 35 percent of the carbonate is composed of clastic fragments. The clasts are more abundant at the base and indicate a gradual shift with time from physical to chemical sedimentation. The depositional facies of the Basal Series indicates an open sea shelf defined by chemical precipitation intercalated with shallower conditions marked by clastic sedimentary rocks.

The San Judas Dolomite is approximately 380 m thick. The lithology is characterized by a fine to very coarsely crystalline dolomite. White sparry dolomite and evaporite pseudomorphs are found abundantly. The dolomite was deposited in a subtidal oolitic barrier facies with lagoonal and supratidal intercalations. Rhythmically banded sulfide mineralizations occur in the dolomite as small lens-shaped bodies, but are not mined at present.

The Neptuno Limestone overlies the San Judas Dolomite and underlies the San Vicente Dolomite. It consists of dolomite layers that are partially dolomitized. Intercalations of shale are present. The Neptuno Limestone is rich in detrital material and lacks significant sulfide mineralization.

The San Vicente Dolomite is the main ore-bearing unit within the Chambara Formation. It attains a thickness of about 280 m. The dominant lithology is fine to very coarsely crystalline dolomite. Lenses of white sparry dolomite and evaporite pseudomorphs are intercalated in the carbonates. The facies of this member indicates subtidal oolitic barriers with lagoonal and supratidal depositional environments according to Fontbote and Gorzawski, (1990). Tuffaceous and volcanoclastic rocks are also present as small lenses throughout the formation.

Aramachay Formation

The only unit of the Aramachay Formation that is present in the San Vicente mining area is the Uncush Limestone. It is approximately 105 m thick and lies conformably on the Chambara formation. It has a late Rheatian to

Hettangian age. The bituminous and silty Uncush Limestone is black in color and rich in organic matter. The total organic carbon content varies from 0.1 to 4.5 weight percent (Spangenberg and Macko, 1998). Very fine-grained pyrite occurs within the limestone. Detrital material is also locally present and forms shaly and silty intercalations that indicate nearby terrestrial sources of siliciclastic sediment.

Condorsigna Formation

The Condorsigna Formation is represented by the Alfonso Dolomite in the San Vicente mining area. The unit is 120 m thick and lies conformably on the Aramachay Formation. It was deposited during the Hettangian. The dolomite is medium to very coarsely crystalline and has abundant lenses of white sparry dolomite. It is the youngest formation present in the study area.

The Utcuyacu Intrusion

The Utcuyacu granodiorite intrudes the metamorphic basement rocks and is of late Permian to early Triassic age. The contact relationship to the carbonates of the Pucara Group is controversial. Levin (1974) reported an intrusive contact between the granodiorite and carbonates of the Pucara group which indicates that the intrusion is relatively young. On the other hand, Fontbote and Gorzawski (1990) observed a thrust fault contact. According to their observations, the fault dips at 20 to 40° west and can be traced over 4 km

in the field. A radiometric age determination of the batholith that is based on a Rb-Sr whole rock isochron indicates an age of 240 ± 4 Ma (Gunnesch et al., 1990). The Lower Triassic age coincides with extensive magmatic activity in the Eastern Cordillera (Megard, 1968).

Gabbroic Intrusions and Diorite Stocks

The second intrusive unit in the area consists of gabbroic and dioritic rocks. They are reported north of the San Vicente mine area in contact with the Utcuyacu granodiorite (Capedevila et al., 1977). The contact of one of these intrusions with sedimentary rock of the Pucara Group is exposed north of the Tarma river and has been described as a northeast-trending thrust fault (Fontbote and Gorzawski, 1990). Most authors have noted the presence of dioritic stocks and gabbroic dikes that intrude sedimentary units of the Pucara and Mitu Groups, but the age(s) of the intrusions have not been established by radiometric methods to date. On the basis of contact relationships the possible age of these intrusions ranges from post-Early Jurassic to late Cenozoic.

PETROGRAPHY

Evidence for the preferred epigenetic hypothesis of mineralization at San Vicente can be readily observed from standard petrographic observations of texture that serve as the basis for paragenetic interpretations. Megascopic examination of hand specimens from the San Vicente deposit provide textural evidence that the ore and gangue minerals are epigenetic. The best evidence consists of multiple generations of dolomite, sphalerite, and other sulfides, that encrust breccia fragments of the carbonate host and analytical evidence indicating that some of these minerals are chemically and texturally variable. Alternatively, syngentic or diagenetic mineralization expectedly might produce textures that are equivalent rather than cross-cutting, and the ore and gangue minerals characterized by less textural and chemical variability. Based on comparison to North American counterparts, the San Vicente deposit is a Mississippi Valley Type Deposit, contrary to the interpretations of many earlier investigators.

Individually separate and distinct bands of ore and carbonate minerals may be distinguished in hand specimens. Textures of individual crystals may also be observed where the minerals are sufficiently coarsely crystalline. Most importantly, however, the structural and textural relationships between the ore and associated sedimentary host rock are too large to be observed in thin section.

A detailed description of the samples used in this study is presented in Table 1. Examples of the rhythmically banded (sample SV-6) and breccia

(sample SV-5) ores are shown in Figures 8 and 9, respectively. From these descriptions it is evident that there are two principal macroscopically distinguishable ore textures present in hand specimens. One is represented by the rhythmically-banded ores, also often referred to as zebra ore, and the other is by brecciated fragments of the rhythmite ores.

Rhythmically-Banded Ore

Rhythmic bands of dolomite host rock and sphalerite-galena ore characterize most samples from the San Vicente deposit. Samples SV1, SV2, SV4, SV6, and SV7 are representative samples of the zebra type (rhythmically banded) ore.

Sample SV-6, illustrated in Figure 8, is representative of a typical rhythmically-banded ore. It consists of dark dolomite-I, sphalerite rhythmites with galena, dolomite-II gangue and late fracture healing dolomite-III. The thickness of the ore bands and the interlayered host rock (dark dolomite-I) varies in the samples. In sample SV-4, the sphalerite has a uniform thickness of approximately one centimeter throughout the sample, whereas the dark first generation dolomite-I and white dolomite-II bands are only 0.5 centimeter wide. In contrast, the ore bands of specimen SV-7 are much narrower and generally only 2 to 4 millimeters in width. The host rock has a similar thickness. These variations may be attributed to differing amounts of replacement of the original carbonate host rock.

Table 1. Description of hand samples of San Vicente Ore.

Hand Sample	Classification	Description	Thin sections / Polished Sections ¹⁾	Electron Microprobe Analyses ²⁾	Sulfur Isotope Analyses ³⁾
SV-1	banded rhythmite	alternating sequence of dolomite-I, sphalerite and dolomite-II. Abundant galena lenses.	TS: (1) / PS: (3)	yes	(12)
SV-2	dolomite host rock	dolomite host rock primarily dolomite-I with lenses of dolomite II.	TS: (1)	no	--
SV-3	dolomite host rock	hand sample of mostly dolomite-I host rock with larger lenses of dolomite-II and healed fractures of dolomite-III	TS: (1)	no	--
SV-4	banded rhythmite	alternating sequence of dolomite-I, sphalerite, and dolomite-II. Minor galena lenses are embedded in some of the rhythmite bands.	TS: (1) / PS: (5)	yes	(35)
SV-5	breccia ore	hydraulic breccia consisting of triangular fragments of banded rhythmite ore and a matrix of coarse dolomite-II	TS: (1) / PS: (1)	yes	(5)
SV-6	banded rhythmite	hand sample of banded rhythmite ore with a larger healed fracture of dolomite-III	TS: (1) / PS: (2)	yes	--
SV-7	banded rhythmite	alternating sequence of dolomite-I, sphalerite, and dolomite-II. The thickness of bands is relatively small.	TS: (1)	no	(5)

¹⁾ TS = thin section; PS = polished section. Number of sections in parentheses.

²⁾ Analyses of microprobe results are listed in Table 2 (main body text) and Table 3 and 4 (Appendix A)

³⁾ Number of sulfur isotope analyses in parentheses.



Figure 8. Photograph of Rhytmite Ore (sample SV-6).



Figure 9. Photograph of Breccia Ore sample (sample SV-5).

The dark and finely crystalline ($< 1\text{-}2\ \mu\text{m}$) dolomite-I is preferentially replaced by sphalerite-I. The replacement becomes more dominant towards the sphalerite-II band and eventually only sphalerite is present. The transition from host rock carbonate to a banded and secondary sulfide-dolomite replacement mineral assemblage indicates concomitant dissolution of the carbonate host and precipitation of sulfides in its place. At a later stage, fractures developed in which open space fillings and veinlets of sphalerite-II formed. Galena is a late minor phase present as irregular lenses at the edge of sphalerite bands. The galena crystals and globular masses range from millimeter to centimeter in size.

Fractures in the rhythmic bands are filled by white sparry dolomite-III that is similar in appearance to the dolomite-II. This third generation of dolomite can only be distinguished based on its cross-cutting relationship in hand samples. The fractures are most commonly oriented perpendicular to the bands, although others are found at oblique angles. The thickness of these fractures ranges from hairline-sized features, as observed in thin sections of sample SV-3, to as much as centimeter-wide healed fractures, as seen macroscopically in sample SV-6 as shown in Figure 8. Most thin fractures pinch out over short distances of a few centimeters.

Ore Breccia

Breccia samples are best represented by specimen SV-5 that is illustrated in Figure 9. Dolomite-I fragments are coated by sphalerite and galena ore, with the sulfides forming a band that generally surrounds the fragments. The matrix between the mineralized fragments consists of white and coarsely crystalline dolomite-II.

The fragments are several centimeters long and irregular in shape. The rock is interpreted to be a hydraulic breccia that probably formed during the mineralization and dolomitization event. The upper left corner of sample SV-5 depicts a triangular shaped void that was filled with sphalerite and cemented by later dolomite. Sphalerite that replaces the original dolomite exhibits a change in color from rim to center of the void. The color change can be attributed to changes in the chemistry of the hydrothermal fluid such as increased concentrations of iron and cadmium. The variation in the fluid chemistry causes changes in the minor element chemistry of sphalerite and affects the color of the mineral. Bitumen and organic material of the original host rock are preserved and form radially radiating spheres into sphalerite.

MINERALOGY AND TEXTURES

Three very distinct bands can be described in the zebra rock of San Vicente. Bands of sphalerite and galena surround dark and elongate fragments of Dolomite (I). The sphalerite-galena bands are themselves separated by bands of sparry dolomite (II). Doubly polished thin sections were prepared from all specimens. In addition, some polished plugs were prepared for reflected light observations. Samples SV-1,SV-2, SV-4 and SV-6 and SV-7 are banded rhythmites, whereas sample SV-5 represents a hydraulic breccia. Sample SV-3 is a larger section of the host rock without any of the bands of sulfide ore.

Dolomite-I

The term dolomite-I describes the minerals associated with the dark band of host rock that is surrounded by bands of sphalerite-galena ore. This rock consists mostly of dolomite clasts, dolomite cement, bitumen, sphalerite pore fillings, minor quartz, and disseminated pyrite. The thickness of the bands is approximately 1 to 1.5 cm in width, but varies slightly among the available specimens.

The dolomite is an intramicrite according to the classification scheme proposed by Folk (1962). The matrix consists of micritic dolomite with abundant inclusions of organic matter. The bitumen stains the layers or bands of host rock to its characteristic dark color. The grain size of the matrix is submicroscopic. In some bands, the density of the micritic dolomite becomes

sufficiently high to render its classification as a pure micrite. Usually, however, a coarse clastic component contributes about 30 percent by volume of the rock. Sample SV-4, as shown in Figure 10. , is representative of a typical band. Sphalerite-I replaces approximately 25 percent of dolomite-I and increases in abundance towards sphalerite-II in the rhythmite. The cathodoluminescence color of dolomite-I is orange and does not show zoning within the minerals (Figure 10.). A bright yellow luminescence is observed at the grain boundaries, but this effect does not relate to chemical variations. It is caused by the smaller thickness of the crystal at the boundary that results in the scattering of light. Both bitumen-rich micrite matrix and intraclasts have the same orange luminescence as can be observed by comparison to the light microscopy image (Figure 10.).

Boundaries to sphalerite-II of the rhythmite are irregular. On some bands the sphalerite-II continues and penetrates into dolomite-I. Replacement textures and pore space fillings are easily identified. Therefore, this sphalerite formed later than the host rock.

The coarser grained dolomite crystals surrounded by the dark matrix are easily distinguished by their translucent color. The size of the crystals is fine grained and they have anhedral to subhedral crystal shapes. Tiny inclusions within and carbonaceous material around these crystals indicate the replacement of original pelecypodal clasts. In some instances, the organic matter outlines shapes that resemble the appearance of microfossils, such as

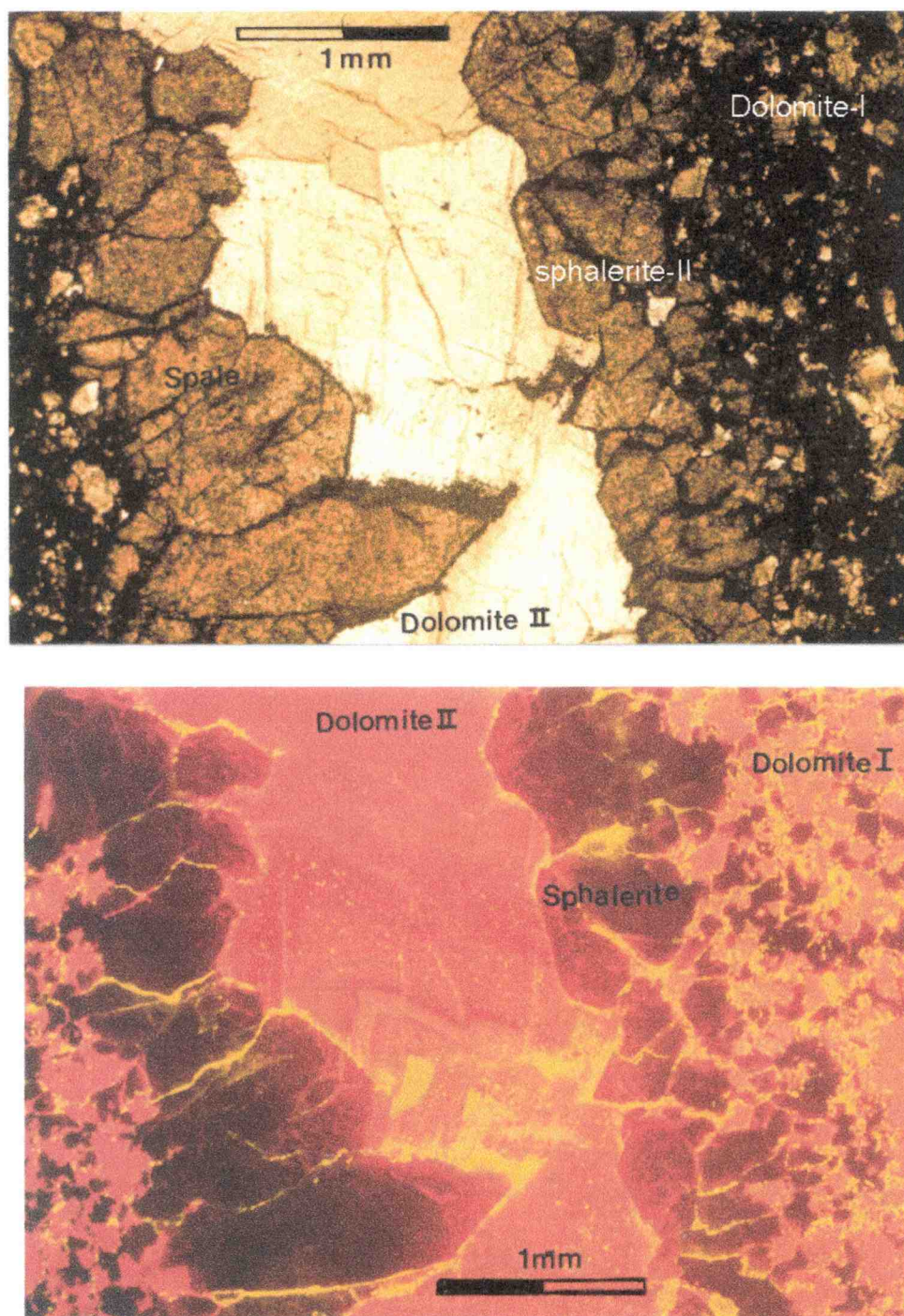


Figure 10. Photomicrograph of rhythmite in (A) plane light and (B) cathodoluminescence view.

ostracode shells. The large extent of recrystallization and diagenesis is too strong to confirm the presence or identity of possible microfossils. An example of such a remnant is illustrated in Figure 11. .

Detrital quartz grains were observed in one band at the contact with sulfides in a doubly polished thin section of sample SV-1B. The presence of quartz was also confirmed by electron microprobe analysis. The quartz is anhedral in shape, fine grained, and constitutes less than 1 percent of the host rock. Other clastic clay and silt-sized minerals were not observed in thin section. Thus, detritus in the carbonate host rock is not very abundant. Consequently, the facies can be interpreted as a shallow marine to lagoonal environment distant from terrestrial input.

Bitumen

Organic matter is abundant in dolomite-I. It is responsible for the dark color of the host rock. Bitumen is concentrated in the micritic carbonate, but is not found in the coarser clasts. Dolomitization of the host rock replaced calcium carbonate, but left the bitumen unaffected. This is demonstrated in Figure 12. . Pervasive dolomitization has replaced all of the original limestone and left stains of the bitumen in fragments. At the intersection of three dolomite veinlets a small sphalerite crystal developed. Bitumen also occurs in sulfide minerals where sphalerite-I replaces dolomite-I in the host rock. Its presence can be observed by comparison of cathodoluminescence and regular microscopy

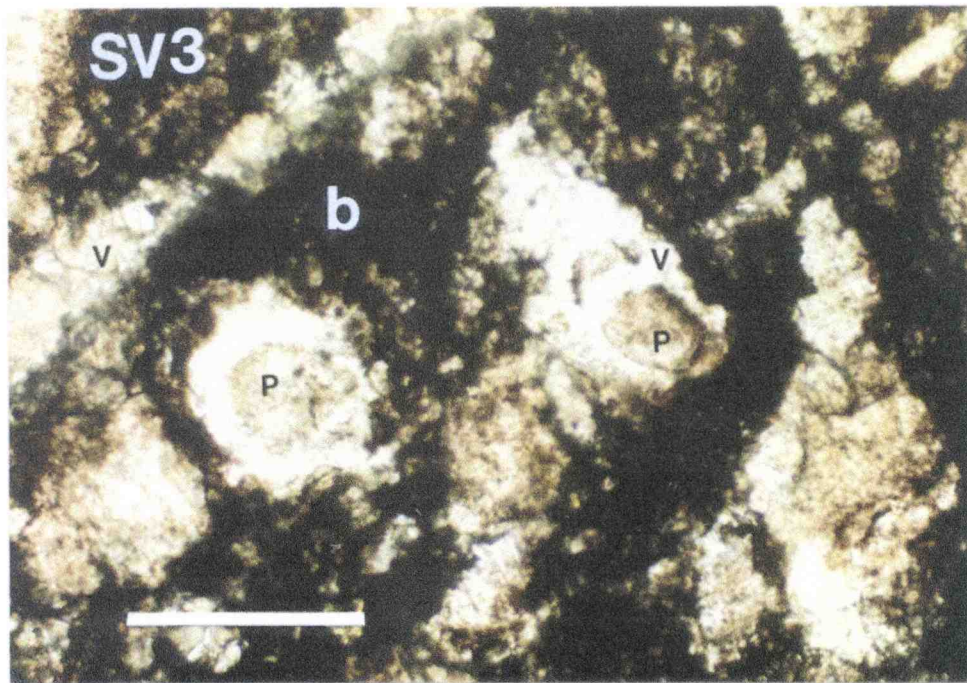


Figure 11. Photomicrograph of dolomite-I in thin section SV-3. Peleoids (p) are embedded in a matrix of bitumen (b) and small veinlets (v) of dolomite-II crosscut at oblique angles. Scale bar = 1 mm.

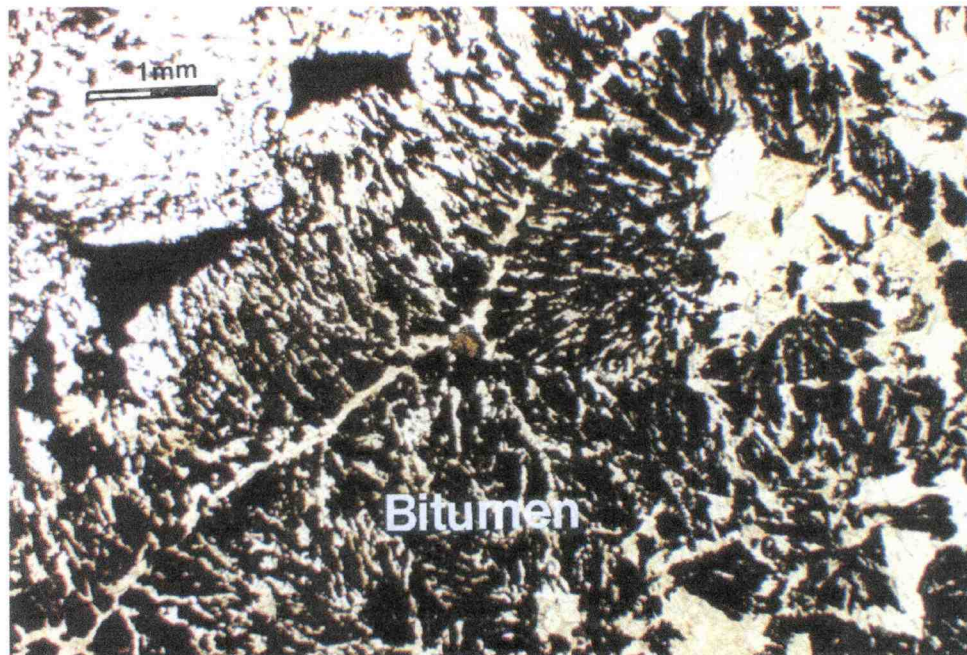


Figure 12. Photomicrograph of bitumen in thin section SV-5. Bitumen occurs as dendritic streaks in dolomite.

(Figure 10.), because the bitumen has not undergone dissolution during the replacement process.

Sphalerite

Three generations of sphalerite can be distinguished in thin sections. The first generation (sphalerite-I) occurs as replacements of dolomite and pore space fillings in dolomite-I host rock. Sphalerite-I has been described previously in context with the dolomite-I host rock. The second generation (sphalerite-II) represents the subhedral to euhedral crystals present along the veinlets. A third generation of sphalerite (sphalerite-III) grew contemporaneously with dolomite-II in the center of late cross-cutting veinlets.

The size of sphalerite-II crystals changes depending on the position in the rhythmite band. Crystals adjacent to the dark dolomite wall rock range from 0.2 to 0.5 mm in diameter and are subequant. They variably replace dolomite-I crystals in the host rock. The boundary of sphalerite-I with dolomite-I in host rock and the rhythmite band is gradational. Towards the center of the bands, sphalerite forms elongated, subhedral crystals that are 2 to 4 mm in length. At the contact with the white dolomite-II, the crystals are commonly isomorphous, indicating that they grew into open space. The apex of pyramidal-shaped crystals commonly points toward the centers of the veins.

The color of the sphalerite varies between hand samples. For example, thin section SV-1A has very light-colored sphalerite crystals with small brownish

zones in the center of some minerals. In contrast, yellow to red-brown colored sphalerite is present in sections SV-4A to SV-4B. Many of the sphalerite crystals have distinct individual color variations, as shown in Figure 13. . Often the core of the mineral is darker in color than its rim. The color variation is caused by variable chemical composition of the sphalerite, such that higher concentrations of iron and cadmium cause darker red to brownish colors.

Inclusions are present in sphalerite, but many are too small for fluid inclusion studies on conventional heating/freezing stage microscopes. Primary aqueous fluid inclusions are rare in the sphalerites. Sizes of the primary inclusions are often less than a micrometer (Figure 14.). The inclusions contain both an aqueous and a gaseous phase, but solid salt crystals were not observed. Twinning in sphalerite crystals is abundantly present in all thin sections. The planes of twinning are parallel to the {111} plane. Some of the twin planes enclose micrometer-size fluid inclusions. They are likely secondary fluid inclusions formed at a later stage than at time of original growth of the crystal.

Two larger inclusions of hydrocarbons were observed in thin section SV-1A as illustrated in Figure 15. . They are 3 to 5 μm in diameter and have a distinct orange-brown color. The color intensity (absorbance) is a function of composition and path length for many hydrocarbon inclusions (Burruss, 1981). In addition, the yellow color of the sphalerite host mineral may likely preclude an accurate absorbance analysis of the hydrocarbon inclusions by fluorescence microscopy.

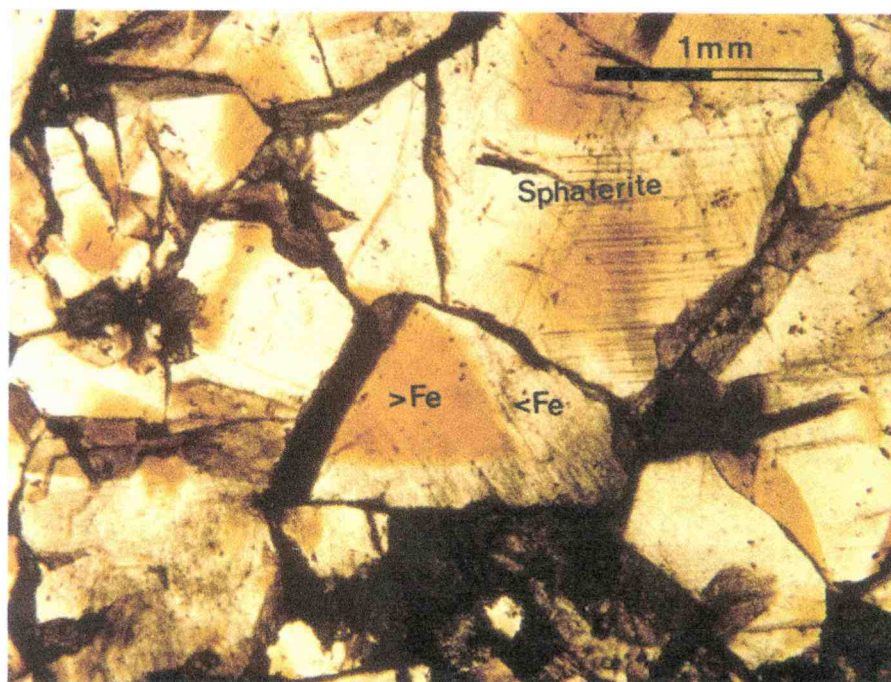


Figure 13. Photomicrograph of sphalerite-II from thin section SV-4a. Distinct color variations indicating high and low iron concentrations are present in individual crystals.

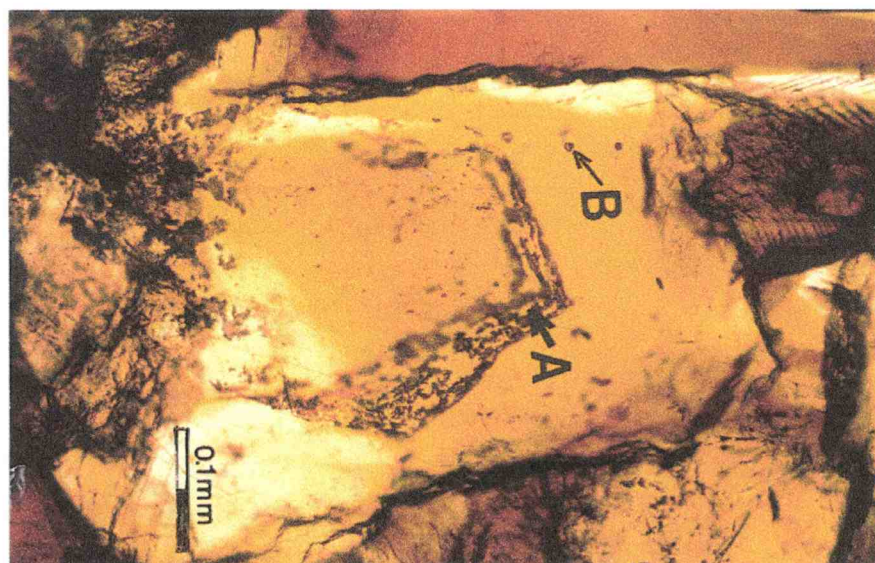


Figure 14. Photomicrograph of sphalerite-II from thin section SV-6. Small fluid inclusions (B) indicate a fluid and gas phase, submicroscopic stains on internal surfaces (A) indicate periodic interruption of precipitation and isomorphous growth into open spaces.

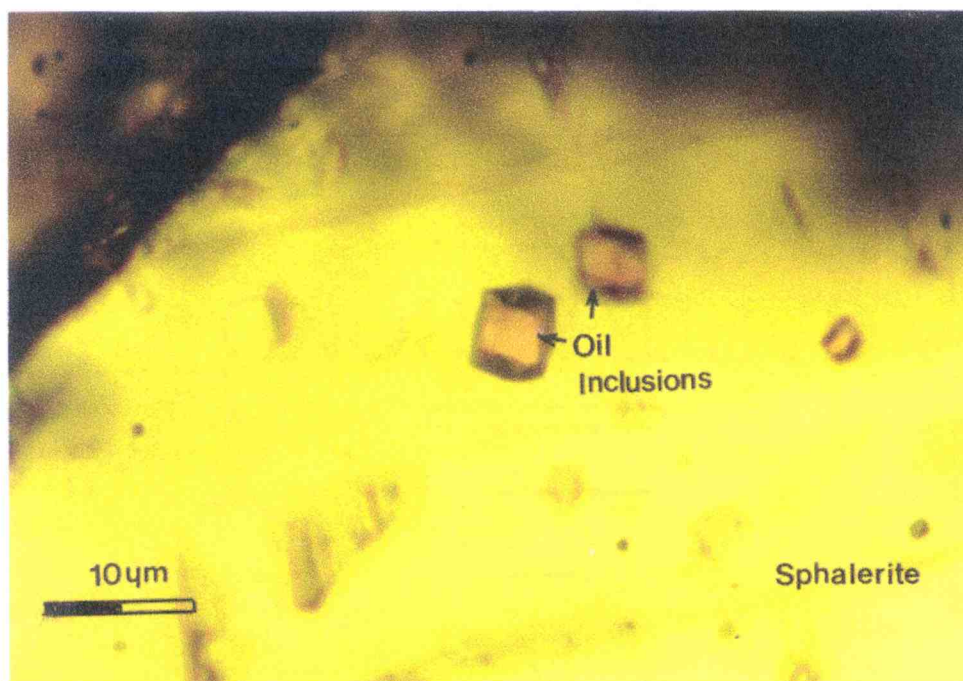


Figure 15. Possible Hydrocarbon fluid inclusions in sphalerite.

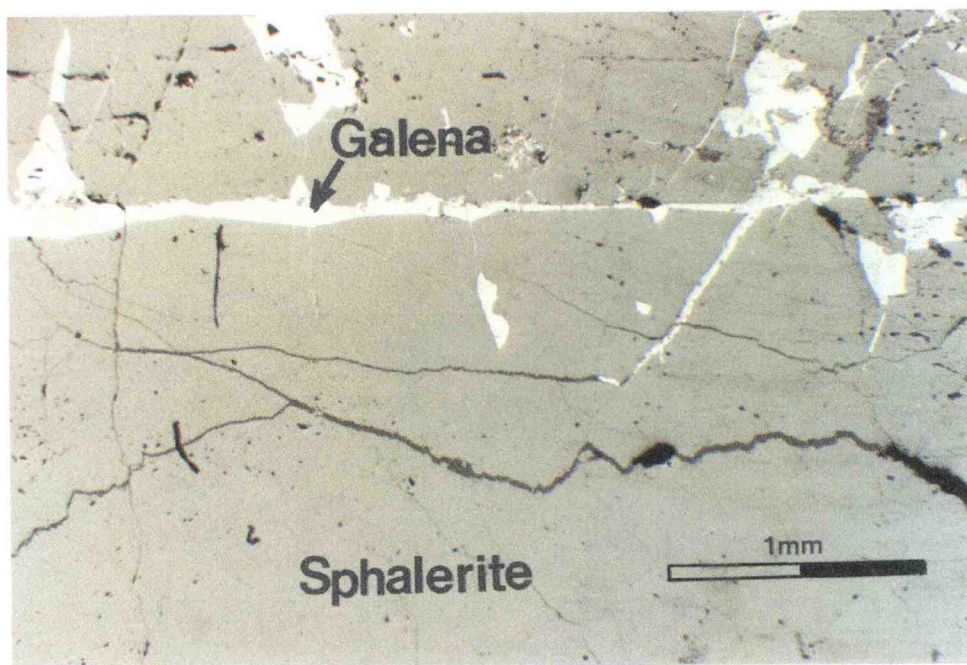


Figure 16. Fractures and small veinlets in sphalerite filled with galena.

Galena

Galena is usually much less abundant than sphalerite. It occurs at the transition between sphalerite-II bands and dolomite-II, and as intergranular space fillings in the earlier sphalerite-I generation. The texture of galena is anhedral, and it varies in size from a few millimeters to a centimeter.

Its textural relationship suggests that the mineral began to form at the same time as late sphalerite-II in the replacement bands, and continued to grow as sphalerite precipitation ended. Sample SV-4 contains a galena aggregate that grew across a fractured vein. It is therefore younger than dolomite-II and later than the initial stage of sphalerite-II. Galena also encloses smaller sphalerite crystals in some areas of the samples, whereas sphalerite-II may also completely enclose galena. Therefore, the textural relationships indicate contemporaneous to slightly later deposition of galena in the bands.

The distribution of galena in sample SV-4 is inhomogeneous. Galena is only present in the lower four bands of the hand-sample. Within these bands it is located predominantly on one side of the rhythmite. This unusual setting may indicate preferential distribution of colloidal galena, precipitation, and(or) settling during mineralization, and subsequent concentration along the footwall of the band. The orientation of the sample with respect to stratigraphic top and bottom was not established at the time of collection.

Replacement and fractures that are filled with galena are probably formed during remobilization at a later stage. These replacements and fracture fillings are best observed with reflected light microscopy. A typical fracture

healed by galena is shown in Figure 16. . These fracture-fillings of galena were not a problem during the sampling of sphalerite for isotopic analyses because, where present, they comprise less than one percent by volume of the sulfide-host rock.

Dolomite II

This term describes the white bands of sparry dolomite that separate bands of sphalerite replacing the dolomite-I host. The color of this mineral is light grey to white. The size of the crystals ranges from a one to five millimeters. Inclusions of other minerals are sphalerite and pyrite. The pyrite inclusions are very fine-grained and usually restricted to the center portion of the rhythmites. The light color of this dolomite results from the absence of organic matter in the crystals.

Surfaces between the dolomite II and sphalerite ore bands are characterized by the isomorphous termination of sphalerite crystals. In some thin sections the thickness of dolomite II bands becomes very narrow and eventually pinches out completely. Fragments of sphalerite crystals within the dolomite II bands are also present.

In hand specimens SV-1, SV-4, and SV-6 very small open cavities were observed. These cavities are associated with fractures and grain boundaries between individual dolomite crystals. One of these micro-vugs contained a small pyrite crystal that was extracted for sulfur isotope measurements. These cavities may be interpreted as spaces that were left open because of the

incomplete filling of the band.

Internal structures and textures in dolomite are difficult to observe from standard thin sections because light is reflected and scattered on these surfaces. On the other hand, polished thin sections reveal crystal growth bands in the mineral as shown in Figure 17. . The apex of the rhombohedral crystals in this sample point toward the center of the band. Some of the rhombohedral faces are slightly curved. Other bands have dolomite-II where rhombohedrons point parallel to the length of the bands (Figure 10. , cathodoluminescence view). This feature indicates that the white sparry dolomite fills open spaces of the bands.

Fractures that crosscut the ore bands were observed in hand specimen and polished sections of SV-6. The fractures are healed with sparry, coarsely crystalline dolomite of the third generation. Dolomite-III cannot otherwise be distinguished from dolomite-II.

Pyrite

Pyrite is present as a minor mineral constituent in dolomite-I host rock as well as at the center of dolomite-II bands as shown by Figure 18. . It is finely disseminated in dark dolomite-I, as observed in sample SV-3. Pyrite in the host rock is fine-grained and anhedral. Because of its trace abundance and very



Figure 17. Photomicrograph of dolomite-II in thin section SV1.

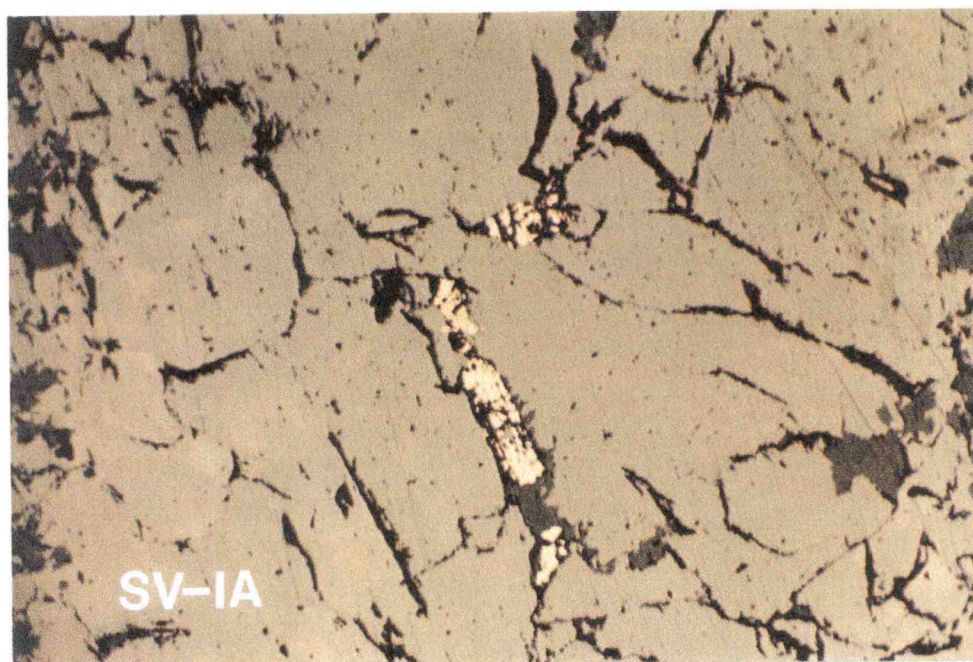


Figure 18. Pyrite at the center of two sphalerite bands.

small grain size, it was not possible to extract sufficient amounts of the host-rock pyrite for isotope analysis. Pyrite in the host dolomite may be formed by fixation of sulfide derived from the bacterial reduction of seawater sulfate at the time of formation. The small pyrite crystals show little evidence of dissolution and are probably remnants of syngenetic or diagenetic sedimentary sulfide.

Larger intergranular space fillings of pyrite in dolomite-II yielded enough sulfide material for isotopic determinations. Pyrite was also observed as abundant and very small (1 to 2 μm) sized crystal inclusions in sphalerite. These inclusions are abundant at the rim of subhedral to euhedral sphalerite in contact with rhythmite filling dolomite II. This textural relationship suggests the stabilization of pyrite at later stages in the mineralization, and might explain the lighter sulfur isotope values in sphalerite at the center of the rhythmites. The mineralogical (pyrite) and isotopic data (^{34}S depletion) also suggest a change in the chemical environment at the latest stages of the mineralization.

Paragenetic Sequence

The paragenetic sequence of minerals in the San Vicene orebody is relatively simple as shown in Figure 19. . This paragenesis is readily interpreted from macroscopic fabrics and mineralogic textures and indicates that limestone was replaced by dolomite. Sulfide precipitation replaces some of the dolomite growth over bitumen. Open spaces in the rhythmites are subsequently filled with white sparry dolomite.

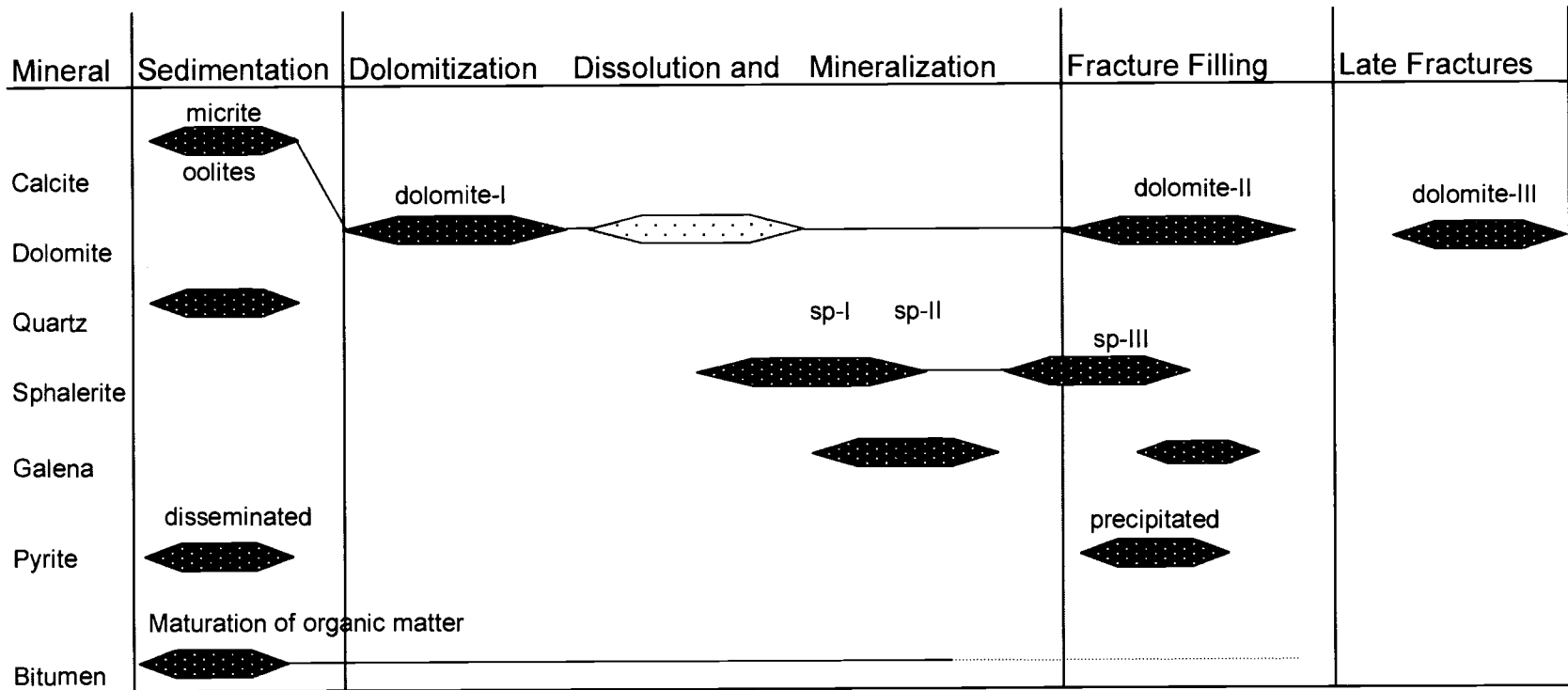


Figure 19. Paragenetic sequence of the San Vicente Ore.

Dolomitization has predated the ore mineralization, and appears to be a diagenetic process. The calcium to magnesium ratio in normal seawater is approximately 1:3 and the salinity is about 3.5 percent. Evaporation of seawater in Sabkha environments may increase the ratio to 1:10 and salinity to more than 5.0 to 35.0 percent (Folk and Land, 1975). Because the density of this hypersaline water is larger than the original seawater pore fluids, these waters then seep downward and replace the original sedimentary limestone with dolomite. The environmental conditions during formation of the Pucara Group presumably changed over time. On a stratigraphic scale, limestone units alternate with dolomite units. Dolomitization of limestone results in a decrease of volume by approximately 13%. This volume change may have lead to an increase in the hydrologic conductivity of the dolomitized carbonate units in the stratigraphic sequence.

The widespread presence of dissolution and replacement textures in the original dolomite host rock indicate that the mineralizing fluid was at least weakly acidic. Organic matter is hydrophobic and does not dissolve in hydrothermal waters. Sphalerite crystals precipitated over the bitumen and those containing laminar inclusions of organic matter were commonly noted in thin sections. Dissolution of the host rocks may also have contributed to the formation of the hydraulic breccias. This result would be expected when the strength of the partly dissolved host rock could no longer support itself and collapsed. The breccia sample SV-5 as well as collapsed beds in various hand

specimens are evidence for rock failure with advanced dissolution. The breccia is framework supported. These breccia structures could not have formed during early diagenesis because hydrothermal dolomite forms the matrix between the fragments.

The hydrothermal fluid precipitated sulfides in the sequence sphalerite, galena, and pyrite. The early sphalerite is present as pore and dissolution fillings in the corroded dolomite. It grows into the rhythmite as euhedral crystals, which indicate that open space was available during growth. Galena precipitated consequently with later sphalerite-II in the veins. Both minerals may contain inclusions of the other. Cross-cutting relationships between galena and dolomite-I bands indicate that the sulfide mineralization took place after dolomitization of the host rock. The open spaces in the rhythmite were ultimately filled with sparry dolomite-II. The large grain size, the absence of organic matter, and the euhedral crystal shapes strongly imply the precipitation of dolomite-II from a hydrothermal fluid.

ELECTRON MICROPROBE ANALYSES

Major and minor element compositions have been determined primarily for sphalerite, and secondarily for dolomite, galena, and pyrite by electron microprobe analyses of doubly polished thin sections. A CAMECA SX50 automated system housed at the College of Oceanic and Atmospheric Sciences was used. Each element was carefully calibrated prior to the analysis and several reference points on the unknown samples were checked periodically to ensure highly reproducible data quality. The acceleration voltage of the electron beam was 15 keV. The beam itself had a diameter of 3 - 5 μm .

Dolomite

The major elements of calcium and magnesium as well as the transition metals of zinc, iron and manganese were selected for the analyses of dolomite. Two line profiles from each dolomite generation were collected from a coarse dolomite-I crystal and across a dolomite-II crystal. The profile through dolomite-II spanned across a typical veinlet from hanging wall to footwall. The results of these analyses are tabulated in

Table 2. The concentration profiles of transition metals (Fe, Zn, and Mn) are shown in Figure 20A. Dolomite-I has higher iron and manganese concentrations in the core of the mineral (0.3 wt.% FeCO_3 and 1.75 wt.% ZnCO_3), whereas zinc is enriched towards the rim of the grain (~0.2wt. % at the rim, and ~0.3 wt.% MnCO_3 at the center). The relative

Table 2. Chemical composition of dolomite from the San Vicente Dolomite (in wt. %).

Sample	Point#	Mg(CO ₃)	Ca(CO ₃)	Mn(CO ₃)	Fe(CO ₃)	Zn(CO ₃)	Sr(CO ₃)	Total
SV-1	Dol-I 33	41.5	59.9	0.14	0.097	1.98	0.08	103.7
SV-1	Dol-I 34	45.8	55.9	0.26	0.196	1.75	0.08	103.9
SV-1	Dol-I 35	45.9	56.0	0.32	0.329	0.77	0.05	103.3
SV-1	Dol-I 36	46.2	54.0	0.31	0.347	0.38	0.32	101.5
SV-1	Dol-I 37	45.8	56.1	0.13	0.224	1.22	0.06	103.5
SV-1	Dol-II 40	46.6	54.0	0.13	0.82	1.79	0.12	103.4
SV-1	Dol-II 41	46.3	54.4	0.12	0.69	0.37		101.9
SV-1	Dol-II 42	37.8	62.3	0.06	1.22	0.22	0.08	101.7
SV-1	Dol-II 43	45.6	53.4	0.13	1.77	0.17	0.06	101.1
SV-1	Dol-II 44	32.7	65.7	0.16	2.08	0.08	0.05	100.7
SV-1	Dol-II 45	43.6	52.9	0.19	3.35	0.22	0.03	100.2
SV-1	Dol-II 46	42.5	53.2	0.19	4.31	0.13	0.03	100.3
SV-1	Dol-II 47	42.9	52.7	0.19	4.05	0.14	0.10	100.0
SV-1	Dol-II 48	45.8	53.5	0.15	1.52	0.04	0.02	101.1
SV-1	Dol-II 49	39.2	60.6	0.21	0.90	0.19	0.11	101.2
SV-1	Dol-II 50	41.0	58.6	0.15	1.19	0.16	0.10	101.2
SV-1	Dol-II 51	30.4	69.1	0.20	0.90	0.29	0.03	100.9
SV-1	Dol-II 52	44.7	52.8	0.20	1.29	0.32	0.09	99.4
SV-1	Dol-II 53	45.7	53.9	0.24	1.43		0.13	101.3
SV-1	Dol-II 54	44.0	55.3	0.27	1.40		0.08	101.1
SV-1	Dol-II 55	37.0	62.9	0.18	1.14	0.17	0.10	101.5
SV-1	Dol-II 56	41.6	53.3	0.19	0.95	0.07	0.05	96.1
SV-1	Dol-II 57	46.2	54.3	0.19	0.80	0.28	0.04	101.8
SV-1	Dol-II 58	46.1	54.4	0.16	0.62	0.26	0.11	101.6
SV-1	Dol-II 59	45.6	53.8	0.26	1.65	0.97	0.11	102.4

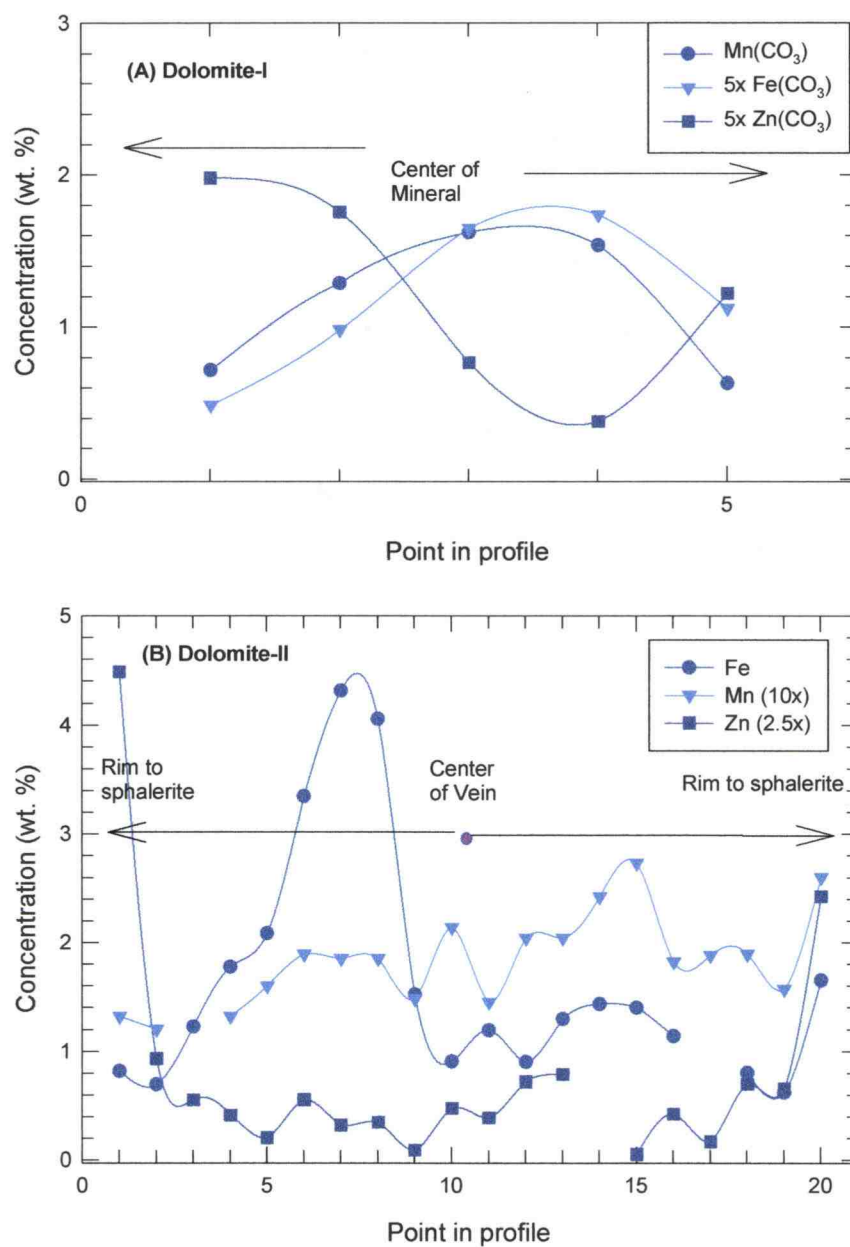


Figure 20. Concentration profile of transition metals (Fe, Mn, and Zn) in dolomite-I (A, upper graph) and dolomite-II (B, lower graph).

variations of the transition metals are less than in dolomite-II. The differing chemical trends indicate that dolomite-I can be considered a primary dolomite that was formed during the original dolomitization event and subsequently contaminated by sulfides.

The variation of transition metals in dolomite-II is shown in Figure 20B. The distance between the points is 38 μm . The concentration of zinc is four to five times higher at the rims of dolomite-II where the mineral is in contact with sphalerite-II crystals. Although both transition metals (Fe and Mn) vary across the crystals, iron (ranging from 4.31 to 0.63 wt.% FeCO_3) is more concentrated than manganese (ranging from 0.27 wt.% to 0.06 wt.% MnCO_3). Microscopic observations of the profiled section indicate the presence of small pyrite inclusions that could elevate the iron analyses locally. Iron quenches cathodoluminescence, whereas manganese enhances the signal greatly. The relative abundance of iron and manganese causes the color variations that may be observed in the cathodoluminescence images. The hydrothermal fluid that precipitated the carbonate was initially rich in zinc. The analyses at both ends of the profile indicate 0.97 to 1.79 wt.% ZnCO_3 . The points are more than 30 μm distant from the next sphalerite mineral, and should therefore be representative of dolomite without possible interference. Manganese and iron concentrations during crystallization were variable and have been preserved in the growth bands. Moreover, the absolute concentration of iron is also significantly higher in dolomite-II than in dolomite-I. Dolomite-II has an average iron carbonate concentration of 1.6 wt.%, whereas dolomite-I has only 0.24 wt.% iron

carbonate. The average manganese carbonate content in dolomite-II is 0.18 wt.% MnCO_3 , while dolomite-I contains 0.23 wt.% MnCO_3 . This enrichment in transition metals is presumably the result of higher concentrations of metals in the ore forming brine.

Sphalerite

Because this zinc sulfide is a major collector of various transition metals in solid solution, the chemical composition of sphalerite is an important indicator of co-solutes in the hydrothermal fluid. Iron, manganese, and cadmium are commonly noted in sphalerite as trace element constituents that cause color variations in the mineral. The abundance of manganese was often near the detection limit of the microprobe and has therefore not been included in the interpretation. The partitioning of iron and cadmium in sphalerite depends on the concentration of the various metals and on the physical and chemical conditions of the hydrothermal fluid. Therefore, components such as cadmium, manganese, and iron contribute information on the evolution of the fluid.

The analytical results for sphalerite in two doubly polished thin sections of sample SV-1A, a rhythmite ore, are listed in Appendix 1, and those of sample SV-5B, a breccia ore, are shown in Appendix 2. The paragenetic sequence in these samples is well established.

The location of the profiles on section SV5B are plotted in Figure 21. Four profiles were measured in thin section SV5-B. Profiles 1, 3 and 4 traverse a zone where sphalerite is initially colorless and clear and then abruptly

becomes yellow in color. Profile 2 begins in bitumen-stained sphalerite, continues through light yellow sphalerite, and terminates in bitumen-stained sphalerite. Profile 3 traverses a yellow sphalerite and terminates in clear sphalerite. Profile 4 is similar to profile 1 and spans also through yellowish sphalerite extending into clear sphalerite.



Figure 21. Location of electron microprobe profiles on thin section SV5-B.

The concentration of iron sulfide (mol % FeS) and cadmium sulfide (mol % CdS) in the profiles are plotted in Figure 22. The abundance of iron sulfide increases sharply from 0.2 mol % in the light yellow sphalerite to ~1 mol % in the dark yellow sphalerite as shown in profile 1 of Section SV-5B. At the edge to dolomite-II the concentration increases to 2.5 mol %, where the presence of small pyrite inclusions is observed at the contact of sphalerite to dolomite-II and resulted likely in this elevated iron sulfide content. Cadmium sulfide in profile 1 steadily decreases in light sphalerite-II from 0.35 to 0.10 mol %, whereas an increase from 0.10 to 0.16 mol % was measured for the section through yellow sphalerite. At the sphalerite crystal boundary towards dolomite-II the cadmium sulfide content decreases sharply to 0.08 mol %. The variations of both elements suggest that the composition of the hydrothermal fluid changed during the precipitation of the sulfides, and that individual crystals can exhibit a chemical zonation.

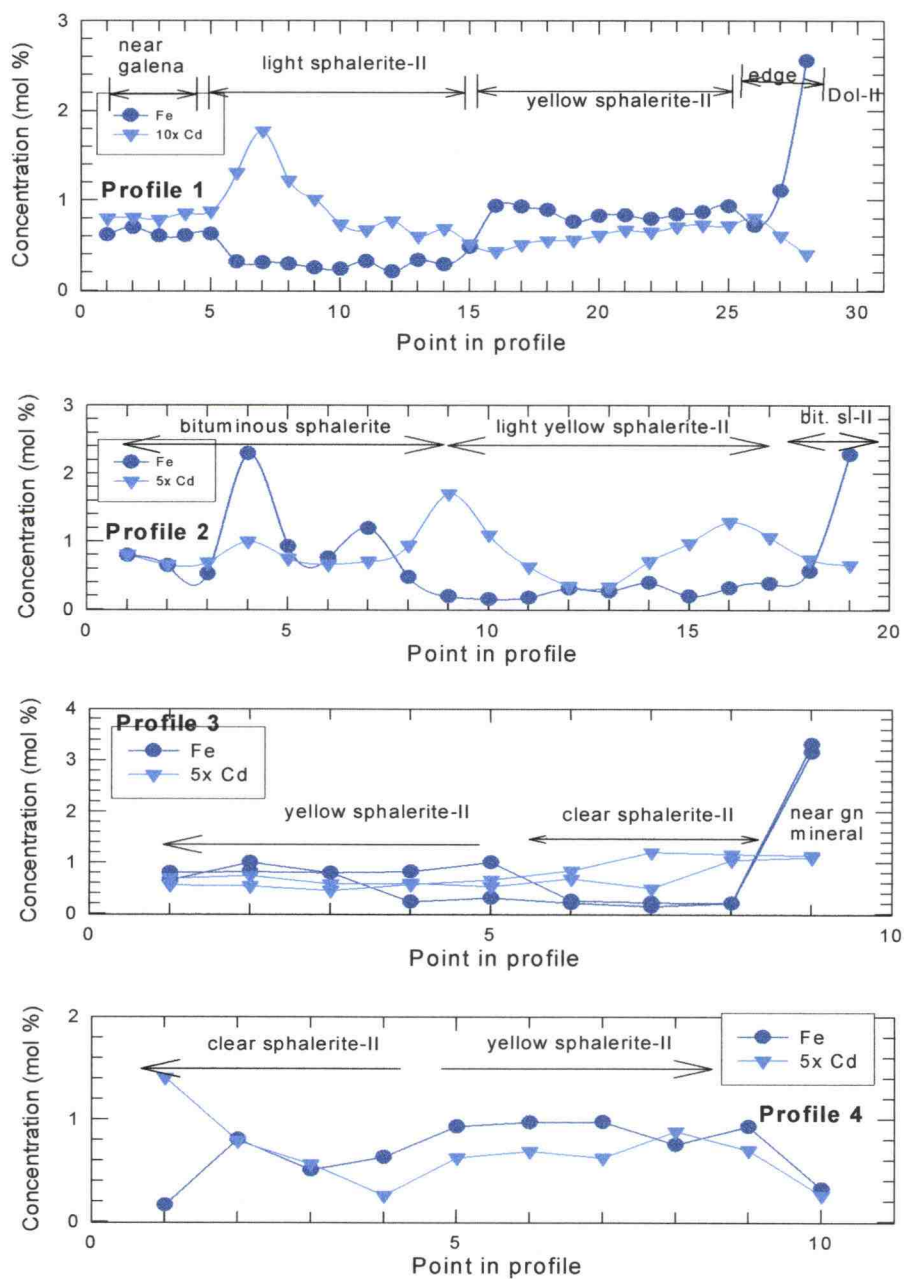


Figure 22. Chemical profiles of iron sulfide (FeS) and cadmium sulfide (CdS) in sphalerite SV5-B.

In profile 2, cadmium is generally less abundant and changes between the core (0.12 ± 0.05 mol %) and rim (0.23 ± 0.06 mol %) of individual sphalerite minerals. The iron content of sphalerite that replaced bitumen is higher (average: 1.0 ± 0.6 mol %) than in the light yellow sphalerite (average: 0.26 ± 0.09 mol %) as shown in profile 2 of section SV5-B. Profile 3 consists of two independent lines over the same area. It was measured in order to determine the reproducibility of the analyses. The concentration of iron and cadmium was reproduced with an accuracy of 20 percent. The concentration of iron increases from yellow to clear sphalerite-II that was precipitated later in this profile. The last point analysis of this profile indicates an iron abundance of 3.2 ± 0.1 mol %, where the crystal is in contact to galena. Profile 4 of sample SV-5B indicated less variation in iron (0.7 ± 0.3 mol %) and cadmium (0.14 ± 0.07 mol %) with respect to clear and light yellow sphalerite. However the iron to cadmium ratio (Fe mol % : Cd mol %) changes from 5 in the clear sphalerite to approximately 7 in the yellow crystal. This may indicate that cadmium has a fairly strong effect on the crystal color.

Similar concentration profiles were obtained from sample SV1-A and are illustrated in Figure 23. The two profiles from this thin section span two subparallel bands of sphalerite-II. Abrupt changes are present when the profile crosses individual grain boundaries. Again, the iron content generally increases toward paragenetically younger sphalerite. In profile 2, the iron content in the early sphalerite increases towards the rim of the crystal (0.1 mol % Fe at the

core to 0.5 mol % at the rim), whereas a late stage sphalerite mineral has a very low iron concentration (~ 0.03 mol %). This paragenetically later crystal is in contact with pyrite.

Concentrations of cadmium vary within individual crystals (from about 0.07 mol% between points 14-20 to 0.17 mol % between points 21-31) as shown in profile 1, but do not vary with respect to the crystal grain boundary in profile 2, where the average cadmium content is 0.15 mol %. Overall the variation of cadmium abundance is less than that of iron in these two profiles.

Chemical variations within individual crystals may not only be caused by compositional changes of the hydrothermal fluid, but also may be the result of solid diffusion. However, the general trend of increasing iron concentrations with paragenesis suggests a higher iron concentration in the fluids of later stages of mineralization. The interpretation of the electron microprobe data strongly depends on the reliability of paragenetic information and locally on crystal grain boundaries. Therefore, only sections that are petrographically well defined are likely to be useful in the interpretation of the chemical data in profiles such as these.

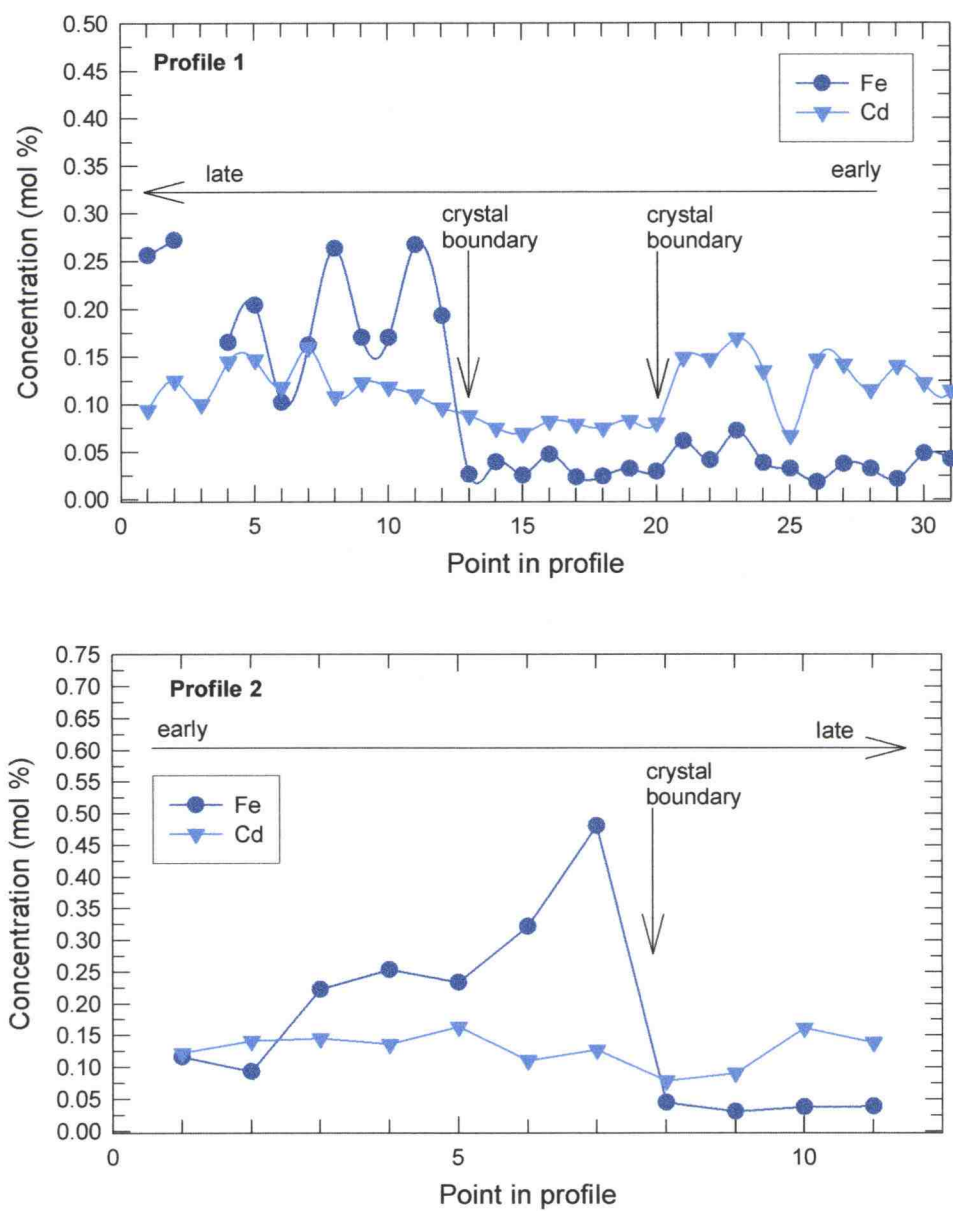


Figure 23. Profile of cadmium and iron concentration in sphalerite on thin section SV1A.

SULFUR ISOTOPE STUDY

Sulfur isotope analyses were undertaken to determine the probable source of sulfur in the ore minerals and to obtain information on the physical and chemical conditions of ore formation. The results of previous investigators and those of this study indicate that the isotopic signature varies across the ore rhythmites. In general, the sulfide minerals become progressively depleted in ^{34}S towards the center of the rhythmites and thus with diminishing age.

Sulfur isotope analyses were performed on 57 mineral separates of sulfides. Sulfate minerals were not identified in any of the samples. The sulfides analyzed consisted of sphalerite (48), galena (6) and pyrite (3). Sulfide mineral separations were performed in the ultra-clean laboratory facility at the Radiation Center. They were extracted as a pulverized sulfide from the hand specimens with a 1/32" diameter Dremel drill. The powders were carefully collected on weighing paper and stored in screw cap sample vials. The sulfide powders were oxidized to sulfur dioxide gas by the cupric oxide combustion method at 1025°C (Grinenko, 1962) in the sulfur extraction laboratory at Oregon State University under the supervision of Prof. Cyrus W. Field. Sulfur isotope analyses were performed at the University of Missouri by Dr. Kevin L. Shelton.

All isotopic data are reported as ‰ variations ($\delta^{34}\text{S}$) obtained from the relationship:

$$\delta^{34}\text{S} \text{ ‰} = \left(\frac{R_x}{R_s} - 1 \right) \cdot 1000 \quad (3)$$

, where R_x and R_s represent the measured and assumed $^{34}\text{S}/^{32}\text{S}$ ratios of the sample and the standard, respectively. Positive and negative ‰ deviations indicate enrichment and depletion of ^{34}S in the sample relative to the sulfur standard (troilite phase in the Canyon Diablo Meteorite, 0 ‰ by definition). The analytical uncertainty is better than ± 0.2 ‰ as determined from multiple preparations and analyses of the O.S.U. secondary standard (B-STD).

Isotopic data for the 57 mineral concentrates and brief descriptions of the sample are listed in Table 3. The mean $\delta^{34}\text{S}$ of all analyses is 8.7‰ and values range from 3.9‰ to 12.7‰. The mean values for sphalerite, galena and pyrite are 9.1, 6.1 and 7.6 ‰, respectively. The sulfur isotope composition of sulfides at the San Vicente deposit is remarkably uniform. The total $\delta^{34}\text{S}$ content of sulfide in the deposit may be calculated using a weighted average of the sulfides as given by

$$\delta^{34}\text{S}_{\text{tot}}, \text{‰} = \frac{w_{sp} \cdot \delta^{34}\text{S}_{sp} + w_{gn} \cdot \delta^{34}\text{S}_{gn}}{\sum w} = \frac{10 \cdot 9.1\text{‰} + 1 \cdot 6.1\text{‰}}{11} = 8.8\text{‰} \quad (4)$$

Sphalerite is approximately ten times more abundant than galena by weight percent ZnS, and pyrite is present only as a trace constituent, and where the value (8.8 ‰) reflects the dominance of sphalerite in the deposit.

Table 3. Sulfur Isotope Composition of Sulfides from the San Vicente Deposit (SL = sphalerite, Gn = galena, Py = pyrite).

Mineral	Sample	Rhythmite	Paragenesis	$\delta^{34}\text{S}$	Mineral	Sample	Rhythmite	Paragenesis	$\delta^{34}\text{S}$
Py	STD			1.1 ‰	SL	SV-4	C	early	12.0 ‰
SL	SV-1A	A	late	7.5 ‰	SL	SV-4	C	intermed.	9.5 ‰
SL	SV-1A	A	intermed.	8.3 ‰	SL	SV-4	C	late	8.7 ‰
SL	SV-1A	A	early	8.7 ‰	SL	SV-4	D	early	9.4 ‰
SL	SV-1A	B	intermed.	8.4 ‰	SL	SV-4	D	intermed.	8.9 ‰
SL	SV-1A	B	late	7.3 ‰	SL	SV-4	D	late	8.0 ‰
Gn	SV-1A	F	late	5.9 ‰	SL	SV-4	E	early	11.6 ‰
SL	SV-1A	C	intermed.	7.1 ‰	SL	SV-4	E	intermed.	9.4 ‰
Py	SV-1A	D	intermed.	8.1 ‰	SL	SV-4	E	late	9.9 ‰
Py	SV-1A	D	late	5.6 ‰	SL	SV-4	F	early	8.9 ‰
SL	SV-1A	E	intermed.	8.2 ‰	SL	SV-4	F	intermed.	8.5 ‰
SL	SV-1A	F	late	10.0 ‰	SL	SV-4	F	intermed.	7.5 ‰
SL	SV-1A	F	late	10.6 ‰	SL	SV-4	F	late	7.4 ‰
SL	SV-5B	A	late	8.3 ‰	Gn	SV-4	J	early	7.4 ‰
SL	SV-5B	A	late	7.8 ‰	Gn	SV-4	I	early	6.4 ‰
SL	SV-5B	A	early	8.8 ‰	Gn	SV-4	T4	late	3.9 ‰
Py	SV-5B	B	late	9.3 ‰	SL	SV-4	G	intermed.	7.9 ‰
SL	SV-5B	B	late	8.1 ‰	SL	SV-4	G	early	10.0 ‰
SL	SV-7	A	late	9.0 ‰	SL	SV-4	G	intermed.	9.8 ‰
SL	SV-7	A	early	10.7 ‰	SL	SV-4	G	late	7.2 ‰
SL	SV-7	A	intermed.	10.0 ‰	SL	SV-4	H	early	9.3 ‰
SL	SV-7	A	intermed.	9.9 ‰	SL	SV-4	H	intermed.	9.2 ‰
Gn	SV-7	A	late	4.8 ‰	SL	SV-4	H	intermed.	9.3 ‰
SL	SV-4	T4	late	8.1 ‰	SL	SV-4	H	late	9.3 ‰
SL	SV-4	A	late	8.6 ‰	SL	SV-4	I	early	12.7 ‰
SL	SV-4	A	intermed.	8.7 ‰	SL	SV-4	I	intermed.	11.5 ‰
SL	SV-4	A	early	9.3 ‰	SL	SV-4	I	late	10.6 ‰
SL	SV-4	B	late	8.5 ‰					
SL	SV-4	B	intermed.	9.6 ‰					
SL	SV-4	B	early	9.5 ‰					
Gn	SV-4	B	late	7.9 ‰					

The heaviest sulfur isotope compositions at San Vicente reside in sphalerites and those that were precipitated early are enriched in ^{34}S relative to those of paragenetically later varieties. In particular, sample SV-4 was selected to study possible relationships between sulfur isotope abundances and the paragenetic sequence of sulfide deposition. A photograph of a polished slab of this ore sample given in Figure 24. shows the location and $\delta^{34}\text{S}$ per mil values of the sulfide concentrates. The terms early, intermediate and late sphalerite were assigned to the paragenetic sequence of sulfide concentrates separated from a single rhythmite based on their proximity to the immediately nearby slivers of unreplaced dolomite host rock.

The trend of lighter sulfur isotope compositions towards the center of the rhythmite is apparent from an examination of all the data in Table 3. The average $\delta^{34}\text{S}$ per mil values for early, intermediate and late sphalerites are 10.1, 9.0 and 8.6 ‰, respectively. Sphalerites from individual profiles of single rhythmites becomes consistently depleted in $\delta^{34}\text{S}$ (lighter) towards the center of the bands as illustrated in Figure 25. The largest trend was observed in rhythmite SV4-A where the difference between early and late sphalerite is 4.6 ‰. The average difference is 1.8 ‰ with a standard deviation of 1.3 ‰.

Sample SV-4

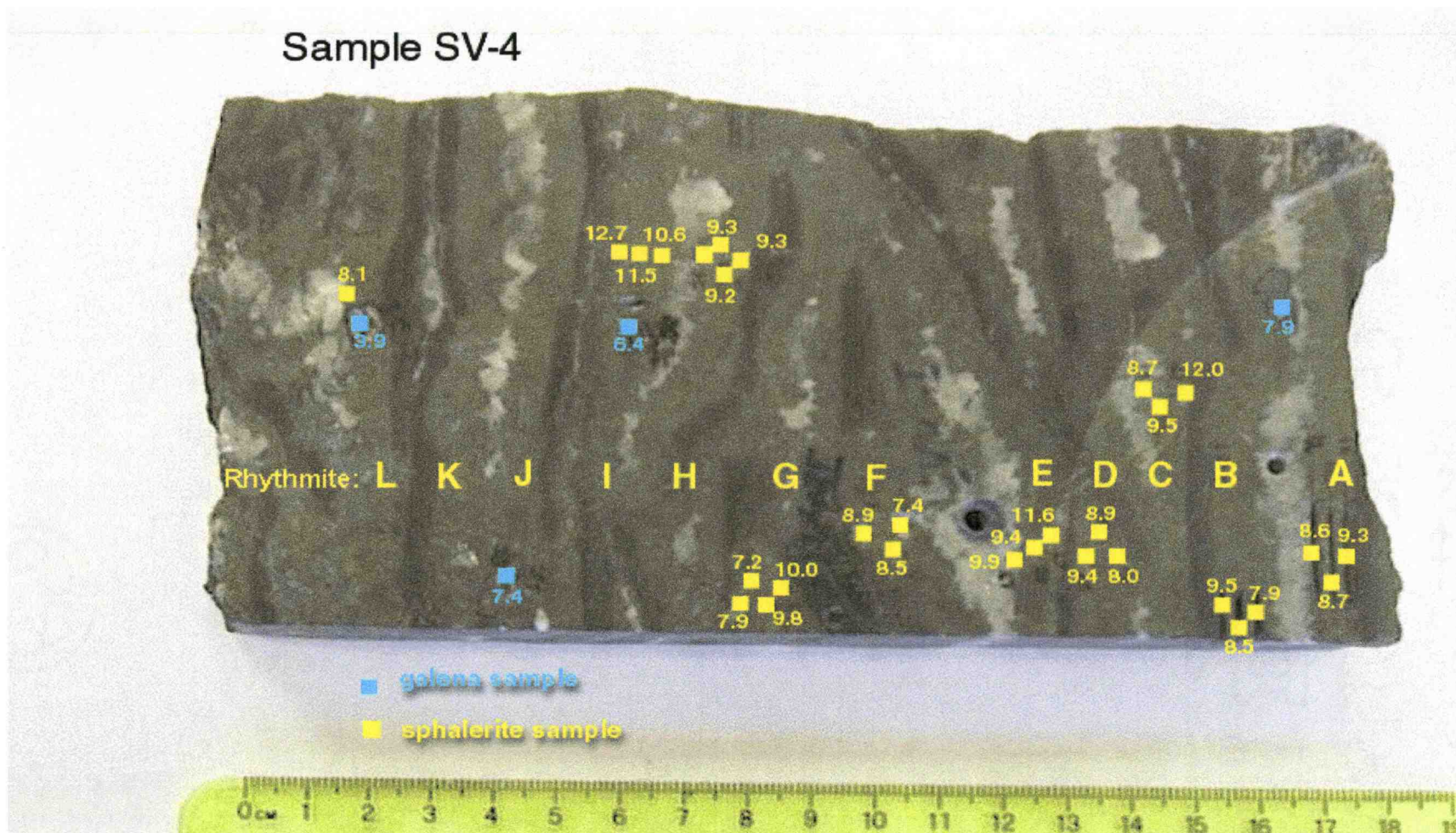


Figure 24. Location of sulfide concentrate samples (galena and sphalerite) on hand sample SV-4 (values are $\delta^{34}\text{S}$ in per mil).

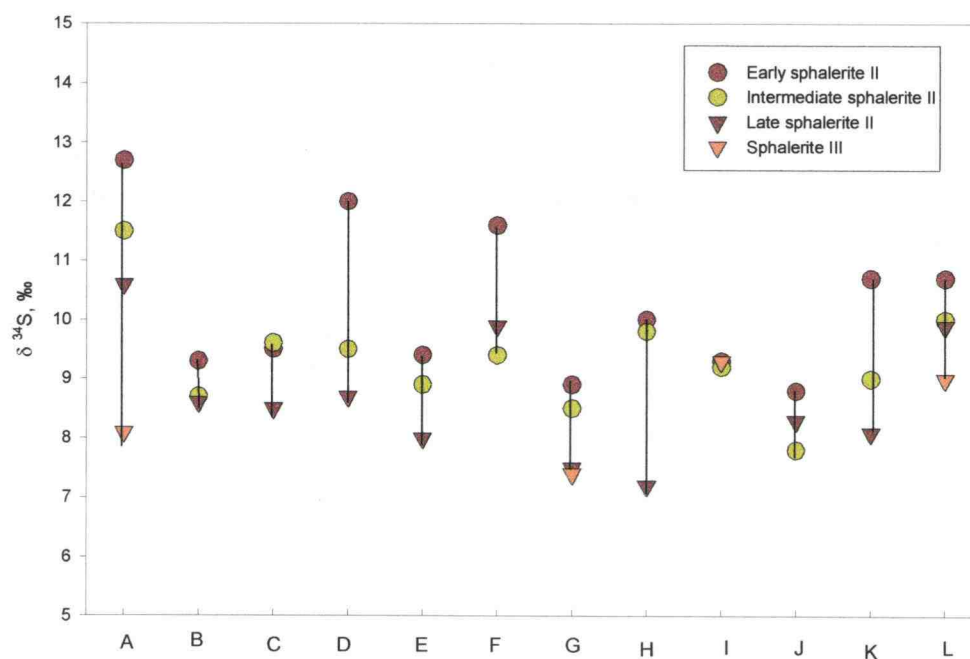


Figure 25. Plot of sulfur isotope $\delta^{34}\text{S}$ values from rhythmite bands of sample SV4 according to their paragenetic sequence.

The average $\delta^{34}\text{S}$ value of galena is 6.1 ‰ with a standard deviation of 1.5 ‰. Where possible, galena concentrates were extracted from areas immediately adjacent to sphalerite. However, some concentrates of galena from sample SV-4 were not collected close to coexisting sphalerite samples. Accordingly these analyses were not considered in the discussion of sphalerite-galena geothermometry.

Pyrite is a scarce accessory mineral in the ore. The low abundance and relatively small grain size of this mineral presented difficulties in the extraction of a sufficient amount of pyrite suitable for isotope analysis. A minimum of 1 to 3 mg was required. Nevertheless, it was possible to collect three concentrates, one from sample SV-5 and two derived from sample SV-1. The average $\delta^{34}\text{S}$ value is 7.6 ‰ with a standard deviation of 1.9 ‰.

The sulfur isotope data of the San Vicente deposit is distinct from other ore deposits of the Central Andes. The number of analyses, the range, mean, and standard deviation of $\delta^{34}\text{S}$ values of four other deposits are listed in Table 4. The mean and range of $\delta^{34}\text{S}$ values of sulfur, sulfide, and sulfate phases is illustrated graphically in Figure 26. The graph indicates a wider range in sulfur isotope values of the San Vicente deposit, and reflects the zonation of mineral phases. With the exception of San Vicente, a magmatic source of sulfur has been suggested in these deposits and mineralization occurs at higher temperatures. Sulfate is not present at the Casapalca and Cerro De Pasco deposit. Their sulfur isotope values have a relatively narrow range consistent with a magmatic sulfur source and higher temperature of precipitation.

Table 4. Summary of Sulfur Isotope Data of Ore Deposits in Central Peru.

Deposit / Source of data	Mineral / Phase	n	Mean	Range		s.d.
				from	to	
Cerro De Pasco (Ault & Kulp, 1959); (Einaudi, 1977)	Native Sulfur	1	-2.3 ‰			
	Pyrite	6	0.8 ₅ ‰	0.0	2.0	0.8
	Sphalerite	5	2.0 ‰	0.8	2.9	0.9
	Galena	6	-0.9 ‰	-1.8	-0.2	0.6
Morococha (Petersen, 1972) (Field, 1983, & unpublished data), (Field 1974, written communication)	Evaporite SO ₄	7	12.9 ‰	12	14.2	0.8
	Hydrothermal SO ₄	10	20.8 ‰	17.7	25.3	2.5
	Pyrite	14	3.0 ‰	1.3	4.9	1.1
	Sphalerite	3	3.3 ‰	2.5	3.8	0.7
	Chalcopyrite	4	3.0 ‰	2.1	4.7	1.1
	Galena	3	-0.3 ‰	-0.6	0.2	0.4
	Chalcocite	1	3.8 ‰			
	Enargite	1	0.6 ‰			
Casapalca (Rye and Sawkins, 1974)	Pyrite	4	1.1 ‰	0.7	1.4	0.4
	Sphalerite	19	1.0 ‰	-0.4	2.4	0.7
	Chalcopyrite	1	0.5 ‰			
	Galena	4	-1.7 ‰	-2.5	-0.8	0.7
	Bournonite	1	1.3 ‰			
	Tetrahedrite	1	1.7 ‰			
San Cristobal						
Vein Ores (Campbell, 1987)	Barite	<u>5</u>	16.1 ‰	15.3	18.5	1.4
	Pyrite	7	6.3 ‰	6.0	6.8	0.3
	Sphalerite	6	6.6 ‰	5.5	7.8	0.9
	Chalcopyrite	7	5.9 ‰	5.2	6.7	0.5
	Galena	7	4.6 ‰	4.1	6.5	0.9
Replacement Ores (Bartlett, 1984); (Field, unpublished)	Barite	5	16.4 ‰	14.3	19.7	2.2
	Pyrite	17	5.2 ‰	2.4	8.2	1.5
	Marcasite	1	7.5 ‰			
	Sphalerite	16	5.8 ‰	4.5	7.5	0.7
	Galena	10	2.8 ‰	1.6	4.2	0.8
San Vicente						
(Gorzawski et al, 1990):	Sphalerite	18	10.9 ‰	9.4	13	1.04
	Galena	2	6.8 ₅ ‰	6.8	6.9	0.07
(Spangenberg et al., 1999)	Anh(?)/Gypsum	2	18.2 ₅ ‰	15.6	20.9	3.7
	Native Sulfur	2	8.6 ₅ ‰	7.6	9.7	1.5
	Pyrite	4	10.2 ‰	8.1	12.2	1.7
	Sphalerite	25	10.7 ‰	5.7	14.2	2.4
	Galena	9	6.3 ‰	2.5	9.8	2.8
	Pyrite	3	7.7 ‰	5.6	9.3	1.9
This study:	Sphalerite	48	9.2 ‰	7.1	12.7	1.3
	Galena	6	6.0 ₅ ‰	3.9	7.9	1.5

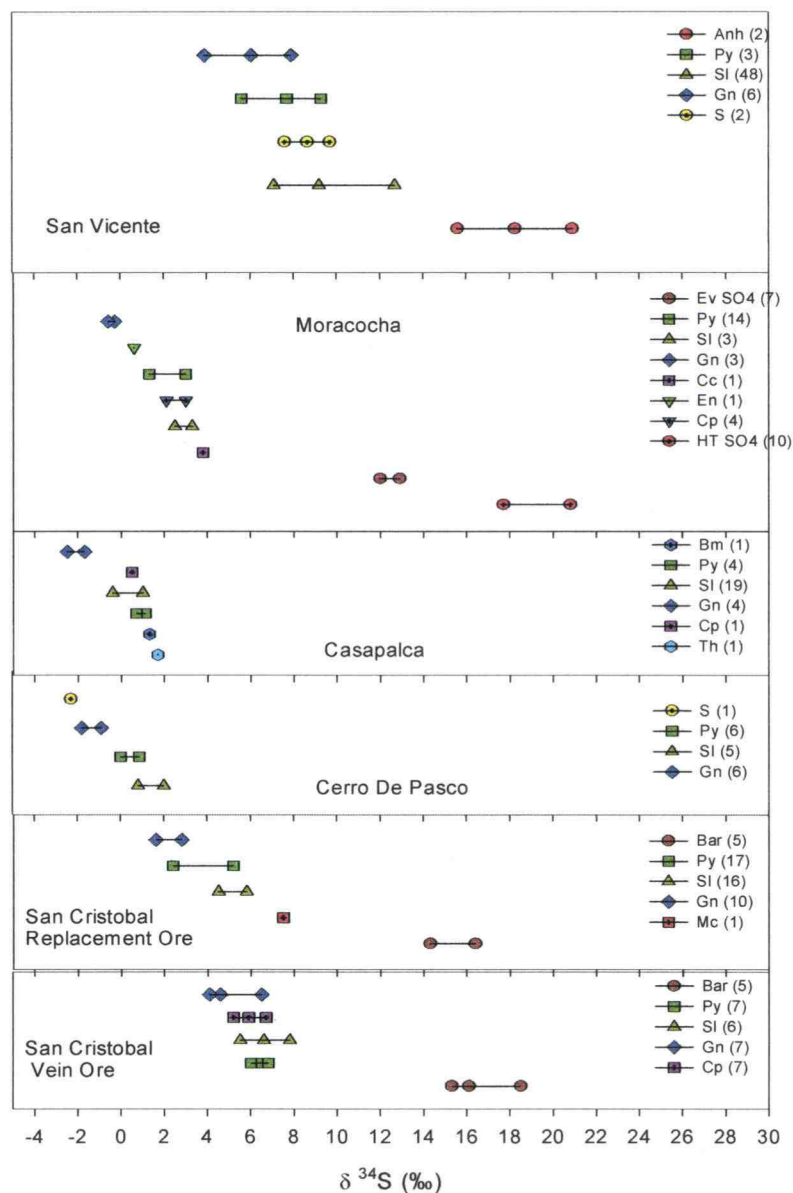


Figure 26. Sulfur isotope values of Central Peruvian Ore Deposits. Cp = chalcopyrite, Anh = anhydrite, Gn = galena, Sl = sphalerite, Py = pyrite, Bar = barite, Mc = marcasite, S = sulfur, Th = tetrahedrite, Bm = bournonite, HTSO4 = hydrothermal sulfate, EvSO4 = evaporitic sulfate, En = Enargite, Cc = chalcocite.

In contrast, hydrothermal ($20.8\text{ ‰} \pm 2.5\text{ ‰}$) and evaporitic ($12.9\text{ ‰} \pm 0.8\text{ ‰}$) sulfates were observed at the Morococha deposit by Petersen (1972; written communication 1974) and Field et. al (1983), and the San Cristobal deposit contains barite ($16.4\text{ ‰} \pm 2.2\text{ ‰}$) according to data by Campbell (1987), Bartlett (1984), and Field (unpublished). The fairly heavy $\delta^{34}\text{S}$ values suggest a possible influence of sedimentary sulfate from the Pucara Group of Triassic to Jurassic age. These deposits also have a larger variation of sulfur isotope values in the associated sulfides that can indicate lower temperatures of precipitation than those at the Cerro de Pasco and Casapalca deposits. Sulfur isotope variations in replacement ore are larger than those in vein ore of the San Cristobal deposit and support the possible influence of sedimentary rocks. This regional trend towards heavier and more differentiated sulfur isotope values may indicate the relative position of these deposits in their tectonic framework. Thus the isotopic data for sulfides of the Casapalca and Cerro de Pasco, in contrast to the heavier values and larger variation for those of Morococha, San Cristobal, and especially San Vicente, suggest a higher temperature of deposition and a closer affiliation to a likely magmatic source of sulfur ($\sim 0\text{ ‰}$). The heavier values presumably reflect the influence of evaporite or seawater sulfate and (or) deposition at lower temperatures and greater distances from deep-seated intrusions.

Source of Sulfur

Three potentially major geochemical sources of sulfur can be considered for the origin of sulfide-sulfur in the San Vicente deposit: (1) magmatic sulfur from intrusions, (2) sulfur from sedimentary sulfides, and (3) sedimentary sulfur from aqueous seawater sulfate and (or) evaporites.

In general, the isotopic composition of sulfide-sulfur that has originated from igneous sources is isotopically similar to that of meteorites. They have average $\delta^{34}\text{S}$ values close to 0 ‰ and range from -3 ‰ to +3 ‰ (Ohmoto and Goldhaber, 1997). On the other hand, seawater and sedimentary sulfates are enriched in the heavy isotope by approximately 10 to 30 ‰ depending on the geologic age. Sulfides of sedimentary origin have a wide range in $\delta^{34}\text{S}$ values (-70 ‰ to +50 ‰). They are typically depleted in heavy sulfur (^{34}S) as a result of biogenic isotopic fractionation and the mean is about -20 ‰.

A simple initial approach to determining the source of sulfur in the ore minerals is to compare the bulk sulfur isotopic composition ($\delta^{34}\text{S}_{\text{tot}} = 8.8 \text{ ‰}$) to the possible sources. This approach ignores the isotopic effects of fractionation, the mixing of magmatic and sedimentary sulfur sources, and effects caused by differing proportions of reduced (S^{-2}) and oxidized (S^{+6}) aqueous species of sulfur. Such simple interpretation should therefore be supported with detailed geologic and geochemical studies. Figure 27 shows a histogram of the sulfur isotope data of sphalerite, galena and pyrite from this study. The very narrow

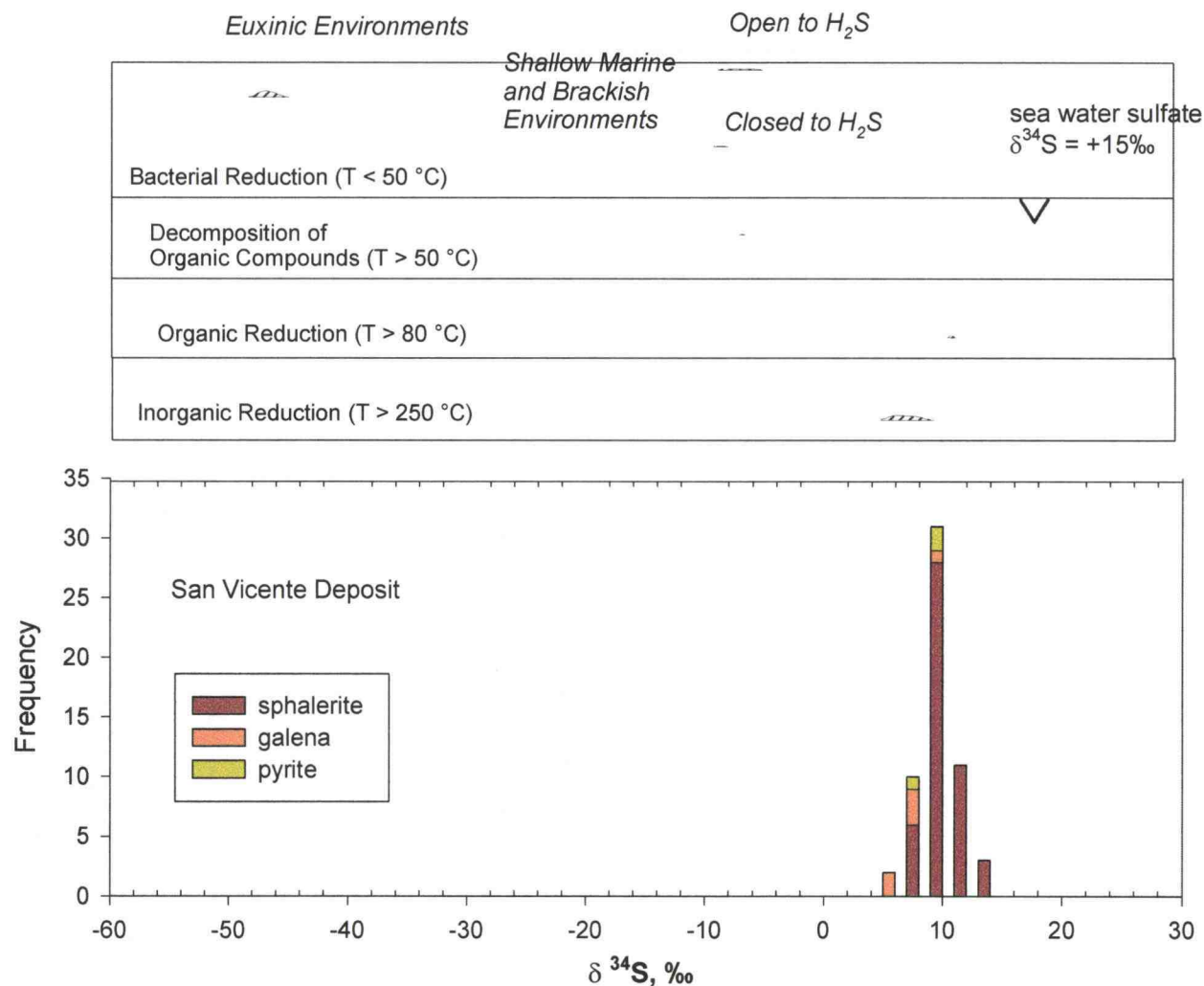


Figure 27: Histogram of sulfur isotope values from sphalerite, galena and pyrite from this study. Distribution patterns for $\delta^{34}\text{S}$ values of H_2S and sulfides when sulfate $\delta^{34}\text{S} = +15\text{‰}$ is reduced by various mechanisms are superimposed on the diagram.

distribution of the isotopic values are compared to possible sources based on comparison to well studied environments. The distribution of isotope values in environments where seawater of Triassic-Jurassic age has a $\delta^{34}\text{S}_{\text{sw}} = 15 \text{ ‰}$ is superimposed on the frequency diagram.

Magmatic fluids would have precipitated sulfides with values near 0 ‰. On the other hand, hydrothermal minerals may have isotopic compositions that are different from that of their original magmatic source. Studies by Sakai (1968) and Ohmoto (1972) have demonstrated from theory that the fugacity of oxygen and the pH of ore forming fluids, as well as temperature, are important controls in the isotopic composition of the sulfur-bearing minerals precipitated. Considering geologically reasonable variations in these parameters and an original sulfur composition of 0 ‰, Ohmoto (1972) demonstrated that sulfides can be produced with $\delta^{34}\text{S}$ values ranging from -26.5 to $+4 \text{ ‰}$. In another study by Ohmoto and Rye (1979), it was shown that $\delta^{34}\text{S}$ values larger than $+8 \text{ ‰}$ are not produced at temperatures below 200°C . $\delta^{34}\text{S}$ values different from 0 ‰ do not necessarily indicate sulfur from isotopically unique (sedimentary) sources, and conversely, that values near 0 ‰ do not have to be of magmatic origin. The observed bulk sulfur composition of $\delta^{34}\text{S} = 8.8 \text{ ‰}$ at San Vicente cannot be explained by a magmatic source of sulfur. However, it could be explained as either a mixture of magmatic sulfur and a source of heavy sulfur, or by fractionation of a single source of heavy sulfur (Ohmoto, 1972). Nonetheless, there is neither geologic evidence for mixing of magmatic fluids with connate formation waters in the Pucara Basin nor an indication of temperatures above

200°C. Therefore, it is unlikely that magmatic sulfur was the source.

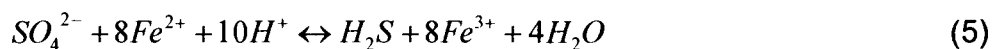
If sedimentary sulfides were the primary source of sulfur, the sulfides would be more likely to have a bulk composition of -20‰ , or lighter. Ohmoto and Rye (1979) give the range of $\delta^{34}\text{S}$ values in sedimentary sulfides as -70 to $+70\text{‰}$, and further state that they are typically depleted in $\delta^{34}\text{S}$ with a mean average of -17‰ . Bacterial reduction of seawater sulfate can produce sulfides of variable composition depending upon whether or not the system is open or closed with respect to SO_4^{2-} and H_2S . When the reduction of sulfate is slow with respect to the supply of sulfate, sulfides are typically depleted in ^{34}S by about -40 to -60‰ relative to seawater sulfate. These conditions are typically in deep euxinic environments. Sulfides with $\delta^{34}\text{S}$ values of -40 to -20‰ are expected assuming Mesozoic seawater sulfate compositions. Neither are such light sulfides observed at the San Vicente district, nor is geologic evidence available that would support the presence of such deep euxinic environments in the Pucara Basin.

Systems in which sulfate is reduced at a faster rate than its supply from seawater are considered closed with respect to sulfate. These are typically restricted shallow marine or brackish-water environments. Under such restricted conditions, hydrogen sulfide is continuously removed by precipitation of sulfides. The $\delta^{34}\text{S}$ values can range from -5 to $+70\text{‰}$ according to Ohmoto and Rye (1979). If the supply of metals is limited in such a system, the $\delta^{34}\text{S}$ values range from -5‰ to the $\delta^{34}\text{S}$ value of seawater sulfate of that geologic age. When the supply of metals is unrestricted, the isotopic composition of the

maximum population is approximately 25 ‰ lower than the corresponding seawater sulfate which is a function of geologic age. Rye and Ohmoto (1974) also note that under these conditions, the coexisting minerals will exhibit non-equilibrium relationships with respect to their $\delta^{34}\text{S}$ values.

seawater sulfate:

The $\delta^{34}\text{S}$ value of sulfate in seawater ranges from 10 to 25 ‰ during the Mesozoic. The rather narrow range and exclusively positive per mil values of $\delta^{34}\text{S}$ in sulfides from San Vicente appear to exclude sedimentary sulfide-sulfur as a possible source of sulfur. Reduction of seawater sulfate or sedimentary sulfate from marine evaporites are more likely to yield a bulk isotopic composition for H_2S of between 8 and 10 ‰. The moderately heavy $\delta^{34}\text{S}$ values suggest that the sulfur was derived from seawater or ancient evaporite that had undergone subsequent reduction by ferrous iron or organic compounds. Incorporation and fractionation of sulfate can produce the observed range of $\delta^{34}\text{S}$ values at the San Vicente mine. The presence of iron in clastic sediments and (or) bitumen in the carbonate host rock supports the thermochemical reduction of sulfate. In addition, previous research (Fontbote and Gorzawski, 1990) has indicated the presence of sulfate pseudomorphs in the clastic sediments of the basal series and the red sandstone of the Mitu Group. These formations are also generally considered to be the probable source of metals in the hydrothermal fluid. Inorganic reduction of seawater sulfate or sulfate-bearing evaporates can be accomplished by oxidation of ferrous iron in the reaction:



A geologic example of this mechanism has been described by Ohmoto and Rye (1979) for the formation of Kuroko type volcanogenic massive sulfide deposits in which seawater sulfate is considered to be the source of the sulfide-sulfur. For this reaction to proceed, there must be a source of reduced iron, excess sulfate and hydrogen ions. In addition, this reaction requires temperatures in excess of 250°C. It is important to note that the reaction (5) does not imply a particular mechanism of sulfate reaction. Indeed several reactions of intermediate sulfur species may be involved in the overall reduction mechanism, as discussed later. The supply of H^+ is limited in the surrounding carbonate host rock due to buffering by carbonic acid in the fluid. Because temperatures in Mississippi Valley type deposits are typically lower than 200°C, it may be inferred that temperatures in the stratigraphically deeper sedimentary rocks of the MVT Group were higher. The supply of reduced iron is probably restricted to sandstones and siltstones of the MVT group. The reduction of sulfate by organic matter has also been proposed for the generation of sulfide sulfur in MVT deposits.

Holser and Kaplan (1966) and Claypool et al. (1980) studied the variation of sulfur isotopes in ancient marine evaporites as a function of geologic time. Sulfate in evaporite deposits, such as gypsum and anhydrite, resembles closely the $\delta^{34}S$ values of seawater sulfate. The magnitude of post-depositional alteration limits the use of this age relationship. A significant change in the isotopic composition of marine sulfate occurred between Permian and Jurassic

time. Late Permian evaporates are characterized by $\delta^{34}\text{S}$ values near 12 ‰, whereas values of +12 to +15 ‰ are observed in sedimentary sulfide of Triassic age. In addition, Field et al. (1983) have reported $\delta^{34}\text{S}$ values of +13.1 and +13.8 ‰ for evaporitic anhydrite in the western part of the Pucara Basin. Because of the similarity of sphalerite sulfur isotope values (~ 9.5 ‰) to marine sulfate of the Triassic (+11 to 17 ‰; Claypool et al., 1980) it may be inferred that the source of sulfur was possibly a reduced form of this seawater sulfate.

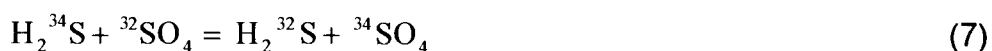
Of the sedimentary formations comprising the Pucara Basin, three contain lenses of evaporite sulfate: (a) the clastic sediments of the Late Permian to Early Triassic Mitu Group, (b) the Triassic Chambara Formation and (c) the Jurassic Condorsigna Formation. The red sandstones of the Mitu Group contain the evaporite replacement structures and are of Late Permian age. The isotopic signature of Mitu Group sulfate would therefore lead to heavier $\delta^{34}\text{S}$ bulk compositions. Sulfate derived from the evaporite-bearing Triassic carbonate units would also result in slightly higher bulk sulfide values. However, mixing of the sedimentary sulfate with an igneous source of sulfur might also generate a bulk isotope composition of +8.8 ‰. Igneous intrusions are possibly of similar age and abundant underneath the sedimentary basin (Fontbote and Gorzawski, 1990). The batholithic intrusions might also provide the required heat for sulfate reduction in the clastic sediments.

Sulfur Isotope Geothermometry

One of the most prominent applications of sulfur isotope studies is in relation to geothermometry. If isotopic equilibrium is established between mineral pairs such as ZnS and PbS in ore deposits, or between H_2S and SO_4^{2-} in hydrothermal fluids, isotope exchange reactions can be formulated, such as given by the reaction equations:



and,



In these examples (6) and (7), the isotopic fractionation factor (α) can be related to the equilibrium constant of the chemical system. The amount of fractionation of isotopes between two compounds in an equilibrium isotopic exchange reaction is proportional to mass differences between the isotopic compounds, and is inversely proportional to their temperature of equilibrium that approaches unity at high temperatures. At low temperatures, the potential amount of fractionation increases strongly, but because the kinetic reaction rates become slower, the assumption of equilibrium in the exchange reaction may not be valid. Temperature estimates are based on the isotopic differences between two minerals (A and B) expressed as a Δ_{A-B} value derived from the measured $\delta^{34}\text{S}$ values. The equation:

$$\Delta_{A-B} = \delta^{34}S_A \text{‰} - \delta^{34}S_B \text{‰} \cong 1000 \ln \alpha \quad (8)$$

relates the delta value (Δ), derived from the measured per mil values, to the

fractionation factor (α). If variations of the fractionation factor with temperature are known either from theory or experiment, the Δ value can be used as an estimate of the temperature of mineral deposition. This method assumes contemporaneity and equilibrium conditions between the two mineral phases, and that isotopic compositions have been preserved. The temperature of the sphalerite-galena thermometer is calculated from fractionation factors published by Ohmoto and Rye (1979) for ZnS-H₂S and PbS-H₂S isotopic equilibrations, and reformulated in terms of the following equation:

$$T[^\circ K] = \frac{0.85 \cdot 1000}{\sqrt{\Delta_{sl-gn}}} \quad (9).$$

Several assumptions are involved in the calculation of temperatures from isotope fractionation factors. A critical assumption is that isotopic equilibrium has been attained between the two mineral phases. The reaction rates between heavy and light sulfur species are temperature dependent. Equilibrium is reached faster at higher than at lower temperatures. Mineral pairs have to be cogenetic to be applicable in geothermometric calculations. For this reason, galena and sphalerite mineral pairs that are in close proximity were selected from the samples. Table 5 summarizes the results of the isotopic temperature estimates. Three mineral pairs were applied to geothermometric calculations. The Δ_{gn-sl} values (4.1 and 4.2) fall in a narrow range and indicate temperature conditions of 142 to 147°C. The uncertainty in the temperature is $\pm 15^\circ\text{C}$ based on an analytical uncertainty of 0.2 ‰. However, the isotopic composition of sulfides varies across the rhythmite. If the uncertainty is 0.5 ‰ due to isotopic

heterogeneity, the temperature uncertainty may be $\pm 30^{\circ}\text{C}$. Sulfur isotope values of galena-sphalerite pairs from Spangenberg et al. (1999) are also listed in Table 5. These authors did not calculate temperatures from their data, but the data suggest temperatures of between 128 and 152°C . Although it cannot be established from available sample descriptions that these minerals are truly cogenetic, the temperature estimates are within the analytical error and sampling uncertainty of this study.

Heavier galena samples were measured in samples SV-4 and SV-1A. For instance, rhythmite B in sample SV-4 had a galena crystal with $\delta^{34}\text{S} = 7.9$ ‰. At 145°C , the corresponding sphalerite would yield a $\delta^{34}\text{S}$ value of 12.2 ‰. Although associated sphalerite was not sampled directly next to this galena, similarly heavy sphalerites are present elsewhere in sample SV-4.

Table 5. Delta values of sphalerite-galena mineral pairs including isotopic temperature estimates.

Sample	Description	$\delta^{34}\text{S}_{\text{sl}}$	$\delta^{34}\text{S}_{\text{gn}}$	$\Delta_{\text{sl-gn}}$	Temperature	
					[K]	[°C]
SV7	Sphalerite-Galena pair in vein	9	4.8	4.2	415	142
SV4	sl-II - galena	8.1	3.9	4.2	415	142
SV1	sl-II - galena	10	5.9	4.1	420	147
FSV-0752	sl-gn	3.8	-0.7	4.5	401	128
FSV-0765	sl-gn	4.9	0.9	4.0	425	152

the uncertainty in temperature estimates based on 0.2 ‰ analytical error is ~ 10% (~15°C)

Isotope Fractionation Models

The observed sulfur isotope values of sphalerite, galena and pyrite vary systematically. Isotope fractionation models can be used to evaluate the physical and chemical conditions that have caused this variation. The most important physical parameter is temperature. It influences reaction rates and the value of the fractionation factor. Chemical parameters are oxidation state, pH, and speciation of sulfur compounds in the hydrothermal fluid. On the basis of these variables, three principal models were developed. These models are sulfate reduction to hydrogen sulfide (Model I), Raleigh fractionation of hydrogen sulfide (Model II), and effects of changes in pH and redox conditions (Model III).

Common input parameters to all three models are temperature and equilibrium conditions. Mississippi-Valley-type deposits are formed under relatively low temperature conditions. For example, studies of MVT deposits in the United States indicate temperatures of 50 to 100 °C for the S.E. Missouri District and 50 to 200 °C in the Illinois-Wisconsin and Hansonburg Districts. Fluid inclusion studies on dolomite-II at the San Vicente deposit indicate temperatures of 115 to 162 °C and salinities of 9.5 to 26 equivalent weight percent NaCl (Moritz et al., 1996).

Orr (1974) has suggested that the reduction of aqueous sulfates by organic matter may take place at temperatures above 80-120°C on the basis of

H_2S and SO_4^{2-} concentrations and temperature relationships in natural gas and oil. Oil field brines that have acquired sulfate from evaporites and (or) sulfate-rich connate waters may become sulfide-bearing hydrothermal fluids after circulation through organic carbon-rich sediments at temperatures well above 150 - 200°C. Organic reduction cannot cause complete conversion of SO_4^{2-} into H_2S over relatively short periods of time. Orr (1974) reported evidence that H_2S produced by organic reduction in natural gas and oil reservoirs has identical $\delta^{34}\text{S}$ values to that of associated evaporite beds. Therefore, it is likely that seawater sulfate of Late Permian to Triassic age was completely reduced to hydrogen sulfide in bituminous limestones of the Pucara Group. Provided this reduction was quantitative and complete, the isotopic values of hydrogen sulfide would be similar, if not identical, to the original sulfate source. Alternatively, the ferrous iron present in the underlying sandstone of the Mitu Group may also be considered as a potential reductant of sulfate. Again, the expected isotopic values would be similar to the original marine sulfate.

Model I Isotopic Variation Caused by Sulfate Reduction to Hydrogen Sulfide

The changes in sulfur isotope values during the reduction of sulfate to hydrogen sulfide may be predicted from theory (Ohmoto and Rye, 1979). The isotopic variations depend not only on temperature and proportions of aqueous sulfate and sulfide sulfur, but also the resulting $\delta^{34}\text{S}$ values depend on whether or not the system is closed or open with respect to both sulfide and sulfate sulfur. Environments in which the sulfate supply exceeds that consumed in the

reduction process are open with respect to sulfate. Conversely, if the reduction rate of sulfate is faster than the supply, the system is closed. Consequently, model I can be subdivided into four cases:

- Case 1. open with respect to SO_4 and open with respect to H_2S
- Case 2. open with respect to SO_4 and closed with respect to H_2S
- Case 3. closed with respect to SO_4 and open with respect to H_2S
- Case 4. closed with respect to SO_4 and closed with respect to H_2S

The input parameter and calculations relevant to Model I are described in Appendix 3. Sulfides in the San Vicente deposit may have formed in a closed system with respect to sulfate, because the amount of sulfate present in the evaporite source was probably finite as deduced from the lack of evidence for sulfate in the local sedimentary section. For these geologic reasons, only case 3 and case 4 need to be considered further, and case 1 and 2 of Model I can be excluded.

A Raleigh distillation process may be used to calculate the changes in $\delta^{34}\text{S}$ of residual sulfate and evolved hydrogen sulfide as a function of the fraction of sulfate to that of sulfide in the system. $\delta^{34}\text{S}$ values of SO_4^{2-} in a closed system and those of H_2S in an open and closed system (case 3 and 4) are calculated from:

$$\delta^{34}\text{S}_{\text{SO}_4^{2-}(t)} = \delta^{34}\text{S}_{\text{SO}_4^{2-}o} + 1000 \cdot \left(F^{(\alpha_{\text{H}_2\text{S}-\text{SO}_4} - 1)} - 1 \right) \quad (10)$$

Equation (10) is used to calculate the isotopic composition of sulfur in sulfate as a function of the fraction of remaining sulfate in the system during the

distillation process. $\delta^{34}\text{S}_{\text{SO}_4(t)}$ is the $\delta^{34}\text{S}$ value of sulfate at time t , $\delta^{34}\text{S}_{\text{SO}_4(o)}$ is the original $\delta^{34}\text{S}$ value at the beginning, F is the mole fraction of sulfate remaining at time t , and α is the isotopic fractionation factor. The $\delta^{34}\text{S}$ value of hydrogen sulfide in systems that are open and closed with respect to H_2S , are then calculated, respectively, from the following equations:

$$\delta^{34}\text{S}_{\text{H}_2\text{S}(t)} = \delta^{34}\text{S}_{\text{SO}_4^{2-}(t)} - 1000 \cdot (1 - \alpha_{\text{SO}_4^{2-}-\text{H}_2\text{S}}) \quad (11)$$

$$\delta^{34}\text{S}_{\text{H}_2\text{S}(t)} = \delta^{34}\text{S}_{\text{SO}_4^{2-}(o)} + 1000 \cdot (F^{(\alpha-1)} - 1000(1 - \alpha)) \quad (12)$$

Equations (11) and (12) are used to calculate the sulfur isotope composition of hydrogen sulfide in an open system as a function of isotope fractionation factor α (11) and fraction of hydrogen sulfide in the system (12). Equation (12) is obtained through substitution in equation (10) for the $(\delta^{34}\text{S}_{\text{SO}_4(t)})$ term of equation (11). Both equations (11) and (12) are valid for systems that are open with respect to hydrogen sulfide, and are equivalent. However, equation (12) is preferred as only the original isotopic value of sulfate is required in the calculation. Equation (10) and (12) represent case 3 of Model I where the system is closed with respect to sulfate, but open with respect to hydrogen sulfide.

The equation to calculate the isotopic composition of hydrogen sulfide in a closed system as a function of the remaining fraction of sulfate (F) is

$$\delta^{34}\text{S}_{\text{H}_2\text{S}(o-t)} = \frac{\delta^{34}\text{S}_{\text{SO}_4^{2-}(o)} - \delta^{34}\text{S}_{\text{SO}_4^{2-}(t)} \cdot F}{1 - F} \quad (13)$$

Equation 13, together with equation (10), represents case 4 of Model I, which is a system that is closed with respect to both hydrogen sulfide and sulfate. The variables in this equation are the same as in equation (10) and

(12).

Illustrated in Figure 28 are the results of such a calculation (equations 10, 12, and 13) based on an initial $\delta^{34}\text{S}$ value of +15 ‰ for seawater sulfate during the Triassic, and temperature conditions of 140 °C. Sulfate becomes enriched in $\delta^{34}\text{S}$ during the reduction (equation 10). Initially, any hydrogen sulfide is strongly depleted in $\delta^{34}\text{S}$ in H_2S -closed systems (equation 12) and is depleted by the $\Delta_{\text{H}_2\text{S}-\text{SO}_4}$ separation of about -46 ‰ at 140°C.

Hydrogen sulfide formed in open systems, but closed with respect to seawater sulfate (case 3 of Model I), would acquire progressively heavier $\delta^{34}\text{S}$ values with progression of the reduction process (equation 13). The corresponding $\delta^{34}\text{S}$ values of sulfur in sphalerite would become progressively heavier as well. Clearly, case 3 is not supported by the observed isotopic data and can therefore be excluded.

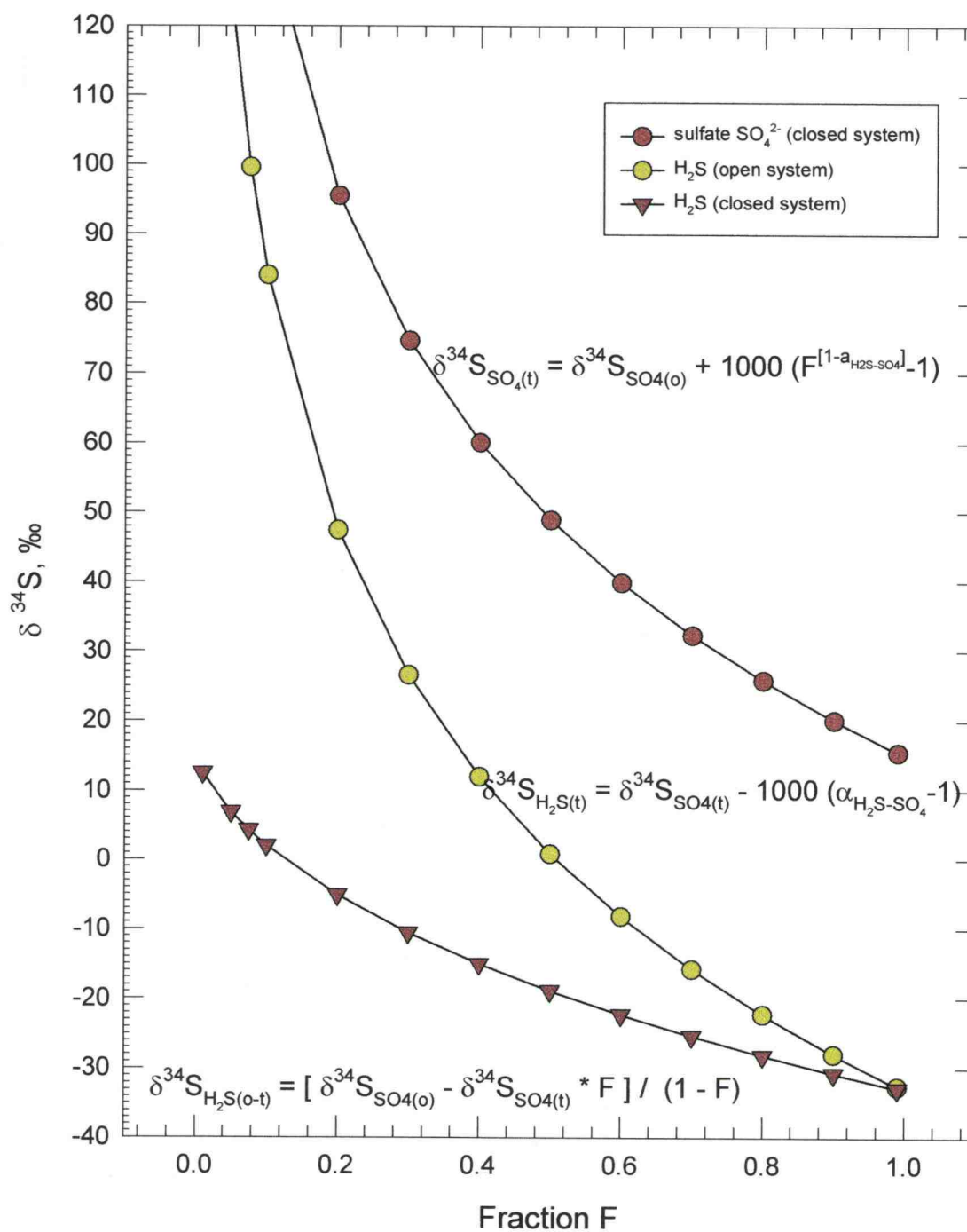


Figure 28. Plot of $\delta^{34}\text{S}$ values of sulfate (closed system with respect to SO_4) and hydrogen sulfide in an open and closed systems (with respect to H_2S) at 140°C .

Systems that are closed both to sulfate and hydrogen sulfide (case 4 of Model I) will have identical isotopic $\delta^{34}\text{S}$ values provided that the reaction goes to completion, and that the entire sulfate was reduced. Case 4 of Model I describes a system, where the reduction of sulfate is complete (closed with respect to SO_4), and the precipitation of sulfides is also complete (closed system with respect to H_2S). Hydrogen sulfide is constantly removed from the fluid by precipitation of metal sulfides. The rate of precipitation greatly exceeds the reduction rate of sulfide. As the remaining sulfate becomes progressively heavier, the remaining hydrogen sulfide becomes heavier as well. Consequently, the isotopic composition of sphalerite becomes heavier. The trend in $\delta^{34}\text{S}$ values of sphalerite can be calculated from:

$$\delta^{34}\text{S}_{sl,f} = \delta^{34}\text{S}_i + 1000 \cdot \left(F^{(\alpha_{\text{SO}_4-\text{H}_2\text{S}} - 1)} - 1 \right) + \Delta_{sl-\text{H}_2\text{S}} \quad (14)$$

, where $\delta^{34}\text{S}_{sl,f}$ is the composition of sphalerite at fraction F , $\delta^{34}\text{S}_i$ is the isotopic composition of the initial system (+15 ‰), and $\Delta_{sl-\text{H}_2\text{S}}$ is the isotopic separation between sphalerite and H_2S . Although the model qualitatively reproduces the trend of lighter sulfur isotope values in sphalerite, it predicts a much larger range (from +15 to more than -80 ‰) that is not supported by the analytical data obtained. Therefore, case 4 of Model I does not realistically describe the evolution of the hydrothermal fluid at a temperature of 140°C.

The fractionation factor of the sulfate-hydrogen sulfide pair is strongly temperature dependent. Reaction rates at high temperature are greatly enhanced, but the isotopic differences between sulfate and sulfide become smaller. This isotopic effect can be graphically illustrated by assuming that a

constant sulfate to hydrogen sulfide ratio was established at a high temperature. Subsequent cooling of the fluid causes re-equilibration of the isotopes according to the temperature dependent fractionation factor. Sulfate is variably reduced at high temperature (275°C) in the sandstone and the hydrothermal fluid is then cooled through 100°C as it ascends through the basin sediments. The isotopic composition of sphalerite precipitated from such cooling solutions at various H₂S to SO₄ ratios are shown in Figure 29. When the sulfide to sulfate ratio is 0.85 : 0.15, the observed range in isotopic values for sphalerite at San Vicente (7.1 to 12.7 ‰) is reproduced. Clearly, precipitation of metal sulfides causes this ratio to change in the aqueous phase. On the other hand, the isotopic exchange between hydrogen sulfide and sulfate may likely be kinetically inhibited at lower temperatures. However, isotopic equilibrium between sulfate and sulfide is a fundamental assumption in this model. Experimental evidence, summarized by Ohmoto and Goldhaber (1997), indicates that equilibrium is not obtained at temperatures below 200° to 175°C. Therefore, although the observed data are reproduced, this model may not describe successfully the evolution of the hydrothermal fluid.

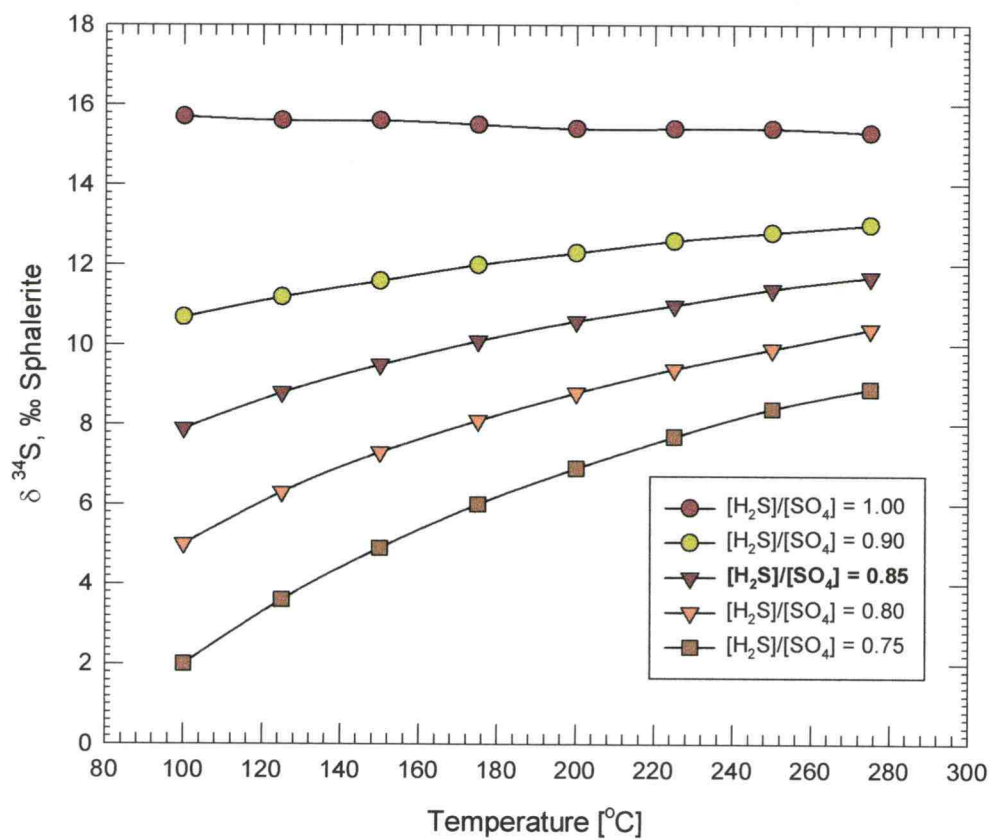


Figure 29. Evolution of $\delta^{34}\text{S}$ in sphalerite from a hydrothermal fluid at various sulfide to sulfate ratios over the temperature range from 275° to 100°C.

Model II Isotopic Variations in Sulfides due to Raleigh Fractionation of Hydrogen Sulfide

The second model represents a system where only hydrogen sulfide is initially present in the fluid (see Appendix 4). The reduced hydrothermal fluid precipitates sphalerite continuously until all hydrogen sulfide is consumed.

Isotopic compositions of sphalerite are calculated from the equation:

$$\delta^{34}S_{slf} = \delta^{34}S_i + 1000 \cdot \left(F^{(\alpha_{sl-H_2S}-1)} - 1 \right) + \Delta_{sl-H_2S} \quad (15)$$

, where the only change to the previous equation (14) is the fractionation factor α , which is the fractionation factor of the sphalerite-H₂S system at a given temperature. This simplified model does not account for any other sulfide phases that are co-precipitated from the aqueous phase. Sphalerite is the dominant sulfide phase in the ore deposit. Because the initial sphalerite is heavier than associated hydrogen sulfide in solution, this fractionation causes the residual H₂S and subsequent generations of sphalerite to become progressively lighter. Thus, the $\delta^{34}S$ values in sphalerite differ by 1.3 ‰ between early and late sphalerite at 145°C. This range has been observed in some rhythmities (sample SV-4: rhythmite D 1.4 ‰; rhythmite F 1.5 ‰), but other rhythmities indicate a larger difference between early and late sphalerite. For example, in rhythmite C of sample SV4, early and late sphalerite differ by 3.3 ‰. Perhaps fractionation between hydrogen sulfide and sulfides other than sphalerite, such as pyrite, account for the larger than predicted range.

Inclusion of pyrite enhances the simple model. Because the fractionation factor between hydrogen sulfide and sphalerite is rather small, the isotopic effect may be enhanced when sulfides with a larger fractionation factor are co-precipitated from the hydrothermal solution. The stabilization of pyrite in the latest stages of the mineralization was observed in the petrographic study of the ore. Although pyrite only occurs as a minor mineral in the main San Vicente ore, Spangenberg et al. (1999) have reported massive pyrite mineralization in the upper parts of the mantos ore bodies. This overall suggests that pyrite formed at a late stage in the mineralization process. Galena, on the other hand, may have formed earlier and in part during the precipitation of sphalerite. Assuming that the mole fraction of sphalerite, galena and pyrite is $X_{sl} = 0.85$, $X_{gn} = 0.09$ and $X_{py} = 0.06$ respectively, Raleigh fractionation of multiple sulfide compounds can be calculated. The fractionation factor is modified according to the mole fractions of the sulfides present as a function of temperature and the completeness of the reaction (F).

$$\alpha(F) = X_{sl} \cdot \alpha_{ZnS-H_2S} + X_{py} \cdot \alpha_{FeS_2-H_2S} + X_{gn} \cdot \alpha_{PbS-H_2S} \quad (16)$$

The dependence of the composite fractionation factor on the fraction of hydrogen sulfide remaining in the liquid has to be supported by petrographic evidence. Variations of $\delta^{34}S$ values in sphalerite, galena and pyrite as a function of the fraction of hydrogen sulfide remaining are shown in Figure 30.

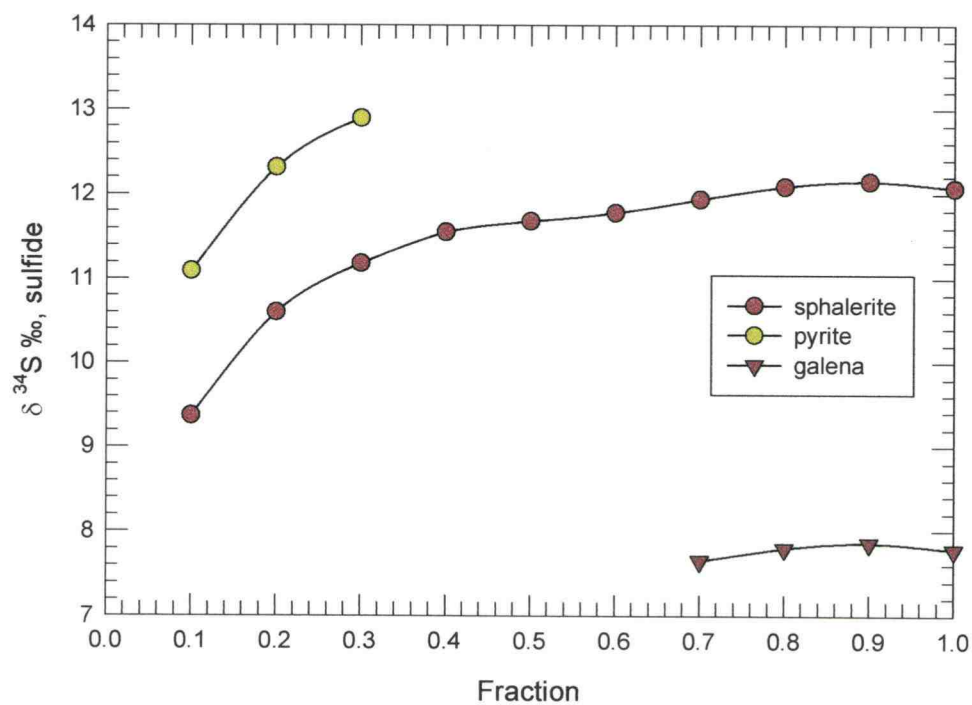


Figure 30. $\delta^{34}\text{S}$ values of sphalerite, galena, and pyrite calculated for Model II based on the mole fraction of sphalerite ($X_{\text{sl}} = 0.85$), galena ($X_{\text{gn}} = 0.09$), and pyrite ($X_{\text{py}} = 0.06$).

Petrographic evidence suggests that galena precipitated during the middle to late stages of mineralization, whereas pyrite formed in the later stages when approximately 70% of the hydrogen sulfide had been removed from the system. Model II successfully reproduces the measured isotopic variations of the ores. The presence of pyrite increases the overall range of early to late $\delta^{34}\text{S}$ values in sphalerite. Galena does not affect the isotopic composition of sphalerite as it forms throughout the mineralization. Heavier galena values (+7.9 ‰) co-precipitate with heavier sphalerite (12.1 ‰).

Model III: variations caused by changing pH and pe conditions

This model considers a geologic environment where sulfur is abundant, but in which the proportions of hydrogen sulfide and aqueous sulfate change with variations in pe and pH (see Appendix 5). Thus, the $\delta^{34}\text{S}$ values for sphalerite relate not only to temperature and fractionation factors, but also to variations in the proportions of reduced to oxidized species of sulfur as given by:

$$\delta^{34}\text{S}_{sl_f} = \delta^{34}\text{S}_t + \Delta_{\text{SO}_4-\text{H}_2\text{S}} - (\Delta_{\text{SO}_4-\text{H}_2\text{S}} \cdot X_{\text{H}_2\text{S}}) + \Delta_{\text{Sl}-\text{H}_2\text{S}} \quad (17)$$

, where $\Delta_{\text{Sl}-\text{H}_2\text{S}}$ and $\Delta_{\text{SO}_4-\text{H}_2\text{S}}$ are the per mil differences between $\text{ZnS}-\text{H}_2\text{S}$ and $\text{SO}_4-\text{H}_2\text{S}$ respectively, and $X_{\text{H}_2\text{S}}$ is the mole fraction of hydrogen sulfide in the system. The results of this model are portrayed in Figure 31 and compared to the previous two models.

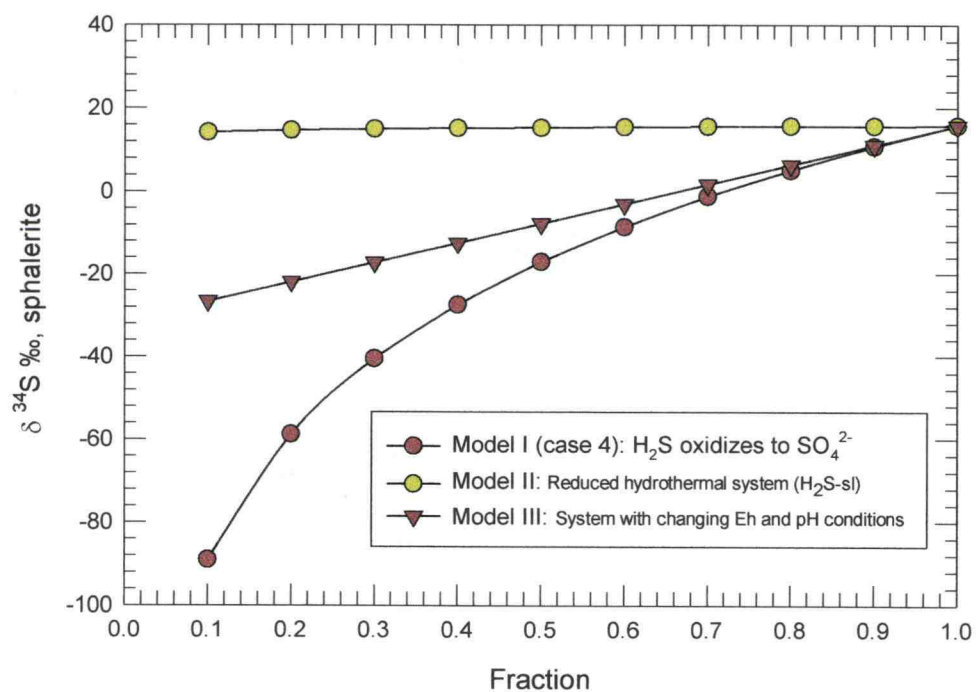


Figure 31. Possible models for the evolution of $\delta^{34}\text{S}$ values for sphalerite that involve changes in pH/pe conditions (Model III), reduction of sulfate to hydrogen sulfide (Model I), and Raleigh fractionation of hydrogen sulfide (Model II).

The variation of sulfur isotope values in sphalerite is a linear function of the sulfate to hydrogen sulfide ratio. The isotopic variations obtained from Model III are large ranging from 15.7 ‰ to -26.6 ‰, and these are not observed in the measured sulfur isotope values for the San Vicente deposit. Variations in sulfate to hydrogen sulfide ratios in the fluid apparently must have been relatively small during mineralization.

As was noted for Model I, reduction of sulfate in situ is unlikely, because large variations are expected in the sulfur isotope values when aqueous sulfide to sulfate ratios are variable. Model III indicates that variations in pH and pe were small at the site of sulfate reduction. This inference requires that ferrous iron is more abundant than sulfate in the clastic sediments, and that the sulfate underwent near total reduction. Alternatively, if sulfate was more abundant than ferrous iron in the source rock, then larger isotopic variations might be expected for the sulfides, and the sulfate to sulfide ratio might increase to the extent that sulfate minerals might have precipitated concurrently with the sulfide ores.

CHEMISTRY OF THE ORE-FORMING FLUIDS

The isotopic composition of bulk sulfur ($\delta^{34}\text{S}_{\Sigma\text{S}}$) in sulfides of the San Vicente deposit (~8 ‰) suggests that the source of sulfur is marine sulfate of Late Permian to Triassic age. The seawater sulfate was fixed initially as gypsum and (or) anhydrite in carbonate sediments and (or) the red sandstones underlying carbonates of the Pucara Group. Sulfate minerals that become dissolved in basin brines subsequently may be reduced to hydrogen sulfide. Two principal reduction mechanisms are considered likely in the geological context: (1) thermochemical reduction by organic matter and (2) thermochemical reduction of sulfate by ferrous iron in clastic sediments of the Mitu Group. The reduction by ferrous iron in underlying sediments implies that the hydrothermal fluids transport hydrogen sulfide to the carbonate host rock, whereas reduction of sulfate by organic matter suggests transport of sulfate in the fluids to the site of reduction and sulfide deposition. Thermodynamic models of the hydrothermal fluid, and sulfur isotope data for these contrasting hypotheses are evaluated using sulfate-sulfide molecular reaction mechanisms.

Geochemical Modeling of the hydrothermal fluid

The chemical and physical properties of the hydrothermal fluid influence the precipitation of sphalerite and galena. Temperature, acidity (pH), redox potential (pe) and speciation of solutes can be estimated and constrained to a finite range of values and components. Electron activities are usually expressed

on either of two scales, pe or E_H . The parameter pe provides a nondimensional scale as opposed to E_H that is measured in volts. The pe is a more useful measure of redox conditions, because it directly relates to the number of electrons transferred in a reaction. The two scales are related by:

$$E_H = \frac{2.3RT}{F} pe \quad (18),$$

where E_H is the redox potential in volt, R is the gas constant, T is temperature in Kelvin, F is the Faraday constant, and pe is the non-dimensional redox potential parameter.

The temperature range of the fluid is constrained by independent evidence. Fluid inclusion studies of the white sparry dolomite-II indicate precipitation from hot (115 to 162°C) and saline (9 to 26 wt % NaCl equivalent) fluids (Moritz et. al., 1996). This temperature range is consistent with results of the sphalerite-galena sulfur isotope geothermometry of this study. In addition, numerous studies of the North American MVT deposits yield similar temperatures.

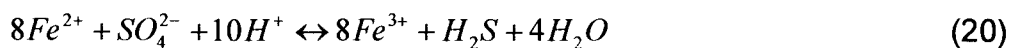
The pH of the fluid is not well known. Spangenberg et al. (1999) have speculated that the pH of the mineralizing fluid is slightly acidic (5 to 6) and mainly controlled by carbonate dissolution until completely buffered by the host dolomite. No direct observation or evidence was cited for this estimate. The pH of the fluid would have been initially slightly basic, if formation water in the carbonate sequences resembled trapped seawater. However, the fluids may have become more acidic (pH: 2-3) if reduction of sulfate had taken place at higher temperatures in the clastic sediments.

The redox potential of the fluid largely controls the speciation of sulfur. In anoxic waters that are depleted in oxygen through the oxidation of organic matter, sulfate becomes the primary oxidant. Although there likely may exist important intermediate sulfur compounds such as thiosulfate, dithionate, native sulfur and hydrogen polysulfides, the general redox reaction usually proceeds all the way to the formation of sulfides and can be written as follows:



This simplified reaction includes only the sulfate and sulfide species of sulfur.

Previous workers have not considered the possibility of sulfate reduction by mechanisms other than by organic matter at the site of deposition. Because the underlying red sandstones are relatively large reservoirs of both metals and sulfate, ferrous (Fe-II) iron may have been originally abundant in these sediments. The leaching of metals from sedimentary and igneous source rocks presumably requires fairly acid and probably chloride-rich solutions. Therefore, the reduction of sulfate might be accomplished by a reaction formally written as:



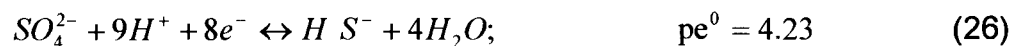
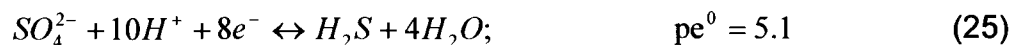
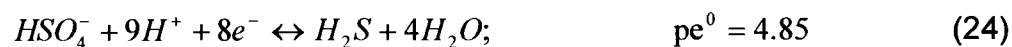
Inorganic reduction of sulfate both by ferrous iron and by reduced carbon can be equally well described by these formal reactions. Both reactions are charge and mass balanced, but they only describe a net reaction. A particular reaction mechanism on a molecular level is not implied.

Construction of the pH-pe diagram

The sulfate and sulfide aqueous species are related by the following reactions:



The relationships between pe and pH for these reactions may be derived from the mass action laws for the following additional equations:



A pe-pH diagram of zinc in the carbonaceous sulfate-sulfide system can be constructed from these data. Additionally, it has been assumed that this system is closed with respect to hydrogen sulfide and carbon dioxide.

Carbonate ions are certainly present in the aqueous phase, and must be considered in the construction of pe-pH diagrams at 25°C. The concentration of carbonate was assumed to be 10^{-2} M, while the concentration of total sulfur in the system may be 10^{-4} M. The lower limit of zinc in the system was estimated to be 10^{-8} M. The metal can form either a carbonate (smithsonite, $pK_s = 10.26$), an hydroxide ($Zn(OH)_2$, $pK_s = 11.14$), or a sulfide (sphalerite, $pK_s = 24$). All

calculated from the mass laws. The pe-pH diagram so contoured is given in Figure 32. Three possible scenarios can be deduced from the diagram: (A) a fluid that carries reduced sulfur becomes neutralized as it encounters the dolomite host rock; (B) a sulfate brine becomes reduced by organic matter in the host rock; and (C) changing redox/pH conditions at the site of deposition. The different pathways need to be evaluated using geologic and geochemical considerations.

Although organic matter is abundant in the carbonate, the reduction of a sulfate bearing brine by organic carbon at the depositional site is unlikely, because this potential reductant remains present and largely unreacted. At the very least, a zone of bleached host rock in contact with the sulfides would be expected. Evidence for variations in pH and redox conditions in the host consist of the dissolution of carbonate. Although the buffering capacity of a fluid saturated with carbonic acid precludes spontaneous changes in the pH of the mineralizing fluid, neutralization of an acidic fluid in the dolomite host rock is supported by evidence of hydraulic breccias and the enhanced solubility of metals under low pH conditions. The fluid presumably obtained and transported scavenged metals from the underlying source rocks.

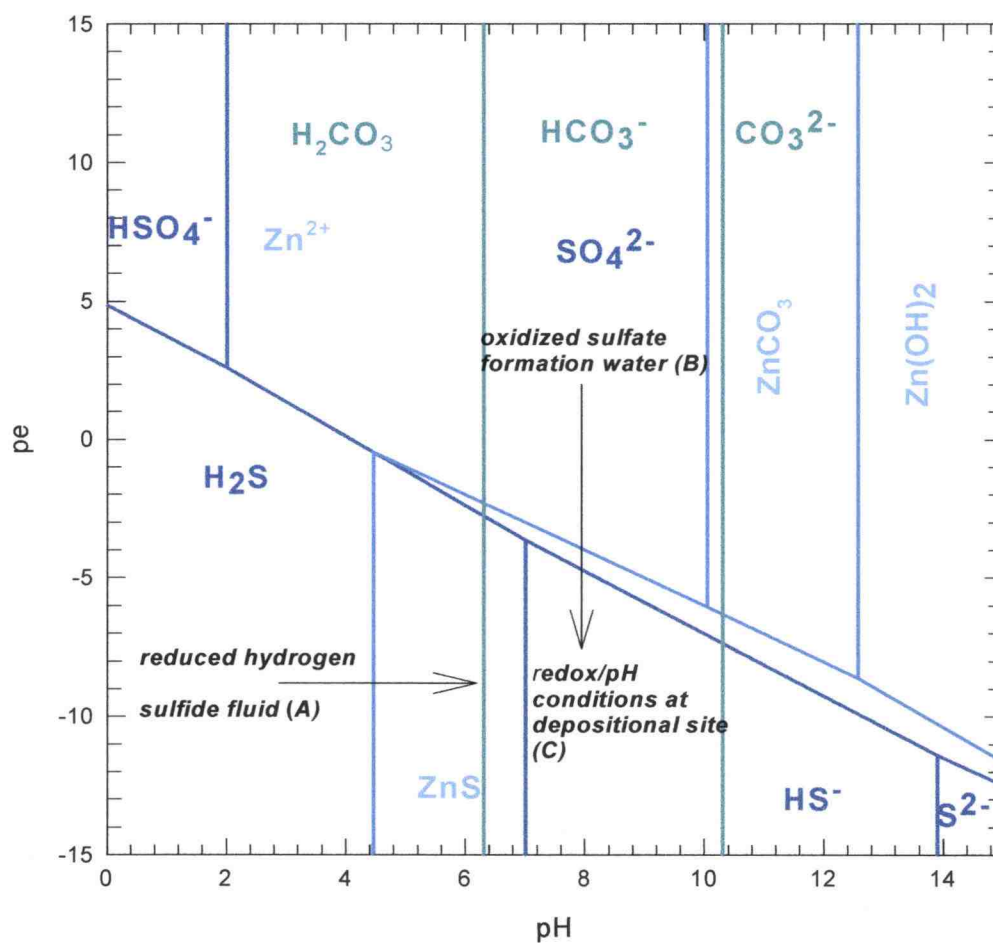


Figure 32. Plot of the aqueous zinc-sulfur-carbon system at 25°C with respect to pe and pH.

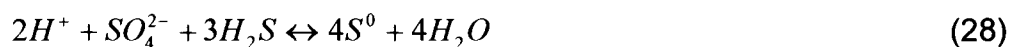
Molecular Reaction Mechanism of Sulfate Reduction

The reduction of sulfate to hydrogen sulfide involves intermediate sulfur compounds. The oxidation state of sulfur in sulfate is +VI, whereas sulfide contains sulfur in the -II oxidation state. Toland (1959) studied the reaction mechanism of sulfate in aqueous solutions at high temperature. The reaction rates are enhanced by initiator compounds. In particular, the presence of bisulfide accelerates sulfate reduction. Sulfate itself does not initially attack hydrocarbons when organic matter is the only reductant present. Reaction rates are faster in acidic than in basic solutions.

The reaction rates provide important information on the precise mechanisms of sulfate reduction. The fluids must be acidic and at temperatures above 250°C to effectively reduce sulfate to hydrogen sulfide. Also, it should be noted that the SO_4^{2-} - H_2S reduction (equation 19) is not achieved in a single step, but most likely involves stepwise reduction by means of intermediary compounds such as thiosulfate, native sulfur, and polysulfide-sulfite chains (polythiosulfonate). As this reaction proceeds to the product side, the fluid becomes progressively less acidic and ferric iron oxides may precipitate. The removal of iron from the fluid may explain the generally negligible abundance of this metal in the deposit. Most importantly, the pe-pH diagram (Figure 32) indicates that it is possible to transport larger concentrations of hydrogen sulfide and Zn^{2+} in acidic solutions. Acidic brines are also capable of dissolving the

carbonate host rock, and thus becoming neutralized in the process. The solubility of sphalerite also decreases rapidly with increasing pH as the fluid follows the path A-C in Figure 32.

Alternatively, one may consider sulfate reduction by organic carbon in the dolomite host rock. This hypothesis requires that sulfate be reduced to H_2S at the site of deposition. Seawater sulfate was fixed as gypsum and/or anhydrite lenses in the Pucara dolomite, and to a lesser extent in the red sandstones of the Mitu Group. The effectiveness of thermochemical reduction of sulfate remains very controversial at sedimentary temperatures that prevail during diagenesis. Orr (1974) has studied sulfur concentrations and sulfur isotope ratios in oil reservoirs and observed a trend towards decreasing sulfur concentrations, while the isotopic ratios increased towards heavier sulfur. The formal mechanism of thermochemical sulfate reduction is expressed by the reactions:

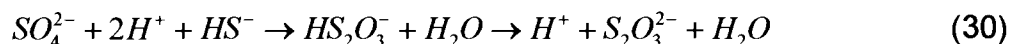


where 'CH₂O' represents the organic matter in the sediment. The reactions indicate that intermediate sulfur compounds such as native sulfur may play an important role in this process. Reduction of sulfate in the presence of hydrogen sulfide may also produce thiosulfate according to Pryor (1962) in near neutral solutions over the temperature range of 250 to 300°C.

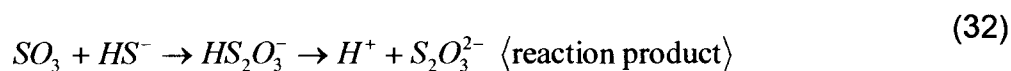
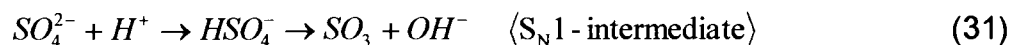
Two important reaction mechanisms may be involved in the reduction of sulfate to sulfide. A bimolecular reaction (S_N2) and a unimolecular reaction

mechanism (S_N1) are potentially involved. The free energy of activation ΔG , and therefore the rate of reaction in bimolecular reactions (S_N2), depends on the reactivity of both the nucleophile and the reacting molecule to undergo that reaction. Therefore, the reacting molecule must be present in an activated state. Bimolecular reaction rates (S_N2) are second order, in contrast to unimolecular reactions (S_N1) that are characterized by first order reaction rates. The reacting molecule forms an intermediate activated molecule and reacts with an activated nucleophile.

The bimolecular reaction (S_N2) of sulfate with bisulfide occurs in slightly acidic solutions:



A unimolecular (S_N1) reaction mechanism is observed in alkaline environments:



The two reactions have very different reaction mechanisms. The S_N1 reaction is unimolecular and requires the activation of the molecule to its transition state. The nucleophile (HS^-) only interacts with the excited state of the electrophile (SO_3^-). Consequently, the reaction rate depends on the formation of the excited state, but not on the amount of nucleophile or products. In contrast, bimolecular nucleophilic substitutions (S_N2 reactions) are strongly dependent on the concentrations of the reactants (eq. 30). The presence of hydrogen (H^+)

increases the nucleophilic substitution of bisulfide on sulfate when thiosulfate is formed. It follows that for solutions with a lower pH, the amount of thiosulfate should increase in proportion to the hydrogen concentration.

Ohmoto and Goldhaber (1997) summarized experimental studies of the thermochemical sulfate reduction mechanism and concluded that the reaction rates are extremely slow and are at 125°C approximately 10^{-9} to 10^{-10} mol/l-year. Therefore long periods of time are required to generate substantial concentrations of H_2S . Consequently, isotopic disequilibrium in associated ore deposits is to be expected. The reaction rate experiments cited by Ohmoto and Goldhaber (1997) were carried out under conditions where the S_N1 reaction mechanism was prevalent. The petrographic evidence of equilibrium textures and formation of breccia structures, may thus, favor an acidic environment where the sulfate reduction occurs more rapidly by the S_N2 reaction path.

The hypothesis of sulfate reduction at the site of deposition must also be evaluated considering the source of the metals in the deposit. Near seawater compositions of the connate water in Pucara sediments would result in basic to neutral brines. Under such high pH conditions, the capacity to leach significant amounts of zinc and lead from detrital sediments is lower than in acidic environments. Accordingly, more efficient leachability leading to the formation of a Zn-Pb orebody, therefore, favors acidic conditions in the metal bearing solution.

Speciation of Solutes in the Hydrothermal Fluid

The computer program MINEQL+ (Environmental Research Software, 1998) was used to model the speciation of solutes in two hydrothermal fluids as a function of temperature. The first system is of a fluid that represents a sulfate-brine, and the system is a fluid in which hydrogen sulfide is the primary sulfur component. Both fluids modeled have a fixed pH of 6 and a sodium chloride concentration of 1 mol/liter. The calculation is based on a system closed to carbon dioxide and having a total carbonate concentration of 10 mmol/liter. The sulfate brine contains 30 mmol/liter total sulfate and 10 $\mu\text{mol/liter}$ Zn. In contrast, the hydrogen sulfide fluid has 1 $\mu\text{mol/liter}$ H_2S and 1 $\mu\text{mol/liter}$ Zn. Sphalerite is allowed to precipitate as a solid phase in each of the model calculations. These compositions, as enumerated, are believed to be a reasonable approximation for the two different models.

The speciation of zinc in the sulfate brine is illustrated in Figure 33. Zinc forms chloride complexes in the temperature range between 60 and 160°C. The most abundant complex is zinc tetrachloride (ZnCl_4^{2-}). Zn^{2+} ions at room temperature are more abundant than those of the chloride complexes. Bicarbonate and sulfate complexes of zinc are very low in abundance over the entire

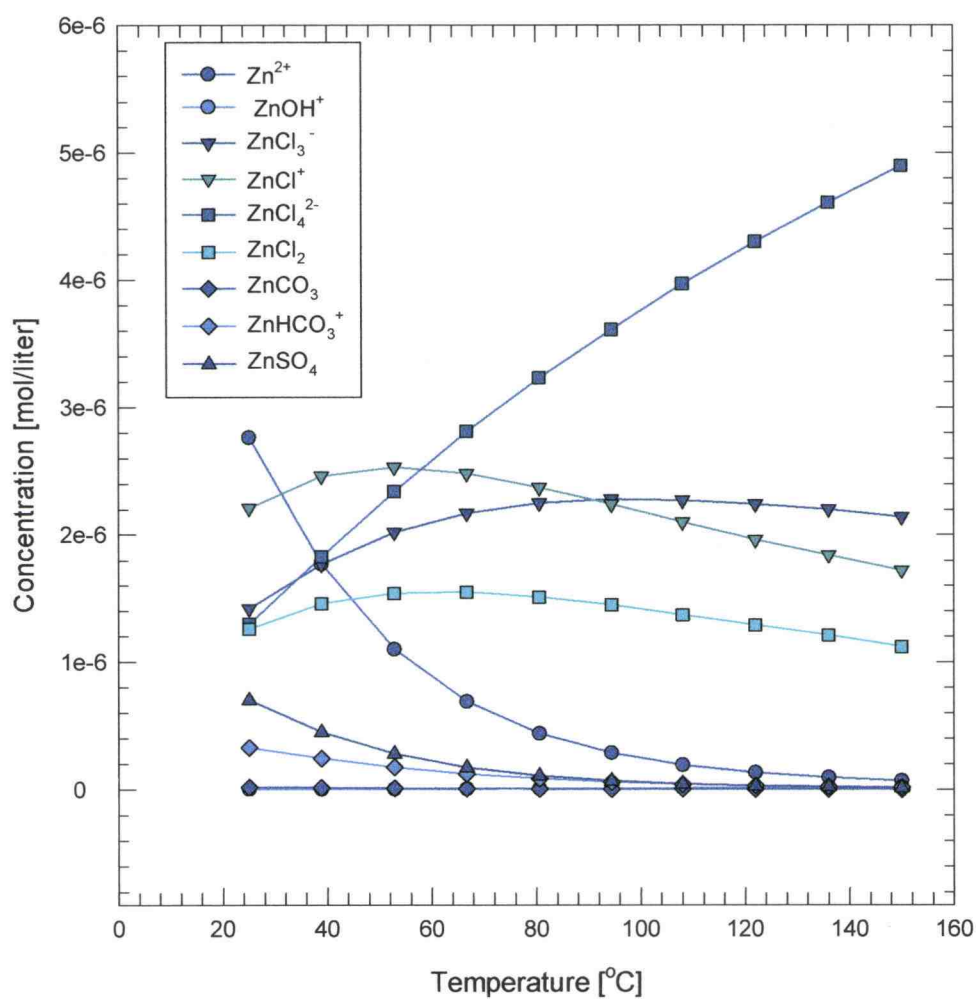


Figure 33. Speciation of zinc in sulfate solutions as a function of temperature.

temperature range. The results indicate that zinc would be transported primarily as the tetrachloride-complex and that sulfur is available as sulfate in the solution. In addition, the brine can transport large quantities of sulfate and metals ($> 10^{-2}$ mol/liter) simultaneously. Precipitation of zinc does not occur until hydrogen sulfide is formed by sulfate reduction.

The sulfide-bearing fluid has a markedly different behavior as a function of temperature. As shown in Figure 34, sphalerite precipitates at temperatures below 175°C when the concentrations of zinc and hydrogen sulfide are larger than 1 $\mu\text{mol/liter}$. At nearly all temperatures, the chloride complexes ($\text{ZnCl}_4^{2-} > \text{ZnCl}_3^- > \text{ZnCl}^+$) are more abundant than the neutral sulfide $\text{Zn}(\text{HS})_2$ complex. Fluids that contain reduced sulfur have therefore only a very limited capacity to transport metals and sulfur at concentrations above 1 $\mu\text{mol/liter}$ and temperatures below 150°C. The decrease in temperature and the neutralization of the acidic hydrothermal solution causes rapid destabilization of the metal-chloride complexes. This causes precipitation of sphalerite, galena and pyrite.

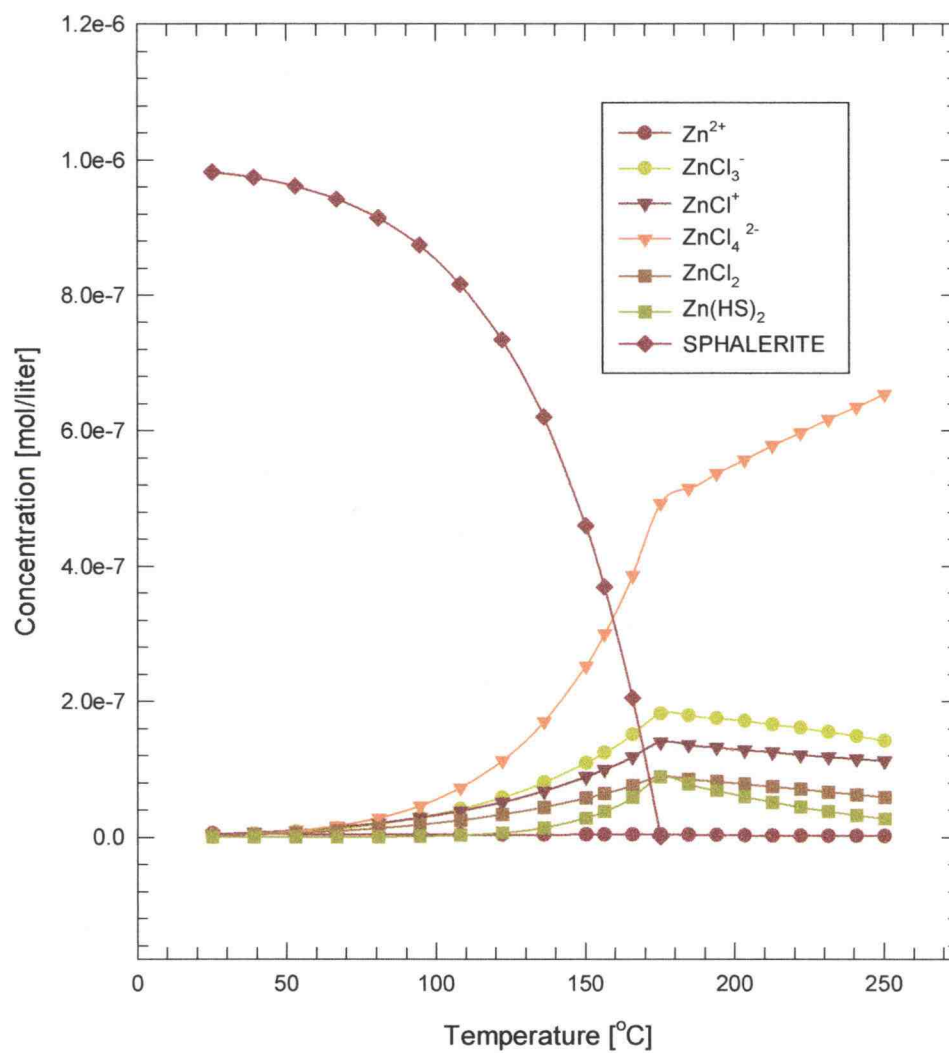


Figure 34. Speciation of zinc in sulfide solutions as a function of temperature.

GENETIC MODEL OF ORE DEPOSITION

This research provides important information regarding future exploration criteria for both additional MVT deposits in the Pucara Basin of Peru and as yet undiscovered Zn-Pb deposits in similar geologic settings. A genetic model consistent with the observations is the foundation for a successful exploration strategy. The source of metals and sulfur, the mechanisms of sulfate reduction, the migration of fluids, and the precipitation of sulfides in the carbonate host rock are all critical parameters. The genetic model presented here is based on the observation of textural features in hand specimen, chemical trends, and the integrated interpretation of these features and trends.

Clastic sediments, underlying the carbonate sequence, are believed to be the source of metal. Due to the behavior of zinc during chemical weathering, its major accumulation in the sedimentary environment is to be expected in detrital matter. However it should be noted that detrital minerals such as quartz, muscovite, feldspar and biotite do not contain appreciable amounts of structural zinc. Zinc is more abundant when adsorbed on surfaces of illite and other clay minerals and Fe-Mn oxides. Alternatively, zinc may also be enriched in colloidal iron oxides and iron oxide coatings of detrital and secondary minerals.

Wedepohl (1964) studied the relationship between zinc and iron oxide in red Triassic sandstones. Sandstone concretions with 22 wt. % Fe_2O_3 had a zinc concentration of 760 ppm. Lead has a similar geochemical behavior as zinc. Zinc and lead are more concentrated in chemically incompletely weathered

rocks. Coarse sandstones and molasse sediments are usually not completely weathered and reflect rapid deposition. Ferrous iron may be abundant and an effective reductant of sulfate. Connate waters may be acidic due to ion exchange mechanisms on silicate and oxide mineral surfaces.

Connate waters possibly also carry sulfate derived from the dissolution of sulfate-bearing evaporite minerals contained in both carbonate and sandstone units. Although the solubility of sulfate minerals does not increase with temperature, they have relatively high solubility products.

Connate waters are gradually replaced with fresh meteoritic water. The recharging fluid is undersaturated with respect to calcium and sulfate and is more acidic. Therefore, the fluid will continuously dissolve the sulfate minerals (anhydrite and gypsum).

The reduction of sulfate has most likely occurred in the sandstone and not in the carbonate host rocks. Several observations provide supporting evidence for this hypothesis. Ferrous iron in the sandstone is oxidized to ferric iron. The sandstones owe their red color to the presence of ferric iron. Conversely, organic matter in carbonates is present and has not been bleached, reacted, or extracted from these rocks. Sphalerite replaces bituminous dolomite and grows over organic matter without signs of dissolution or oxidation of bitumen. Geothermometric calculations of sulfur isotopes on sphalerite-galena pairs indicate a temperature of precipitation of approximately 150°C. At these temperatures, reaction rates for the reduction of sulfate by organic matter are extremely slow. Temperatures in the deeper part of the

sedimentary basin are considerably higher. The stratigraphic separation between the ore deposit and red sandstone is approximately 1350 m. Assuming a normal geothermal gradient of 30°C/km, the estimated temperature differential is about 40°C. Under the assumption that the stratigraphic units dip at 45°, the vertical separation between host rock and clastic source rock becomes even larger. An increase in temperature of 60 to 80°C would be expected. Therefore, reaction rates of inorganic sulfate reduction are enhanced in the deeper part of the basin.

The oxidation of ferrous to ferric iron decreases the pH of the fluids. Under conditions of lower pH, the reduction of sulfate is enhanced. The molecular mechanism of sulfate reduction progresses stepwise and forms intermediate products such as thiosulfate and sulfite. Thiosulfate, in acidic solutions, is formed by a bimolecular nucleophilic substitution of oxygen by bisulfide. In basic solutions, bisulfate initially forms sulfite by separation of a hydroxyl group. The sulfite then undergoes a slow unimolecular nucleophilic substitution with bisulfide to form thiosulfate.

A schematic cross section that illustrates the genetic model is presented in Figure 35. The arrows indicate the direction of flow of fluids in the sedimentary basin. Igneous intrusions may have provided heat to cause convection in the fluid system. The solution becomes enriched in zinc and lead. Faults in the basin may have provided hydrological conduits for fluids to move into upper parts of the basin where they encounter drastic changes in the host rock chemistry. The higher pH and lower temperature cause mineralization.

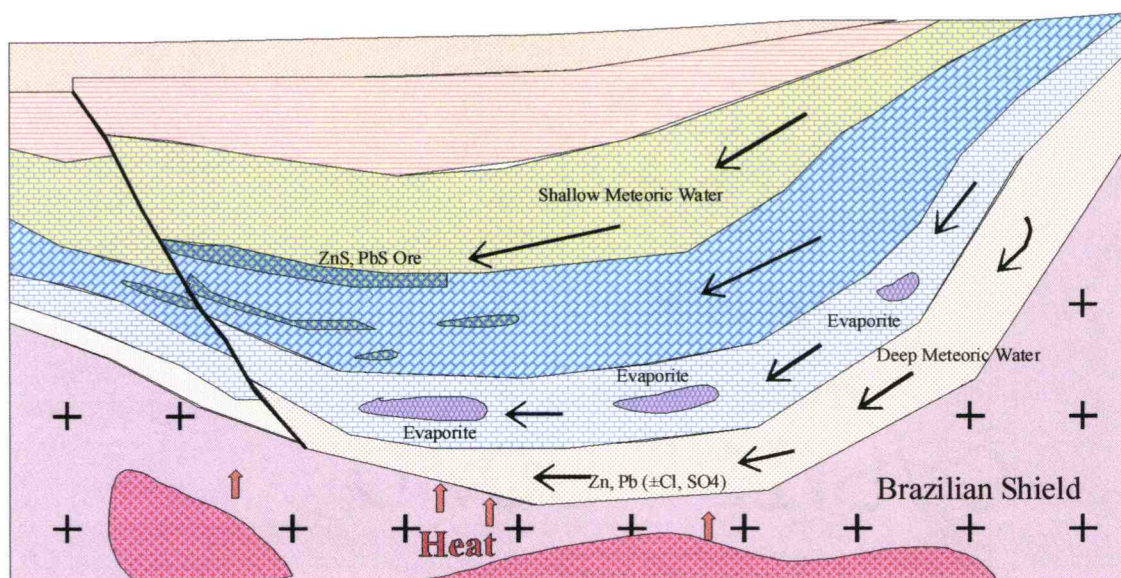


Figure 35. Genetic model of the San Vicente zinc-lead Mississippi Valley type deposit.

SUMMARY AND CONCLUSIONS

The San Vicente zinc-lead deposit is a Mississippi Valley-type deposit. It is epigenetic in origin based on the collective evidence from stratigraphic, tectonic, petrographic and sulfur isotopic characteristics.

The tectonic framework of the Pucara Basin indicates that the source of metals and sulfide are most likely Late Permian sandstones. The lithology of the carbonate sequence indicates changes in the depositional facies. Carbonate units alternate with dolomite units. The limestone formed in a shallow marine facies. The presence of dolomite indicates periodic restrictions to the shallow marine facies and sabkha-like environments. Burial of the sediments imposed increasing temperature in the lower part of the basin. Overthrusting of the sedimentary units occurred during the Andean orogeny. The additional load derived from overthrust igneous rock units caused further subsidence of the sediments. The ore formed at temperatures of between 100 to 150°C in the San Vicente Dolomite, which corresponds to a depth of 3 to 5 km under the assumption of a geothermal gradient of 30°C/km. The temperature at the base of the basin must have been at least 30 to 60°C higher on the basis of stratigraphic separation. Temperature is an important factor on the formation of the ore deposit. The reduction of sulfate to hydrogen sulfide occurs at temperatures above 200°C, and the transport of metals and sulfide in the fluid depends on temperature as well. The tectonic framework indicates that this temperature regime may have been achieved during the Andean orogeny.

Petrographic and mineralogic observations constrain the paragenesis of minerals in the deposit. Primary sedimentary textures in the host dolomite are partially preserved. Dolomitization of the host rock obliterates some of the details. Replacement and dissolution textures are attributed to an acidic hydrothermal fluid that transported metals and sulfides to the deposit. Sphalerite partially replaces the original host rock, and preferentially fills pore spaces and replaces clastic components of the host. Sphalerite has overgrown bitumen at the transition from dolomite-I to sphalerite along the replacement bands. Galena and idiomorphic sphalerite-II form the selvages of the rhythmite, and these were deposited in open spaces. Hydrothermal dolomite-II cements the open spaces between the sphalerite-galena selvages. Pyrite occurs sparingly in the hydrothermal dolomite. The sequence of minerals suggests that the mineralizing fluid was strongly acidic and dissolved large parts of the original host rock, but the fluid did not attack bitumen in the host rock. An increase in carbonic acid content caused the exsolution of carbon dioxide gas from the fluid, which further promoted the generation of open spaces in the host rock. The fluid became neutralized with progressive host rock dissolution, and as a consequence, metal sulfides became saturated and precipitated with increasing pH. The neutralized fluid became increasingly saturated with respect to carbonate dolomite and reprecipitated dolomite-II in the remaining open spaces of the bands and breccia.

Chemical variations of sphalerite and dolomite were detected by electron microprobe analyses. Variations of color in sphalerite can be attributed to its

iron content, which increases towards the center of the rhythmities. Moreover, the concentration of iron increased towards the later stages of sulfide precipitation. Dolomite in the host rock is chemically more uniform than hydrothermal dolomite. The variable trace element content of dolomite-II is attributed to the changing composition of the neutralized ore fluid.

Sulfur isotope measurements indicate the source of sulfur, temperature of sulfide precipitation, and physico-chemical conditions of the ore fluid. The source of sulfur is believed to be marine sulfate that was deposited in sandstones of the Mitu Group and carbonate units of the Pucara Group. The temperature of sulfide deposition was approximately 140°C on the basis of sphalerite-galena geothermometry. Isotope fractionation models exclude the in situ reduction of sulfate by organic matter. The reduction occurred most likely in the clastic sediments of the Mitu Group. The reductant was probably ferrous iron. This mechanism would increase the acidity of the fluid. Isotope variations in the ore can be attributed to Rayleigh fractionation from a finite reservoir of hydrogen sulfide in the ore forming fluid. The presence of pyrite in late stages of ore formation enhanced the isotopic effect.

Thermodynamic and kinetic models further characterize the physical and chemical conditions of the hydrothermal fluid. Sulfate reduction at temperatures above 200°C is favored in acidic solutions that contain initial bisulfide. Solubility products, speciation, pH, and redox conditions strongly favor the epigenetic origin of the deposit. Zinc and lead apparently were derived from leaching of the clastic Mitu Group sediments. Sulfate was reduced by ferrous iron in the source

rock. The ferric iron remained as a residual in the host rock and was not transported by the fluid. The acidic fluid then ascended into the carbonate host rock along hydrological conductive faults. Dolomite was dissolved and neutralized the metal and hydrogen sulfide bearing fluid. Precipitation of sulfides and carbonate as predicted from geochemical considerations is consistent with that observed by the accompanying petrographic study.

The epigenetic origin of the San Vicente deposit implies an exploration strategy for the discovery of similar occurrences. The presence of a clastic source rock that contains ferrous iron as well as a carbonate host rock are essential components for geochemical exploration criteria.

REFERENCES

- Ault, W. U., and Kulp, J. L., 1959. Isotopic geochemistry of sulfur. *Geochimica Cosmochimica Acta*, Vol. 16, p. 511-536.
- Bartlett, M. W., 1984. Petrology and genesis of carbonate-hosted Pb-Zn-Ag ores, San Cristobal District, Department of Junin, Peru: Unpublished Ph.D. dissertation, Oregon State University, 287 p.
- Bates, R.L., and Jackson, J.A., 1987. *Glossary of Geology*. 3rd ed. Alexandria, VA: American Geological Institute.
- Caldas, J., 1983. Tectonic evolution of Peruvian Andes. In: Cabre, R., ed., *Geodynamics of the Eastern Pacific Region, Caribbean and Scotia Arcs*: American Geophysical Union, Geodynamics Series, Vol. 9, p. 77-81.
- Capedevila, R., Megard, F., Paredes, J., and Vidal, P., 1977, Le batholite de San Ramon, Cordillera Oriental du Perou central. *Geologische Rundschau*, Vol. 66, p. 434-446.
- Campbell, A. R., 1987. A sulfur isotope study of the San Cristobal tungsten-base metal mine, Peru. *Mineralium Deposita*, Vol. 22, p. 42-46.
- Claypool, G. E., Holser, W. T., Kaplan, I. R., Sakai, H. and Zak, I., 1980. The age curves of sulfur and oxygen isotopes in marine sulfate and their mutual interpretation. *Chemical Geology*, Vol. 28, p. 199-260.
- Einaudi, M. T., 1977. Environment of Ore Deposition at Cerro De Pasco, Peru. *Economic Geology*, Vol. 72, p. 893 – 924.
- Field, C. W., Rye, W. O., Dymond, J. R., Wheland, J. F., and Senechal, R. G., 1983. Metalliferous sediments of the East Pacific. In: Shanks, W. C., III, ed., *Cameron Volume on unconventional mineral deposits*: New York, Soc. Min. Eng., Amer. Inst. Mining Metall. Petrol. Eng., p. 133-156.

- Folk, R. L., Land, L. S., 1975, Mg/Ca ratio and salinity: two controls over crystallization of dolomite. American Assoc. of Petroleum Geologist Bulletin, Vol. 59, p. 60-68.
- Fontbote, L., 1987. Stratabound Ore Deposits in the Central Andes (Andean Cycle) - Geotectonic and Paleogeographic Setting. Zentralbl. Geol. Paläont., Teil I, H. 7/8, p.1007-1008.
- Fontbote, L., and Gorzawski, H., 1987. Isotope (Sr, C, O, S) tracing of diagenetic ore formation in carbonate-hosted deposits illustrated on the F-(Pb-Zn) deposits in the Alpujarrides, Spain and the San Vicente Zn-Pb Mine, Peru. Soc. Geology Appl. Mineral Deposits Spec. Pub. 6, p. 465-484.
- Fontbote, L., and Gorzawski, H., 1990. Genesis of the Mississippi Valley-Type Zn-Pb deposit of San Vicente, central Peru: Geological and isotopic (Sr, O, C, S) evidences. Economic Geology, V. 85, p. 1402-1437.
- Fontbote, L., Gunnesch, K. A., and Baumann, A., 1990. Metal sources in stratabound ore deposits in the Andes (Andean cycle): Lead isotope constraints. In: Fontbote, L., Amstutz, G. C., Cardozo, M., Cedillo, E., and Frutos, J., eds., Stratabound ore deposits in the Andes. Berlin-Heidelberg-New York, Springer Verlag, p. 759-773.
- Friedman, G.M., 1962. Identification of carbonate minerals by staining methods. J. Sediment. Petrol., V. 29, p. 87-97.
- Gorzawski, H., Fontbote, L., Field, C.W., and Tejada, R., 1990. Sulfur Isotope Studies in the Zinc Lead Mine San Vicente, Central Peru. in Fontbote, L., Amstutz, G.C., Cardozo, M., Cedillio, E., and Frutos, J., eds., Stratabound Ore Deposits in the Andes: Berlin-Heidelberg-New York, Springer Verlag, p.305-312.
- Grinenko, V. A., 1962. Preparation of sulfur dioxide for isotopic analysis. Zeits. Neorgan. Khimii, Vol. 7, p. 2478-2483.
- Gunnesch, K. A., Baumann, A., and Gunnesch, M., 1990, lead isotope variations across the central Peruvian Andes. Economic Geology, 85, p. 1384-1401.

- Holser and Kaplan, 1979 . Isotope Geochemistry of Sedimentary Sulfates. Chemical Geology, V. 32, p.93-135.
- Kullerud, G., 1953. The FeS-ZnS system. A geological thermometer. Norsk. Geol. Tidsskrift p. 32-61.
- Loughman, D. L., and Hallam, A., 1982. A facies analysis of the Pucara Group (Norian to Toarcian carbonates, organic rich shale and phosphate) of central and northern Peru. Sedimentary Geology, Vol. 32, p. 161-194.
- Lange, I.M., Rospigliosi, R.T., and Krouse, H.R., 1990. San Vicente Zinc-Lead Rhytmite Deposit, Peru: A Mississippi Valley-Type Replacement Deposit. in: Proceedings of Pacific Rim Congress 1990 Gold Coast, Queensland, Australia. 1990, Australian Institut of Mining and Metal., 2, p. 435-444.
- Lavado, M., 1980. Geological Aspects of the Occurrence of Zinc-Lead at the San Vicente Mine San Ramon, Tarma, Central Peru. Unpubl. M.S. thesis. U of Texas at Dallas. 115p.
- Levin, P. and Amstutz, G.C., 1976. Kristallisation und Bewegung in Erzrhythmiten am Beispiel triassisch-jurassischer Lagerstätten in Ostperu. Münster. Forsch. Geol. Paläont. 38/39, p.111-128.
- Liu, Y.A. and Schmidt, R.A., 1993. Earth's Partial Pressure of CO₂ over the past 120 Ma; Evidence from Ce Anomalies in the Deep (>600 m) Pacific Ocean. Lunar and Planetary Science XXIV, p. 883-884.
- McLaughlin, D. H., 1924. Geology and physiography of the Peruvian cordillera, Departments of Junin and Lima. Geol. Soc. Of America Bulletin, Vol. 35, p. 591-632.
- McLimans, R.K., Barnes, H.L., Ohmoto, H., 1980. Sphalerite Stratigraphy of the Upper Mississippi Valley Zinc-Lead District, Southwest Wisconsin. Economic Geology, 75, p. 351-361.
- Megard, F., 1968, Geologia del cuadrangulo de Huancayo. Servicio de Geol. Y Minera del Peru Bol., Vol. 18, p. 123.

- Mirsha, B. and Mookherlee, A., 1988. Geothermometry based on fractionation of Mn and Cd between coexisting sphalerite and galena from some carbonate-hosted sulfide deposits in India. *Mineral. Deposita*, 23, p. 179-185.
- Moreland, G.C., 1968. Preparation of polished thin sections. *American Mineralogist* 53, p. 2070-2074.
- Moritz, R., Fontbote, L., Spnagenberg, J., Rosas, S., Sharp, Z., and Fontignie, D., 1996. Sr, C, and O isotope systematics in the Pucara basin, Central Peru: comparison between Mississippi Valley-type deposits and barren areas. *Mineralium Deposita*, V. 31, p. 141-162.
- Ohle, E.L., 1980. Some considerations in Determining the Origin of Ore Deposits of the Mississippi Valley Type - Part II. *Economic Geology*, Vol. 75, p. 161-172.
- Ohmoto, H., 1972. Systematics of sulfur and carbon isotopes in hydrothermal ore deposits. *Economic Geology*, Vol. 67, p. 551-579.
- Ohmoto, H. and Goldhaber, M. B., 1997. Sulfur and carbon isotopes. In: Barnes, H. L., ed., *Geochemistry of hydrothermal Ore Deposits*, 3rd ed.: Wiley, New York, p. 517-611.
- Ohmoto, H. and Rye, R. O., 1972. The Bluebell mine, British Columbia I. Mineralogy, paragenesis, fluid inclusions, and the isotopes of hydrogen, oxygen, and carbon. *Economic Geology*, Vol. 65, p. 417-437.
- Ohmoto, H. and Rye, R. O., 1979. Isotopes of sulfur and carbon. In: Barnes, H. L., ed., *Geochemistry of hydrothermal Ore Deposits*: Holt, Rinehart, and Wilson, Inc., New York, p. 509-567.
- Orr, W. L., 1974. Changes in sulfur content and isotopic ratios of sulfur during petroleum maturation – study of Big Horn Paleozoic oils. *The American Assoc. of Petroleum Geologists Bulletin*, Vol. 58, p. 2295-2318.
- Petersen, U., 1965. Regional geology and major major ore deposits of Central Peru. *Economic Geology*, Vol. 60, p. 407-476.

- Petersen, U., 1972. Nuevas Investigaciones De Yacimientos Peruanos. Boletín de la Sociedad Geologica Del Peru. Vol. 42, p. 36-52.
- Roedder, E. Fluid Inclusion studies of Ore Deposits in the Viburnum Trend, Southeast Missouri. Economic Geology, Vol. 72, p. 474-479.
- Rye, R. O. and Ohmoto, H., 1974. Sulfur and carbon isotopes and ore genesis: A review. Economic Geology, Vol. 69, p. 826-842.
- Rye, R. O., and Sawkins, F. J., 1974. Fluid inclusions and stable isotope studies on the Casapalca Ag-Pb-Zn-Cu deposit, central Andes, Peru. Economic Geology, Vol. 69, p. 181-205.
- Sakai, H., 1968. Isotopic properties of sulfur compounds in hydrothermal processes. Geochem. Journ. (Japan), Vol. 2, p. 29-49.
- Snyder, F.G., 1967. Criteria for the origin of stratiform orebodies. Econ. Geol. Mon. 3, p. 1-13.
- Spangenberg, J., Fontbote, L., and Macko, S. A., 1999. An evaluation of the inorganic and organic geochemistry of the San Vicente Mississippi Valley-Type Zinc-Lead District, Central Peru: implications for ore fluid composition, mixing processes, and sulfate reduction. Economic Geology, V. 94, p. 1067-1092.
- Spirakis, C.S., 1986. The Valence of Sulfur in Disulfides - An Overlooked Clue To The Genesis of Mississippi Valley-type Lead-Zinc Deposits. Economic Geology, V.81, p. 1544-1545.
- Toland, W. G., 1959, Oxidation of Organic Compounds with Aqueous Sulfate. Journ. Amer. Chem. Soc., V. 82, p. 1911-1916.
- Viets, J. G., Hopkins, R.T. and Miller, B., M., 1992. Variations in Minor and Trace Metals in Sphalerite from Mississippi Valley Type Deposits of the Ozark Region: Genetic Implications. Economic Geology, V.87, p. 1897-1905.

Warne, S.St.J., 1962. A quick field or laboratory staining scheme for the differentiation of the major carbonate minerals. *J. Sediment. Petrol.* 32, p. 29-38.

APPENDICES

Appendix 1. Elemental Abundances of Zinc, Iron, Manganese, Cadmium, and Sulfur in Sample SV-1A.

Profile	SV-1A	Stage	Stage	Zn	Fe	Mn	Cd	S	Zn	Fe	Mn	Cd	S	Total
Location	Point #	X	Y	(mol %)	(mol %)	(mol %)	(mol %)	(mol %)	(wt. %)	(wt. %)	(wt. %)	(wt. %)	(wt. %)	
Profile 1	SL 1	-11422	7174	49.0	0.59	0.014	0.15	50.3	64.5	0.66	0.015	0.35	32.5	98.0
Profile 1	SL 2	-11413	7174	49.2	0.45	n.d.	0.13	50.2	65.0	0.51	n.d.	0.29	32.5	98.4
Profile 1	SL 3	-11403	7175	49.1	0.33	0.003	0.13	50.4	64.7	0.38	0.003	0.30	32.6	97.9
Profile 1	SL 4	-11394	7175	49.2	0.25	0.011	0.11	50.4	65.0	0.29	0.012	0.26	32.7	98.2
Profile 1	SL 5	-11384	7175	49.4	0.21	n.d.	0.12	50.2	65.3	0.24	n.d.	0.27	32.6	98.4
Profile 1	SL 6	-11369	7128	49.0	0.26	n.d.	0.09	50.7	64.8	0.29	n.d.	0.21	32.9	98.2
Profile 1	SL 7	-11292	7131	62.4	0.27	0.009	0.13	37.2	64.6	0.24	0.008	0.22	18.9	83.9
Profile 1	SL 8	-11216	7133	49.5		n.d.	0.10	50.4	65.2	0.01	n.d.	0.23	32.6	98.0
Profile 1	SL 9	-11139	7136	49.0	0.17	n.d.	0.15	50.7	64.8	0.19	n.d.	0.33	32.9	98.3
Profile 1	SL 10	-11063	7139	49.1	0.20	0.01	0.15	50.6	64.6	0.23	0.011	0.33	32.7	97.9
Profile 1	SL 11	-10986	7141	49.2	0.10	0.003	0.12	50.6	64.7	0.12	0.004	0.27	32.7	97.8
Profile 1	SL 12	-10910	7144	49.0	0.16	0.009	0.16	50.7	64.6	0.18	0.01	0.36	32.7	97.8
Profile 1	SL 13	-10833	7146	49.1	0.26	n.d.	0.11	50.6	64.3	0.30	n.d.	0.24	32.5	97.4
Profile 1	SL 14	-10757	7149	49.0	0.17	0.005	0.12	50.7	64.4	0.19	0.006	0.28	32.7	97.5
Profile 1	SL 15	-10680	7152	49.0	0.17	0.007	0.12	50.7	64.3	0.19	0.007	0.27	32.6	97.4
Profile 1	SL 16	-10604	7154	48.9	0.27	n.d.	0.11	50.7	64.0	0.30	n.d.	0.25	32.5	97.0
Profile 1	SL 17	-10527	7157	49.1	0.19	n.d.	0.10	50.6	64.6	0.22	n.d.	0.22	32.7	97.7
Profile 1	SL 18	-10423	7130	49.5	0.03	0.01	0.09	50.4	65.5	0.03	0.011	0.20	32.8	98.5
Profile 1	SL 19	-10347	7127	49.4	0.04	0.002	0.08	50.5	65.3	0.04	0.002	0.17	32.8	98.2
Profile 1	SL 20	-10271	7124	49.4	0.03	n.d.	0.07	50.5	64.9	0.03	n.d.	0.16	32.6	97.7
Profile 1	SL 21	-10196	7121	49.3	0.05	0.001	0.08	50.6	64.8	0.05	0.001	0.19	32.6	97.6
Profile 1	SL 22	-10120	7118	49.0	0.02	n.d.	0.08	50.9	64.7	0.03	n.d.	0.18	32.9	97.8
Profile 1	SL 23	-10044	7115	49.1	0.02	0.001	0.08	50.8	64.3	0.03	0.001	0.17	32.6	97.1
Profile 1	SL 24	-9968	7112	49.0	0.03	n.d.	0.08	50.9	64.2	0.04	n.d.	0.19	32.7	97.1
Profile 1	SL 25	-9893	7110	49.4	0.03	n.d.	0.08	50.5	65.1	0.03	n.d.	0.18	32.6	97.9
Profile 1	SL 26	-9817	7107	49.1	0.06	0.003	0.15	50.7	64.6	0.07	0.004	0.34	32.7	97.7
Profile 1	SL 27	-9741	7104	49.4	0.04	n.d.	0.15	50.4	65.1	0.05	n.d.	0.34	32.6	98.1
Profile 1	SL 28	-9665	7101	48.8	0.07	0.005	0.17	50.9	64.1	0.08	0.005	0.38	32.8	97.4
Profile 1	SL 29	-9590	7098	49.1	0.04	n.d.	0.14	50.7	64.3	0.04	n.d.	0.30	32.6	97.2
Profile 1	SL 30	-9514	7095	49.3	0.03	0.012	0.07	50.6	64.9	0.04	0.013	0.15	32.7	97.9

Appendix 1. (Continued)

Profile	SV-1A	Stage	Stage	Zn	Fe	Mn	Cd	S	Zn	Fe	Mn	Cd	S	Total
Location	Point #	X	Y	(mol %)	(mol %)	(mol %)	(mol %)	(mol %)	(wt. %)	(wt. %)	(wt. %)	(wt. %)	(wt. %)	
Profile 1	SL 31	-9438	7092	49.0	0.02	0.005	0.15	50.8	64.2	0.02	0.006	0.33	32.7	97.3
Profile 1	SL 32	-9432	7054	49.1	0.04	n.d.	0.14	50.8	64.3	0.04	n.d.	0.32	32.7	97.4
Profile 1	SL 33	-9338	7074	48.9	0.03	n.d.	0.12	51.0	63.8	0.04	n.d.	0.26	32.6	96.7
Profile 1	SL 34	-9245	7094	48.8	0.02	n.d.	0.14	51.1	64.1	0.02	n.d.	0.32	32.9	97.4
Profile 1	SL 35	-9151	7114	49.0	0.05	0.01	0.12	50.8	64.3	0.05	0.011	0.28	32.7	97.3
Profile 1	SL 36	-9057	7134	49.2	0.04	0.005	0.11	50.6	64.6	0.05	0.005	0.26	32.6	97.4
Profile 1	SL 37	-8963	7153	49.0	0.04	0.023	0.19	50.7	64.6	0.04	0.025	0.42	32.8	97.8
Profile 1	SL 38	-8870	7173	49.2	0.04	0.008	0.13	50.6	64.9	0.05	0.009	0.31	32.8	98.0
Profile 1	SL 39	-8776	7193	49.0	0.02	0.002	0.16	50.8	64.5	0.03	0.002	0.36	32.9	97.8
Profile 1	SL 40	-11657	7133	49.6	0.12	0.012	0.12	50.1	66.2	0.13	0.013	0.28	32.8	99.3
Profile 1	SL 41	-11903	7133	49.5	0.09	0.007	0.14	50.3	65.5	0.11	0.008	0.32	32.6	98.6
Profile 1	SL 42	-12149	7133	49.2	0.22	n.d.	0.15	50.5	65.0	0.25	n.d.	0.33	32.7	98.3
Profile 1	SL 43	-12394	7133	49.0	0.25	n.d.	0.14	50.6	64.9	0.29	n.d.	0.31	32.8	98.3
Profile 1	SL 44	-12640	7133	49.1	0.23	0.008	0.16	50.5	64.9	0.26	0.009	0.37	32.8	98.3
Profile 1	SL 45	-12886	7133	49.2	0.32	n.d.	0.11	50.3	65.7	0.37	n.d.	0.25	32.9	99.2
Profile 1	SL 46	-13132	7133	48.8	0.48	n.d.	0.13	50.6	65.1	0.55	n.d.	0.29	33.1	99.1
Profile 1	SL 47	-13277	7017	49.5	0.04	n.d.	0.08	50.4	65.4	0.05	n.d.	0.18	32.7	98.3
Profile 1	SL 48	-13573	7080	49.2	0.03	0.002	0.09	50.6	64.8	0.03	0.003	0.20	32.7	97.8
Profile 1	SL 49	-13870	7143	49.4	0.04	n.d.	0.16	50.4	65.3	0.04	n.d.	0.37	32.7	98.4
Profile 1	SL 50	-14166	7206	49.5	0.04	n.d.	0.14	50.4	65.3	0.04	n.d.	0.31	32.6	98.3
Profile 2	SL 51	-11657	23899	49.1	0.00	0.006	0.06	50.9	64.7	0.00	0.006	0.14	32.9	97.8
Profile 2	SL 52	-11524	23936	49.1	0.03	0.008	0.05	50.8	65.0	0.03	0.009	0.12	33.0	98.2
Profile 2	SL 53	-11391	23973	49.4	0.03	n.d.	0.06	50.5	65.0	0.03	n.d.	0.15	32.7	97.9
Profile 2	SL 54	-11258	24010	49.4	0.05	0.017	0.12	50.4	63.7	0.05	0.019	0.26	31.9	96.0
Profile 2	SL 55	-11125	24047	49.5	0.03	0.023	0.08	50.4	65.4	0.04	0.025	0.17	32.6	98.2
Profile 2	SL 56	-10992	24084	49.3	0.02	n.d.	0.12	50.5	65.3	0.03	n.d.	0.28	32.8	98.4
Profile 2	SL 57	-10859	24121	49.4	0.03	n.d.	0.06	50.5	65.3	0.03	n.d.	0.14	32.8	98.3
Profile 2	SL 58	-12329	22619	49.1	0.10	0.008	0.07	50.7	65.2	0.11	0.009	0.15	33.0	98.4
Profile 2	SL 59	-12456	22601	49.4	0.10	0.006	0.11	50.4	65.2	0.11	0.006	0.25	32.7	98.2

Appendix 1. (Continued)

Profile	SV-1A	Stage	Stage	Zn	Fe	Mn	Cd	S	Zn	Fe	Mn	Cd	S	Total
Location	Point #	X	Y	(mol %)	(mol %)	(mol %)	(mol %)	(mol %)	(wt. %)	(wt. %)	(wt. %)	(wt. %)	(wt. %)	
Profile 2	SL 60	-12583	22584	49.4	0.08	n.d.	0.12	50.4	65.4	0.09	n.d.	0.27	32.7	98.5
Profile 2	SL 61	-12710	22566	49.5	0.04	0.001	0.17	50.3	65.6	0.05	0.001	0.38	32.8	98.8
Profile 2	SL 62	-12837	22548	49.4	0.01	n.d.	0.14	50.5	65.6	0.01	n.d.	0.32	32.9	98.9
Profile 2	SL 63	-12964	22531	49.3	0.03	n.d.	0.08	50.6	65.0	0.03	n.d.	0.18	32.8	98.0
Profile 2	SL 64	-13091	22513	49.4	0.03	n.d.	0.07	50.5	65.3	0.03	n.d.	0.16	32.8	98.2
Profile 2	SL 65	-11299	22461	49.2	0.04	n.d.	0.14	50.6	64.8	0.04	n.d.	0.32	32.7	97.8
Profile 2	SL 66	-11230	22326	49.3	0.04	0.014	0.14	50.5	65.1	0.05	0.015	0.31	32.7	98.2
Profile 2	SL 67	-11160	22191	49.0	0.06	n.d.	0.13	50.8	64.4	0.07	n.d.	0.30	32.8	97.6
Profile 2	SL 68	-11090	22056	49.1	0.07	n.d.	0.13	50.7	64.6	0.07	n.d.	0.29	32.8	97.8
Profile 2	SL 69	-11020	21921	49.2	0.04	0.014	0.11	50.6	64.9	0.04	0.015	0.26	32.8	98.0
Profile 2	SL 70	-4664	12145	49.1	0.11	n.d.	0.14	50.7	64.5	0.12	n.d.	0.31	32.7	97.6
Profile 2	SL 71	-4241	12208	49.2	0.17	n.d.	0.17	50.5	65.4	0.19	n.d.	0.39	32.9	98.9
Profile 2	SL 72	-5203	15822	49.1	0.04	n.d.	0.11	50.7	64.6	0.05	n.d.	0.25	32.7	97.6
Profile 2	SL 73	-4978	15847	49.3	0.03	n.d.	0.08	50.6	65.3	0.04	n.d.	0.17	32.9	98.4
Profile 2	SL 74	-4754	15871	49.4	0.03	0.002	0.09	50.4	65.4	0.03	0.002	0.21	32.8	98.4
Profile 2	SL 75	-4529	15896	49.2	0.06	n.d.	0.08	50.7	65.0	0.07	n.d.	0.18	32.8	98.1
Profile 2	SL 76	-4304	15920	49.3	0.05	0.006	0.07	50.6	65.2	0.05	0.007	0.16	32.8	98.1
Profile 2	SL 77	-4080	15945	49.3	0.21	0.003	0.17	50.3	64.4	0.24	0.003	0.38	32.2	97.2
Profile 2	SL 78	-3855	15969	49.5	0.10	n.d.	0.15	50.3	65.4	0.11	n.d.	0.33	32.6	98.5
Profile 2	SL 79	-3631	15994	49.5	0.07	n.d.	0.16	50.3	65.6	0.08	n.d.	0.37	32.7	98.8
Profile 2	SL 80	-3406	16018	49.4	0.08	n.d.	0.16	50.4	65.6	0.09	n.d.	0.36	32.8	98.9
Profile 2	SL 81	-3181	16043	49.3	0.03	0.015	0.18	50.4	65.6	0.03	0.017	0.41	32.9	98.9
Profile 2	SL 82	-2957	16068	49.5	0.04	0.014	0.25	50.2	65.9	0.04	0.016	0.58	32.8	99.4
Profile 2	SL 83	-2732	16092	49.6	0.03	0.007	0.19	50.2	66.0	0.03	0.008	0.43	32.8	99.2
Profile 2	SL 84	-2041	16159	49.0	0.66	n.d.	0.17	50.2	64.9	0.75	n.d.	0.39	32.6	98.6
Profile 2	SL 85	-1813	16138	49.6	0.09	0.009	0.13	50.2	66.1	0.10	0.01	0.31	32.8	99.3
Profile 2	SL 86	-1585	16117	48.9	0.38	n.d.	0.21	50.5	65.3	0.44	n.d.	0.49	33.1	99.3
Profile 2	SL 87	-1357	16097	49.0	0.22	n.d.	0.21	50.6	65.7	0.25	n.d.	0.49	33.3	99.7
Profile 2	SL 88	-1129	16076	49.4	0.39	0.002	0.16	50.1	65.8	0.44	0.003	0.37	32.8	99.4
Profile 2	SL 89	-900	16055	49.1	0.57	0.01	0.17	50.2	65.4	0.65	0.011	0.38	32.8	99.2

Appendix 1. (Continued)

Profile	SV-1A	Stage	Stage	Zn	Fe	Mn	Cd	S	Zn	Fe	Mn	Cd	S	Total
Location	Point #	X	Y	(mol %)	(mol %)	(mol %)	(mol %)	(mol %)	(wt. %)	(wt. %)	(wt. %)	(wt. %)	(wt. %)	
Profile 2	SL 90	-672	16034	49.4	0.08	0.002	0.20	50.3	66.1	0.09	0.003	0.45	33.0	99.7
Profile 2	SL 91	-444	16014	49.2	0.22	n.d.	0.15	50.4	65.0	0.24	n.d.	0.34	32.6	98.3
Profile 2	SL 92	-216	15993	49.1	0.47	n.d.	0.12	50.3	65.5	0.53	n.d.	0.27	32.9	99.2
Profile 2	SL 93	11	15972	48.9	0.66	n.d.	0.15	50.3	64.9	0.74	n.d.	0.33	32.8	98.8
Profile 2	SL 94	239	15951	49.2	0.53	n.d.	0.12	50.1	65.5	0.60	n.d.	0.27	32.7	99.1
Profile 2	SL 95	467	15931	49.6	0.10	n.d.	0.08	50.3	65.7	0.11	n.d.	0.19	32.7	98.6
Profile 2	SL 96	695	15910	49.8	0.11	n.d.	0.06	50.0	66.2	0.13	n.d.	0.13	32.6	99.0
Profile 2	SL 97	924	15889	49.5	0.18	n.d.	0.07	50.2	65.9	0.20	n.d.	0.16	32.8	99.0
Profile 2	SL 98	1152	15868	49.6	0.13	0.001	0.06	50.2	66.0	0.15	0.001	0.13	32.7	99.0
Profile 2	SL 99	1380	15847	49.5	0.15	n.d.	0.03	50.3	65.7	0.17	n.d.	0.06	32.7	98.6
Profile 2	SL 101	1836	15806	49.6	0.19	0.003	0.05	50.2	66.1	0.22	0.003	0.11	32.8	99.3
Profile 3	SL 102	-5164	12515	49.1	0.05	n.d.	0.14	50.2	64.4	0.06	n.d.	0.31	32.6	97.3
Profile 3	SL 103	-4969	12488	49.2	0.05	n.d.	0.14	50.7	64.6	0.06	n.d.	0.31	32.6	97.6
Profile 3	SL 104	-4774	12461	49.2	0.04	0.01	0.14	50.6	64.6	0.04	0.011	0.31	32.6	97.6
Profile 3	SL 105	-4578	12434	49.6	0.07	n.d.	0.13	50.6	62.7	0.08	n.d.	0.29	31.1	94.2
Profile 3	SL 106	-4383	12407	49.1	0.11	0.002	0.15	50.2	64.6	0.13	n.d.	0.33	32.7	97.7
Profile 3	SL 107	-4188	12381	49.2	0.15	n.d.	0.14	50.6	64.5	0.16	n.d.	0.31	32.5	97.5
Profile 3	SL 108	-3993	12354	49.3	0.16	0.011	0.14	50.6	64.9	0.18	0.012	0.32	32.5	98.0
Profile 3	SL 109	-3797	12327	48.9	0.15	0.002	0.13	50.4	64.4	0.17	n.d.	0.29	32.8	97.6
Profile 3	SL 110	-3602	12300	48.8	0.08	0.01	0.16	50.8	64.3	0.09	0.011	0.37	32.9	97.6
Profile 3	SL 111	-3407	12273	49.3	0.11	n.d.	0.16	50.9	64.6	0.12	n.d.	0.36	32.5	97.5
Profile 3	SL 112	-3212	12246	48.9	0.05	n.d.	0.18	50.5	64.5	0.06	n.d.	0.40	32.9	97.8
Profile 3	SL 113	-3016	12219	49.0	0.05	n.d.	0.16	50.8	64.1	0.05	n.d.	0.36	32.6	97.1
Profile 3	SL 114	-2821	12192	49.1	0.04	n.d.	0.15	50.8	64.1	0.05	n.d.	0.35	32.5	97.0
Profile 3	SL 115	-2626	12165	49.1	0.05	n.d.	0.13	50.7	64.5	0.06	n.d.	0.28	32.7	97.5
Profile 3	SL 116	-2431	12139	49.3	0.05	n.d.	0.20	50.7	64.9	0.05	n.d.	0.45	32.6	98.0
Profile 3	SL 117	-2235	12112	49.2	0.02	0.018	0.18	50.5	64.7	0.02	0.02	0.40	32.6	97.8
Profile 3	SL 118	-2040	12085	49.0	0.02	n.d.	0.16	50.6	64.3	0.03	n.d.	0.35	32.7	97.4
Profile 3	SL 119	-1845	12058	49.0	0.02	0.015	0.19	50.8	64.4	0.02	0.016	0.43	32.7	97.6

Appendix 1. (Continued)

Profile	SV-1A	Stage	Stage	Zn	Fe	Mn	Cd	S	Zn	Fe	Mn	Cd	S	Total
Location	Point #	X	Y	(mol %)	(mol %)	(mol %)	(mol %)	(mol %)	(wt. %)	(wt. %)	(wt. %)	(wt. %)	(wt. %)	
Profile 4	SL 120	-11084	24199	49.4	0.03	0.001	0.12	50.7	65.2	0.04	0.001	0.27	32.7	98.1
Profile 4	SL 121	-11045	24125	49.8	0.04	n.d.	0.07	50.5	66.6	0.05	n.d.	0.17	32.9	99.7
Profile 4	SL 122	-11006	24050	49.3	0.04	n.d.	0.12	50.1	65.2	0.05	0.001	0.27	32.7	98.2
Profile 4	SL 123	-10966	23976	49.8	0.04	n.d.	0.15	50.5	66.0	0.04	n.d.	0.35	32.5	98.9
Profile 4	SL 124	-11359	23896	49.5	0.04	0.016	0.12	50.0	65.3	0.05	0.017	0.28	32.6	98.2
Profile 4	SL 125	-11360	23963	49.3	0.03	n.d.	0.09	50.4	65.2	0.04	n.d.	0.21	32.8	98.2
Profile 4	SL 126	-11362	24029	49.4	0.03	0.011	0.08	50.6	65.7	0.04	0.012	0.17	32.9	98.8
Profile 4	SL 127	-11363	24096	49.4	0.06	0.008	0.07	50.4	65.3	0.07	0.009	0.16	32.7	98.2

Appendix 2. Elemental Abundances of Zinc, Iron, Manganese, Cadmium, and Sulfur in Sample SV-5B.

Profile	SV-5B	Stage	Stage	Zn	Fe	Mn	Cd	S	Zn	Fe	Mn	Cd	S	Total
Location	Point #	X	Y	(mol %)	(mol %)	(mol %)	(mol %)	(mol %)	(wt. %)	(wt. %)	(wt. %)	(wt. %)	(wt. %)	
Profile 1	SL 1	2624	-23507	48.9	0.61	0.007	0.16	50.3	64.0	0.68	0.008	0.36	32.3	97.3
Profile 1	SL 2	2624	-23378	48.2	0.69	0.01	0.16	50.9	63.3	0.78	0.011	0.36	32.8	97.2
Profile 1	SL 3	2624	-23248	48.8	0.60	n.d.	0.16	50.5	63.9	0.67	n.d.	0.35	32.4	97.4
Profile 1	SL 4	2624	-23119	48.6	0.60	n.d.	0.17	50.6	63.6	0.67	0.001	0.38	32.4	97.1
Profile 1	SL 6	2624	-22989	48.5	0.62	0.009	0.18	50.7	63.5	0.70	0.01	0.39	32.6	97.2
Profile 1	SL 7	2624	-22860	48.9	0.31	0.004	0.26	50.6	63.8	0.35	0.005	0.59	32.4	97.1
Profile 1	SL 8	2624	-22730	49.0	0.30	n.d.	0.35	50.3	63.9	0.34	n.d.	0.80	32.2	97.3
Profile 1	SL 9	2572	-22628	49.0	0.29	0.01	0.24	50.5	63.7	0.32	0.011	0.55	32.2	96.8
Profile 1	SL 10	2572	-22453	49.1	0.25	n.d.	0.20	50.4	64.4	0.27	n.d.	0.46	32.4	97.5
Profile 1	SL 11	2572	-22277	49.1	0.23	n.d.	0.15	50.5	64.1	0.26	n.d.	0.33	32.4	97.1
Profile 1	SL 12	2660	-22057	48.9	0.32	n.d.	0.13	50.6	64.3	0.36	n.d.	0.30	32.7	97.6
Profile 1	SL 13	2660	-21941	48.9	0.20	n.d.	0.15	50.7	63.8	0.23	n.d.	0.35	32.4	96.8
Profile 1	SL 14	2660	-21825	48.8	0.33	0.008	0.12	50.7	64.0	0.37	0.009	0.27	32.6	97.3
Profile 1	SL 15	2660	-21709	49.0	0.28	n.d.	0.14	50.6	64.2	0.32	n.d.	0.31	32.5	97.4
Profile 1	SL 16	2660	-21593	48.8	0.48	n.d.	0.10	50.6	63.9	0.53	n.d.	0.23	32.5	97.1
Profile 1	SL 17	2660	-21476	48.2	0.93	0.015	0.09	50.8	63.8	1.05	0.017	0.19	33.0	98.0
Profile 1	SL 18	2660	-21360	48.0	0.93	0.006	0.10	51.0	63.9	1.05	0.007	0.23	33.2	98.4
Profile 1	SL 19	2660	-21244	48.3	0.89	n.d.	0.11	50.7	64.0	1.01	n.d.	0.25	32.9	98.2
Profile 1	SL 20	2660	-21128	48.8	0.76	0.02	0.11	50.3	64.4	0.85	0.022	0.25	32.5	98.1
Profile 1	SL 21	2748	-21017	48.4	0.82	0.003	0.12	50.6	63.5	0.92	0.004	0.28	32.6	97.3
Profile 1	SL 22	2748	-20896	48.5	0.83	n.d.	0.13	50.6	63.8	0.93	n.d.	0.30	32.7	97.7
Profile 1	SL 23	2748	-20775	48.7	0.79	n.d.	0.13	50.4	64.2	0.89	n.d.	0.29	32.6	98.0
Profile 1	SL 24	2748	-20654	48.6	0.84	n.d.	0.14	50.4	63.9	0.94	n.d.	0.32	32.5	97.7
Profile 1	SL 25	2748	-20532	48.4	0.87	n.d.	0.15	50.6	63.7	0.98	n.d.	0.33	32.6	97.6
Profile 1	SL 26	2748	-20411	48.3	0.93	n.d.	0.14	50.6	63.7	1.05	n.d.	0.32	32.8	97.9
Profile 1	SL 27	2748	-20290	48.3	0.72	n.d.	0.16	50.8	63.6	0.80	n.d.	0.36	32.8	97.5
Profile 1	SL 28	2671	-20178	48.4	1.10	n.d.	0.12	50.3	63.6	1.24	n.d.	0.27	32.4	97.5
Profile 1	SL 29	2671	-20045	46.9	2.55	n.d.	0.08	50.4	62.0	2.88	n.d.	0.18	32.7	97.8
Profile 1	SL 30	2671	-19911	49.1	0.30	0.004	0.12	50.5	64.6	0.34	0.004	0.27	32.5	97.7
Profile 1	SL 31	2671	-19778	48.4	0.92	0.004	0.14	50.5	63.2	1.03	0.004	0.31	32.4	96.9

Appendix 2. (Continued.)

Profile	SV-5B	Stage	Stage	Zn	Fe	Mn	Cd	S	Zn	Fe	Mn	Cd	S	Total
Location	Point #	X	Y	(mol %)	(mol %)	(mol %)	(mol %)	(mol %)	(wt. %)	(wt. %)	(wt. %)	(wt. %)	(wt. %)	
Profile 2	SL 32	681	-26720	48.6	0.79	0.001	0.16	50.4	64.0	0.88	0.001	0.36	32.5	97.8
Profile 2	SL 33	957	-26720	48.7	0.64	n.d.	0.13	50.6	64.1	0.72	n.d.	0.29	32.7	97.7
Profile 2	SL 34	1232	-26720	49.0	0.52	0.001	0.14	50.3	64.5	0.58	0.001	0.31	32.5	97.9
Profile 2	SL 35	1494	-26720	46.8	2.29	0.014	0.20	50.7	61.7	2.58	0.015	0.45	32.8	97.6
Profile 2	SL 36	1752	-26720	48.1	0.92	0.001	0.15	50.8	63.2	1.03	0.001	0.34	32.7	97.2
Profile 2	SL 37	2010	-26720	48.544	0.752	0.009	0.131	50.565	64.072	0.848	0.009	0.296	32.735	97.96
Profile 2	SL 38	2268	-26720	47.9	1.187	0.012	0.14	50.76	62.895	1.332	0.013	0.316	32.692	97.248
Profile 2	SL 39	2526	-26720	49.2	0.47	n.d.	0.19	50.2	65.2	0.53	n.d.	0.43	32.6	98.8
Profile 2	SL 40	2713	-26619	49.2	0.19	0.009	0.34	50.3	61.6	0.20	0.009	0.73	30.9	93.4
Profile 2	SL 41	3008	-26619	49.2	0.14	0.02	0.22	50.4	64.9	0.16	0.022	0.49	32.6	98.2
Profile 2	SL 42	3303	-26619	49.5	0.17	n.d.	0.13	50.3	65.1	0.19	n.d.	0.28	32.4	98.0
Profile 2	SL 43	3597	-26619	49.3	0.30	n.d.	0.07	50.4	65.2	0.34	n.d.	0.16	32.7	98.4
Profile 2	SL 44	3892	-26619	49.2	0.26	0.001	0.07	50.4	65.3	0.30	0.001	0.15	32.8	98.5
Profile 2	SL 45	3892	-26619	48.0	0.39	n.d.	0.14	51.4	62.6	0.43	n.d.	0.32	32.9	96.3
Profile 2	SL 46	4126	-26619	49.2	0.19	n.d.	0.19	50.5	64.1	0.21	n.d.	0.44	32.3	97.0
Profile 2	SL 47	4359	-26619	48.9	0.31	0.015	0.26	50.5	64.3	0.35	0.017	0.58	32.6	97.8
Profile 2	SL 48	4593	-26619	48.5	0.38	n.d.	0.21	50.9	63.6	0.42	n.d.	0.48	32.7	97.2
Profile 2	SL 49	4827	-26619	48.7	0.56	0.001	0.15	50.6	64.1	0.63	0.001	0.33	32.7	97.8
Profile 2	SL 50	5061	-26619	46.8	2.27	0.003	0.13	50.8	61.8	2.56	0.003	0.30	32.9	97.6
Profile 2	SL 51	5294	-26619	48.4	0.65	n.d.	0.14	50.8	63.4	0.72	n.d.	0.31	32.7	97.1
Profile 2	SL 52	5528	-26619	47.9	1.00	n.d.	0.15	51.0	62.7	1.12	n.d.	0.33	32.8	97.0
Profile 3	SL 53	2558	-24066	48.3	0.79	n.d.	0.11	50.8	63.6	0.89	n.d.	0.26	32.9	97.6
Profile 3	SL 54	2427	-24306	48.4	0.81	0.005	0.12	50.7	63.3	0.91	0.005	0.26	32.6	97.0
Profile 3	SL 55	2296	-24546	48.3	1.00	0.003	0.10	50.2	62.8	1.54	0.004	0.23	32.0	96.6
Profile 3	SL 56	2165	-24786	49.0	0.25	n.d.	0.14	50.6	64.4	0.28	n.d.	0.31	32.6	97.6
Profile 3	SL 57	2034	-25026	48.4	0.21	n.d.	0.10	50.5	63.8	1.09	n.d.	0.22	32.6	97.7
Profile 3	SL 58	1903	-25266	49.3	0.20	n.d.	0.21	50.3	64.7	0.23	n.d.	0.47	32.4	97.8
Profile 3	SL 59	1772	-25506	44.3	3.30	n.d.	0.22	52.2	58.4	3.73	n.d.	0.50	33.8	96.4
Profile 3	SL 60	1641	-25746	44.5	3.15	n.d.	0.23	52.1	59.0	3.57	n.d.	0.52	33.9	97.0
Profile 3	SL 61	1641	-25746	49.2	0.20	n.d.	0.23	50.4	64.6	0.22	n.d.	0.52	32.4	97.8

Appendix 2. (Continued.)

Profile	SV-5B	Stage	Stage	Zn	Fe	Mn	Cd	S	Zn	Fe	Mn	Cd	S	Total
Location	Point #	X	Y	(mol %)	(mol %)	(mol %)	(mol %)	(mol %)	(wt. %)	(wt. %)	(wt. %)	(wt. %)	(wt. %)	
Profile 3	SL 62	1751	-25571	49.2	0.14	0.008	0.24	50.4	64.9	0.15	0.009	0.55	32.6	98.2
Profile 3	SL 63	1860	-25395	49.2	0.20	0.002	0.17	50.5	64.8	0.22	0.002	0.38	32.6	98.1
Profile 3	SL 64	1969	-25220	49.2	0.30	0.001	0.13	50.4	64.6	0.34	0.001	0.29	32.5	97.7
Profile 3	SL 65	2078	-25045	49.3	0.22	n.d.	0.11	50.4	64.8	0.25	n.d.	0.25	32.5	97.9
Profile 3	SL 66	2187	-24869	48.7	0.79	n.d.	0.09	50.4	64.3	0.89	n.d.	0.20	32.6	98.0
Profile 3	SL 67	2297	-24694	48.7	0.81	n.d.	0.11	50.4	64.6	0.92	n.d.	0.24	32.8	98.6
Profile 3	SL 68	2406	-24519	48.7	0.80	0.003	0.11	50.4	64.5	0.90	0.003	0.25	32.7	98.3
Profile 3	SL 69	2515	-24343	48.6	0.79	n.d.	0.13	50.5	64.3	0.90	n.d.	0.30	32.8	98.4
Profile 3	SL 70	2624	-24168	48.8	0.27	n.d.	0.20	50.7	63.7	0.30	n.d.	0.46	32.4	96.9
Profile 4	SL 71	277	-25405	48.7	0.16	n.d.	0.28	50.8	63.4	0.18	n.d.	0.63	32.4	96.7
Profile 4	SL 72	277	-25705	48.5	0.80	n.d.	0.16	50.5	63.6	0.90	n.d.	0.35	32.5	97.4
Profile 4	SL 73	277	-26006	48.7	0.50	n.d.	0.11	50.7	64.0	0.56	n.d.	0.25	32.7	97.5
Profile 4	SL 74	277	-26306	47.74	0.628	n.d.	0.051	51.581	62.312	0.7	n.d.	0.115	33.024	96.151
Profile 5	SL 75	-86	-24549	48.134	0.927	n.d.	0.124	50.815	63.245	1.04	n.d.	0.28	32.749	97.314
Profile 5	SL 76	-103	-24300	48.2	0.97	n.d.	0.14	50.7	63.1	1.08	n.d.	0.31	32.5	96.9
Profile 5	SL 77	-120	-24051	48.2	0.97	n.d.	0.12	50.7	63.3	1.09	n.d.	0.28	32.7	97.4
Profile 5	SL 78	-137	-23802	48.5	0.75	n.d.	0.18	50.6	63.6	0.84	n.d.	0.40	32.5	97.3
Profile 5	SL 79	-154	-23553	48.1	0.93	0.021	0.14	50.8	63.1	1.04	0.023	0.31	32.7	97.2
Profile 5	SL 80	-171	-23304	48.9	0.32	0.022	0.05	50.8	63.5	0.36	0.024	0.11	32.4	96.4

Appendix 4. Input parameter and calculations of Isotope Fractionation Model II.

Model II Reduced System -- H₂S MeS fractionation only

$$\delta^{34}\text{S}_{slf} = \delta^{34}\text{S}_t + 1000 \left(F^{\alpha_{sl-H_2S} - 1} \right) + \Delta_{sl-H_2S}$$

Isotopic equilibrium prevails at all temperatures between sphalerite and aqueous H₂S and SO₄. The total isotopic composition of the system is 15‰ - marine seawater sulfate. Aqueous SO₄ does not participate in reactions in hydrothermal system.

The reduction of sulfate is kinetically inhibited, and sulfate is a passive component of the system. Therefore, fractionation effects relate only to sphalerite-H₂S equilibria and the finite sulfur reservoir.

Phase	Pyrite	Galena	Sphalerite
mol fraction (X) :	0.06	0.09	0.85

Isothermal Model at 373.15 K (100 C) :

Δ_{sl-H_2S} :	0.7	α_{sl-H_2S}	1.00072
$\delta^{34}\text{S}_{H_2S_t}$:	15		

F	$\delta^{34}\text{S}_{slf}$	F	$\delta^{34}\text{S}_{slf}$
1	15.7	0.5	15.2
0.9	15.6	0.4	15.1
0.8	15.6	0.3	14.9
0.7	15.5	0.2	14.6
0.6	15.4	0.1	14.1

Temperature effect of Model II for sphalerite, galena, pyrite system

Temperature [K]:	448.15	438.2	428.2	418.2	408.2	398.2
$\alpha_{(sl-H_2S)}$:	1.00050	1.00052	1.00055	1.00057	1.00060	1.00063
Δ_{sl-H_2S} :	0.50	0.52	0.55	0.57	0.60	0.63
$\delta^{34}\text{S}_{H_2S_t}$:	15	15	15	15	15	15
T [°C]:	175	165	155	145	135	125

Fraction F	$\delta^{34}\text{S}_{Sl}(F, T)$					
1	17.0	17.1	17.2	17.3	17.4	17.5
0.9	16.8	16.9	17.0	17.0	17.1	17.3
0.8	16.5	16.6	16.7	16.8	16.9	17.0
0.7	16.3	16.3	16.4	16.5	16.5	16.6
0.6	16.0	16.0	16.1	16.1	16.2	16.2
0.5	15.6	15.6	15.7	15.7	15.7	15.8
0.4	15.2	15.2	15.2	15.2	15.2	15.2
0.3	14.6	14.6	14.6	14.5	14.5	14.5
0.2	13.8	13.7	13.7	13.6	13.5	13.5
0.1	12.4	12.3	12.2	12.0	11.9	11.7

Appendix 5. Input parameter and calculations of Isotope Fractionation Model III.

Model III

Changing pe and pH Conditions

$$\delta^{34}\text{S}_{sl_f} = \delta^{34}\text{S}_t + \Delta_{\text{SO}_4-\text{H}_2\text{S}} - (\Delta_{\text{SO}_4-\text{H}_2\text{S}} \cdot X_{\text{H}_2\text{S}}) + \Delta_{sl-\text{H}_2\text{S}}$$

$\Delta_{\text{SO}_4-\text{H}_2\text{S}}$: -46.98

Temperature : 373.15 K

$\alpha_{(\text{SO}_4-\text{H}_2\text{S})}$: 0.9541

System contains abundant sulfur. The proportions of aqueous H_2S and SO_4 change with variations in pe and pH. $F = X_{\text{H}_2\text{S}} / (X_{\text{H}_2\text{S}} + X_{\text{SO}_4})$

Isothermal Model at 373.15 K (100 C) :

$\Delta_{sl-\text{H}_2\text{S}}$: 0.7

$\alpha_{sl-\text{H}_2\text{S}}$: 1.00072

$\delta^{34}\text{S}_{\text{H}_2\text{S}_t}$: 15

F	$\delta^{34}\text{S}_{sl} (F)$	F	$\delta^{34}\text{S}_{sl} (F)$
1	15.7	0.5	-7.8
0.9	11.0	0.4	-12.5
0.8	6.3	0.3	-17.2
0.7	1.6	0.2	-21.9
0.6	-3.1	0.1	-26.6

F	$\delta^{34}\text{S}_{sl} (F)$	F	$\delta^{34}\text{S}_{sl} (F)$
0.9	11.0	0.84	8.2
0.89	10.6	0.83	7.7
0.88	10.1	0.82	7.3
0.87	9.6	0.81	6.8
0.86	9.1	0.8	6.3
0.85	8.7	0.79	5.9

Effect of temperature on Model III

Temperature [°C]	175	165	155	145	135	125
Temperature [K]	448	438	428	418	408	398
$\Delta_{\text{H}_2\text{S}-\text{SO}_4}$	-32.7	-34.2	-35.8	-37.5	-39.4	-41.3
$\Delta_{sl-\text{H}_2\text{S}}$	0.50	0.52	0.55	0.57	0.60	0.63

F	$\delta^{34}\text{S}_{sl} (F, T)$					
0.9	12.2	12.1	12.0	11.8	11.7	11.5
0.85	10.6	10.4	10.2	9.9	9.7	9.4
0.8	8.9	8.7	8.4	8.1	7.7	7.4
0.75	7.3	7.0	6.6	6.2	5.8	5.3
0.7	5.7	5.3	4.8	4.3	3.8	3.2

